Computed tomography radiomic texture features dependence upon imaging parameters

---

by

Frank Makosa

UNIVERSITY OF THE FREE STATE
UNIVERSITEIT VAN DIE VRYSTAAT
YUNIVESITHI YA FREISTATA

A thesis to be submitted for the degree

Master of Medical Science in Medical Physics

Department of Medical Physics

School of Medicine

Faculty of Health Sciences

Supervisor: Dr S.N.N. Acho

Co-Supervisors: Prof W.I.D. Rae & Prof L.E. Court

November 2019

ACKNOWLEDGMENTS OR DEDICATION

Firstly, I would like to express my sincere gratitude to my supervisors Dr. Susan Acho, Prof. William Rae and Prof. Laurence Court for the continuous support of my M.Med.Sc study, for their patience, motivation, and immense knowledge. Their guidance helped me during the research and writing of this thesis. I could not have imagined having better supervisors and mentors for my M.Med.Sc study. In particular, I am grateful to Prof. William Rae for his insights, and enlightenment he imparted on me throughout this research.

My sincere thanks also go to the radiomics research group at MD Anderson Cancer Center of The University of Texas. They provided me with a phantom called the credence cartridge radiomics (CCR). The CCR phantom was integral to my study and without the CCR phantom it would not be possible to conduct this research.

I extend my profound thanks to the Harvard Medical School scientific researchers for developing 3D Slicer, a free and open source software package for image analysis and scientific visualization. I extensively used 3D Slicer for most of my image analysis in my study.

I would also like to pass my gratitude to Mrs Dedri O'Reilly, a Senior Medical Physicist at the department medical physics at University of the Free State (UFS). She shared the cone beam computed tomography (CBCT) images for cervical cancer patients which was an essential component of this research study.

I thank my fellow colleagues in the Medical Physics Department for the questions and discussing we had about my research study during our department's Monday meetings. Also, I thank my fellow officemate Milani Qebetu for the sleepless nights we worked together before deadlines, and for all the fun we have had in the two years of my study.

Last but not the least, I would like to thank my family: my wife and kids for supporting me spiritually throughout my writing of this thesis and my life in general.

DECLARATION

Author: Frank Makosa

Degree: M.Med.Sc

Title: Computed tomography radiomic texture features dependence upon imaging parameters

Date of deposit:

I, Frank Makosa, certify that the thesis hereby submitted by me for M.Med.Sc (Medical Physics) degree at the University of the Free State, is my independent effort and had not previously been submitted for a degree at another University/Faculty. I furthermore waive copyright of the thesis in favour of the University of the Free State.

Author signature:

ABSTRACT

Introduction and Aim: Few studies have been carried out to determine the influence of Computed Tomography (CT) acquisition parameters (slice thickness, tube potential difference (kVp), and tube current time product (mAs)) on the quantitative image features in radiomics studies. There is little evidence in the published literature, of studies that use mathematics to establish radiomic texture features that are independent of the CT scan technique parameters. The stability of radiomic texture features may have a great impact on the diagnosis and treatment of cancers. Robust texture features can be used to track radiotherapy treatment response. In this study radiomic texture features were investigated to identify features that did not depend on the CT technique parameters.

Methodology: The credence cartridge radiomics (CCR) phantom was imaged at four CT units at the Universitas Academic and the National District hospitals. The tube current-time product (mAs) was varied from 75 to 400 mAs in steps of 25mAs while the kilovoltage peak and slice thickness were kept set at 120kVp and 5 mm respectively. The CT tube potential was investigated at 80, 100, 120 and 135 kVp whilst mAs and slice thickness was kept set at 300 mAs and 5 mm respectively. The slice thickness was varied from 1 mm to 5 mm whilst the mAs and kVp was kept constant at 300 mAs and 120kVp respectively. The acquisition field of view (FOV) and pitch were kept constant. The images obtained were processed using PyRadiomics software platform of 3D Slicer and the Matlab 2017a package. PyRadiomics was used to segment and extract a total of 105 radiomics texture features for each region of interest (ROI) delineated on an image. The 105 radiomic features included 13 shape features, 18 first order statistics features, 23 grey-level co-occurrence matrix, 14 grey level difference matrix, 16 grey-level run length matrix, 16 grey level size zone matrix and 5 neighbourhood grey tone difference matrix features. For each 10 CCR phantom inserts, 16 ROI of 2cm diameter was segmented by aligning the centre of the ROI at the centre of the insert. The Matlab package was used to segment and extract image matrices that were used to perform hand GLCM calculations. A kV Cone Beam Computed Tomography (kV CBCT) acquired cervical cancer data-set was used to establish the robust radiomic texture features response to radiotherapy treatment. The kV CBCT images were acquired first day and weekly during the 25 treatment fractions.

Results: Five first order statistic radiomic features and six grey level co-occurrence matrix features were identified in the experimental test and mathematical manual calculations tests to vary with coefficients of variance of less than or equal to 10 % when the slice thickness was varied. Most of the radiomic texture features were weak and unstable (coefficients of variance above 10%) at very small slice thickness ($< 2.5\ mm$) and robust at medium ($\geq 2.5\ mm$) to large slice thickness ($3.75\ mm\ and\ 5\ mm$) (coefficients of variance ≤ 10 %). The above was attributed to an averaging effect (image smoothening) on the images when the slice thickness of image

acquisition is increased. The image noise was observed to be less in large slice thickness when compared to noise at small slice thickness. Radiomics features were independent and stable to the tube potential at greater than 100 kV. At high tube potential the radiation attenuated signal detected at the CT detector was higher cancelling the noise effects. The robustness of these radiomic features depended on the material comprising the insert analysed.

The extent of mAs dependence observed for the dense cork and plaster resin materials inserts was low compared to the dependence on the solid acrylic material insert. All the other phantom inserts (rubber particles, natural cork and the 3 acrylonitrile butadiene styrene plastic) data plots showed smaller variations around the central axis (zero feature value) of the skewness, uniformity, entropy and kurtosis features graphs. Irrespective of the mAs changes, the radiomic texture feature values obtained from all of the ABS materials inserts, rubber particles and natural cork inserts were consistently smaller, closer to zero. A general decrease in image noise as the mAs of image acquisition was increased in images of uniform or relatively uniform material was also observed.

The patient tumour analysis showed some radiomic texture features response to radiotherapy treatment. This was shown by the changes observed on the inverse difference, inverse difference moment, entropy and difference variance texture features. The texture features had their values decrease from start of treatment (first fraction) to the last treatment fraction. The decrease was not smooth along the treatment period, there were some anomalies on the trends. This decrease was ascribed to the change in the heterogeneity of the tissues within the treatment region of interest evaluated.

Conclusion: Overall, using theoretical analysis and a practical approach, robust radiomic features that were independent of the CT scan parameters were observed. The experimental approach showed that the phantom insert materials had influence on radiomic texture feature values obtained in investigations. Radiomic texture features demonstrated that tumours had a variation of heterogeneity between them. The observation agrees with other clinical studies that showed that tumours exhibit some extensive genetic and phenotypic variations. Radiomic texture features can be utilised to depict tumour texture changes along the treatment timeline as shown in this study. A great challenge would be to associate the radiomic texture feature changes to the clinical biological changes. For future robust radiomic feature studies, the use of phantoms with tissue like materials was proposed.

Key words: 1.) Radiomic Texture features, 2.) Computed Tomography, 3.) Tumour, 4.) Phantom, 5.) Imaging parameters, 6.) Robust, 7.) Slice thickness, 8.) Tube potential difference, 9.) Tube current, 10.) Software

TABLE OF CONTENTS

TABLE OF FIGURES

LIST OF TABLES

ABBREVIATIONS LIST

2D	- Two dimensional
3D	- Three dimensional
ABS	- Acrylonitrile Butadiene Styrene plastic
Adeno	- Adenocarcinomas
CBCT	- Cone Beam Computed Tomography
CCR	- Credence cartridge radiomics
CT	- Computed tomography
COV	- Coefficient of Variance
FOV	- Field of View
f_n	- Normalised feature value
GLCM	- Grey-Level Co-occurrence Matrix
GLDM	- Grey Level Dependence Matrix
GLRLM	- Grey Level Run Length Matrix
GLSZM	- Grey Level Size Zone Matrix
Gy	- Gray
HU	- Hounsfield Units
HX	- the entropy of p_x
HXY	- Entropy in the X and Y co-occurrence matrix rows relationship
HY	- the entropy of p_y
Id	- Inverse Difference
Idm	- Inverse Difference Moment
Idmn	- Inverse Difference Moment Normalized
Idn	- Inverse Difference Normalised

Imc1	- Information measures of correlation 1
Imc2	- Information measures of correlation 2
kV or kVp	- Kilovoltage peak
LET	- Linear energy transfer
mAs	- Tube current time product
Mg	- milligrams
MSCT	- Multi-slice computed tomography
Ng	- Discrete intensity levels
NGTDM	- Neighbourhood Grey Tone Difference Matrix
NGTM	- Neighbourhood Grey Tone Matrix
p	- Intensity histogram
PDF	- Probability density function
Pixels	- Picture elements
PTV	- Planning target volume
QC	- Quality control
RBE	- Relative biological effectiveness
ROI	- Region of Interest
RT	- Radiotherapy treatment
SFOV	- Scan Field of View
SNR	- Signal to Noise ratio
Squam	- Squamous cell carcinomas
SSCT	- single slice computed tomography
Voxels	- Volume elements
$\leq$	- Less than or equal to

Chapter 1: General Introduction

1.1 Introduction

The thesis seeks to give an insight into the study that aimed to investigate the effect of CT scan parameters on radiomic texture features by imaging and analysing images of an invariant phantom. The investigation also established robust radiomic features that are independent of the CT scan technique variables. This was done by analysing the mathematics of quantitative radiomic features from the basic CT image formation physics point of view.

1.1.1 Computed tomography (CT)

CT is a reproducible non-invasive imaging modality that utilises ionizing radiation for depicting small (down to the size of about 0.6 mm in diameter) and/ or large human structures to reveal a large range of pathological processes such as cancer and inflammation in clinical practice. The information portrayed by CT images is considered reproducible and objective (Fletcher et al., 2016). CT has found use in all hospital cancer management departments (diagnostic radiology, nuclear medicine and radiation oncology) mainly because of its potential to acquire relatively high-resolution images with volume element (voxels) sizes of approximately 1 mm^3 (Gillies, 2012). CT image formation follows Lambert-Beer's law (Manmadhachary et al., 2017; Chityala et al., 2011)(represented by equation 1) in that each image represents scaled normalized x-ray attenuation values for the voxel within the slice imaged. Variation in the x-ray attenuation (object or patient contrast) by absorption or scattering in dissimilar types of tissue results in differences in the intensity of the x-rays eventually reaching the CT detectors (Goldman, 2007). Each data point on the image is then represented by the CT number per pixel.

$$\varphi = \varphi_0 \times e^{-\sum_i \mu x_i} \quad (1)$$

Where, φ is the beam intensity received by the CT unit (shown in fig 1) radiation detectors after attenuation, φ_0 is the initial beam intensity, μ is the linear attenuation coefficient in cm^2/g of the individual ray-line (i) and x_i is the mean mass thickness in g/cm^2 of the features in the x-ray path.

A matrix of the x-ray intensities that represent the CT numbers (measured in Hounsfield Units, HU) of all the points within an imaged slice obtained at the detectors will then be reconstructed into a map of voxels (represented by the picture elements (pixels) in the image). The quality of the images produced by a CT unit is determined by the fidelity of the CT numbers, accurate reproduction of low-contrast resolution (small differences in attenuation) and the precise depiction of small, closely spaced objects (spatial resolution). Thus, the integrity of the quality assurance program implemented on the CT unit establishes the calibre of images produced.

Radiomics uses computed tomography digital images to derive quantitative image features. The quantitative image features developed by radiomics techniques have both spatial resolution (voxel size) and contrast (grey-level/density) resolution (Lu et al., 2016). The quality of the spatial resolution and density resolution on images

is influenced by the x-ray intensities received at the detector end of the CT unit which is determined by image acquisition techniques and parameters.

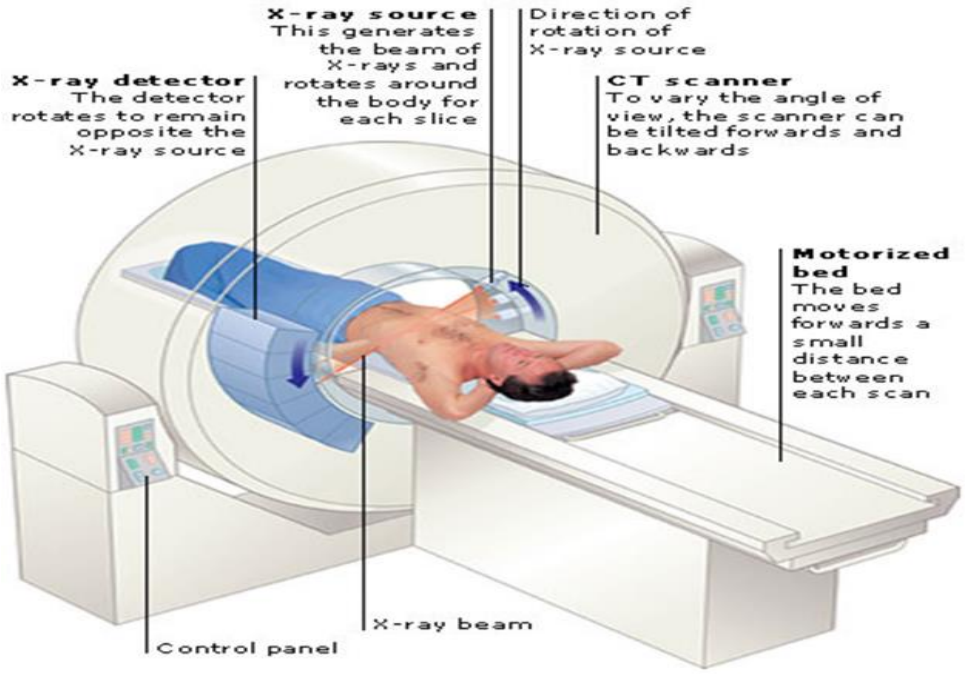

Fig 1. A CT scanner model showing the basic scanning position of a patient. The schematic diagram shows the corresponding X-ray source and detectors positions and their relative rotational motion inside the CT scanner gantry. (Courtesy of the Medical Encyclopaedia)

1.1.2 CT factors that influence image formation and quality

1.1.2.1 Slice thickness

Slice thickness is an imaging parameter (usually from a sub-millimetre scale to 10 mm) that is usually predetermined by the centre's imaging protocols or is selected by the Operator to fulfil the clinical imaging obligation. Studies have shown that the slice thickness affects image resolution in that high spatial resolution within an image is produced by acquiring the image through the use of small slice thickness which is also associated with large data sets (Ford and Decker, 2016). This is due to the reduced tissue signal averaging in the slice direction thus better definition of tissue interfaces can be achieved, but this comes at the cost of detected signal intensity. The detectors collect more photons over thicker slices to establish good low-contrast resolution. Essentially CT image noise affects the potential to resolve low-contrast structures. Quantum mottling significantly contributes to the CT image noise due to the fact that quantum noise depends on the number of x-ray photons contributing to the image (Goldman, 2008). Increasing the number of photons received at the detectors results in a decrease in the image noise (Zukhi and Yusob, 2017). Images acquired using small slice thicknesses (e.g. 1-2 mm), are prone to noise and images acquired using larger slice thicknesses

can be affected by the partial volume effect artefact. Slice thickness is the full width at half maximum (FWHM) of the sensitivity profile, in the centre of the scan field.

1.1.2.2 Scan field of view (SFOV)

SFOV is referred to as the maximum selectable volume (field) to be imaged that gives a reconstructed image (Salemi et al., 2016). The SFOV is usually selected by the radiographer operating the machine who, under the guidance of the radiologist or by standard protocols and clinical judgement, selects a field that covers all the areas of possible disease that needs to be imaged. A smaller SFOV than required might exclude the required structure from the visible image produced after imaging. The quality of an image depends on the SFOV in that a small SFOV increases the spatial resolution in the image. This is because by selecting a small SFOV the whole reconstruction matrix is used for a smaller region resulting in the reduction of the pixel size which is determined by dividing the SFOV by the matrix size. In most cases, using a fixed number of pixels means that selection of a larger SFOV will decrease resolution due to larger voxels.

1.1.2.3 Pitch

Goldman L (Goldman, 2008) produced two distinct pitch definitions that relate to whether the type of the CT scanner is a single slice CT (SSCT) or multi-slice CT (MSCT). Detector pitch is related to an SSCT whilst MSCT relates to beam pitch. Detector pitch is defined as the table increment during a single gantry rotation divided by beam width. A pitch of 1 would mean the scan table moves a distance equal to beam collimation width per single tube rotation. A pitch greater than 1, the couch moves a distance greater than the x-ray beam collimation per scan rotation. This means gaps between adjacent x-ray beams creating a helix. This result in reduced image quality (low signal-to-noise-ratio) but with less dose give to the patient. Lower than a pitch of 1 the x-ray beams overlaps irradiating a volume more than once per scan. There is no patient dose saving due to slow scan speed at lower pitch settings. Beam pitch is defined as table increment in a single gantry rotation divided by the total thickness of all simultaneously acquired slices. Helical MSCT acquired images can be noisier if many detector samples are used for slice measurements such that fewer x-ray photons contribute to each calculated slice sample for larger pitches. If the helical MSCT pitch is increased for the same x-ray technique parameters (kVp and mAs), the number of photons contributing to images decreases linearly. Therefore, "effective" mAs (mAs_{eff}) is usually specified by some manufacturers, to maintain the same level of image noise regardless of the pitch. If scanners employ effective mAs no dose considerations will be involved as the mAs will be adapted to pitch to maintain constant image noise. Lower pitch settings assist in reducing spiral artifacts (Nagel, 2007). The mAs_{eff} is calculated as follows

$$mAs_{eff} = {}^{mAs}/_{pitch} \quad (2)$$

1.1.2.4 Exposure technique parameters

Exposure technique parameters (factors) refer to the machine settings of x-ray tube voltage (kVp), tube current (mA) and exposure time (s) that are either operator selected or automatically selected by the unit for a given study (Goldman, 2007, 2008). A higher kVp would mean more x-rays penetrate the subject under investigation to reach the detectors. The quantity of the x-rays produced will be increased and the x-ray beam energy is also increased. A higher tube current would substantially increase the x-ray intensity thus the number of x-rays photons detected would also increase proportionally (assuming no change in the tube voltage). A faster rotation time corresponds to shorter detector sampling times. The product of tube current and rotation time (mAs) is a common parameter which embodies the characteristic function of mA and s separately. An increase in mAs decreases the image noise thus resulting in improved image quality with more distinct pixel values. mAs is directly proportional to dose, so an increase in mAs will increase dose. A selection of mAs values which do not considerably increase the dose to the patient with limited image quality benefit is usually recommended.

1.1.2.5 Reconstruction matrix and algorithm

A CT image is made up of a square image with rows and columns of pixels that ranges in size from 256 x 256 to 1024 x 1024 (Flores et al., 2015). The reconstruction algorithm consists of an algorithm that includes application of a filter and a kernel to the projection data acquired. The mathematical algorithm filter suppresses the smearing by back-projections that occurs during image reconstruction and the kernel reduces the noise that would have been enhanced by the high-pass or sharper filter (Geyer et al., 2015). Several algorithms that assist in achieving specific clinical imaging requirements are available. For example, soft tissue algorithms for examining more soft tissue organs like the abdomen, or the head, exist for most CT scanners. High-resolution algorithms which provide greater spatial resolution, for detailed representation of bone and other regions of high natural contrast such as the lungs and spine, also exist. The algorithm selected for each image reconstruction strongly affects the appearance and the characteristics of the CT image. Algorithms must thus be carefully selected depending on the application, or clinical use to which any specific CT examination is to be put.

One of the main areas of application of CT imaging is in the field of cancer detection and treatment. CT uses include cancer screening, detection and staging, guidance in tissue extraction procedures (biopsy), treatment planning, image-guided treatment (Cone Beam CT) and post-treatment assessments. During radiotherapy preplanning processes, CT is widely used because of easy and robust assignment of electron densities to the scanned image structures which has an application in the treatment planning dose calculations. Other imaging modalities such as Magnetic Resonance Imaging (MRI), Ultrasound Imaging, Positron Emission Tomography (PET) imaging and Single-Photon Emission Computed Tomography (SPECT) find widespread and meaningful usage in clinical scenarios that require knowledge of the patient's physiological processes and functions.

1.1.3 General Radiomics

Radiomics seeks to distinguish and extract information about tissue structures in an image. Texture analysis is applied to quantify these tissue structures and thereby differentiate or identify similar image features. Image segmentation and shape identification are the pre-processing steps that are employed to classify, segment and identify feature shape (Srinivasan and Shobha, 2008). In a multi-textured image, segmentation establishes demarcations between regions of different textures and these boundaries should be simple, smooth and spatially accurate (Padayachee et al., 2006). The same technique of texture analysis may be employed to track variations in the tumour response to treatment by quantifying tissue texture differences pre-treatment, on-treatment and post-treatment. Texture analysis is a procedure for measuring and assessing digital image characteristics by evaluating the relative position and intensity of signal features. Texture represents stochastic grey scale variations in an image. The spatial variation of pixels/ voxels and their grey-level intensity define the textures within a digital image or region of interest in an image (Beckers et al., 2017). Textures are therefore mathematical parameters computed from the distribution of pixel intensities, which distinguishes the tissue structures revealed in the image (Nailon, 2012; Srinivasan and Shobha, 2008; Castellano et al., 2004). The human eye will perceive a texture in terms of roughness (coarse/fine), smoothness, regular and irregular (Haralick et al., 1973) whereas computer-aided image analysis can quantify textures which the eyes cannot readily perceive or quantify. This means tissue heterogeneities that cannot be perceived by the naked eye can be measured by quantitative texture analysis (QTA) (Zhang et al., 2017). Although radiomic texture features were originally described for projection radiology images, their use in tomographic imaging is more justifiable as overlapping textures and structures are minimized. Therefore, radiomics is seen as a tool that can meaningfully assist in making medical decisions that will be evidence based on texture features that are derived from CT images or any other imaging modality (Bodalal et al., 2018; Tsougos et al., 2018; Lambin et al., 2017).

The general understanding in the classification of the texture of an image is that a group of mutually related pixels compose a texture. Images are characterized by pixels that are established by varying densities in imaged materials. The pixels that define a texture are called primitives or texture elements (Srinivasan and Shobha, 2008).

Various methods are used to analyse texture structures in images;

1) Statistical techniques,
2) Model-based techniques,
3) Structural or syntactic and
4) Filter Bank Based Methods

1.1.3.1 Statistical techniques

First-order (1st-order) and second-order (2nd-order) statistical image analysis techniques are estimates of the probability density functions (PDF).

1.1.3.1.1 First-order

1st-order statistical methods refer to images analysis methods that examine the grey-level distributions only. The 1st-order method considers the frequency of a particular grey-level at a random image position and does not consider correlations, or co-occurrences, between pixels.

1.1.3.1.2 Second-order

The 2nd-order statistical image analysis method incorporates an interpretation of pixels spatial location (relative distance among pixels and their relative orientation) in its image grey-scale distribution examination (Kodituwakku, 2014; Stefan, 2012). Computer-aided diagnostic systems widely use statistical methods to analyse a selected region of interest on an image to produce texture information such as the mean, variance, standard deviation etc. The grey-level co-occurrence matrix (GLCM), the grey-tone difference matrix (GTDM), linear discriminant analysis (L_d) and the grey-level run-length matrix method (GLRM) are some of the image processing techniques that are of 2nd-order statistics.

1.1.3.1.3 Grey-level co-occurrence matrix

The image statistical information about the distribution of nearby pixels within a region is described by the GLCM method, also known as the spatial grey-level dependence (SGLD) matrix (Padayachee et al., 2006). GLCM does not only consider the intensity dispersion, but it also considers relative positions. Consider the PDF of an image matrix $p_{d,\theta}(i,j)$ to be represented by $P_{d,\theta}(i,j)$ then the probability of the co-occurrence of grey levels, i and j for two pixels separated by a distance d at an orientation angle θ is represented by an element (i,j). Counting the pairs of pixels separated by a defined number of matrix elements, or the distance, in a particular orientation is used to calculate the matrix.

1.1.3.1.4 Grey-tone difference matrix

GTDM the sum of a set of pixels having a grey-tone, i, of the difference between the voxels of the set and the mean value of a column of elements, $g(i)$, in a matrix, computed over the corresponding neighbourhood. From GTDM, several features can be computed: Coarseness, contrast, busyness, complexity, and strength.

1.1.3.1.5 Linear discriminant analysis

L_d is used to distinguish features in linear combinations of two or more, by setting weights on each feature that can maximize the variance between classes and minimizing variance within the class (Theodoridis and Koutroumbas, 2009).

1.1.3.1.6 Grey level run-length

The GLR technique can be used to compute texture features by considering a set of pixels of constant grey-level, g, spatially located in a straight line of length, r, at an angle, θ, which can be represented by a probability function, $P_\theta(g,r)$ (Alobaidli et al., 2014).

1.1.3.1.7 Grey-level run-length matrix

GLRM probability function, $P_\theta(g,r)$, can be used to define texture features as: long run emphasis, short run emphasis, run-length non-uniformity, run-length percentage and grey-level non-uniformity (Incoronato et al., 2017; Padayachee et al., 2006).

1.1.3.2 Model-based techniques

Model-based methods use the Gaussian Markov random fields and Gibbs random fields techniques. According to Cohen et al. the Gaussian fields method is used to model texture features whilst the Markov random fields (MRF) are used to create boundaries of the textured features (Cohen and Cooper, 1984). The MRF method considers the textural distributions and spatial positions of pixels in an image. Therefore, MRF defines the energy function on a label field to minimize that energy function through optimization. This means model-based methods depend upon making an image model based on certain parameters captured from the fundamental qualities of the studied texture.

1.1.3.3 Structural or syntactic methods

Micro or macro-textures (primitives) are used to represent texture in structural or syntactic methods by quantifying the spatial arrangements of the primitives. Structural descriptors view texture in terms of these texture primitives. To describe the texture, primitives are defined and the rules of placement of these primitives are also established. Syntactic methods are suitable for textures where primitives can be described using a larger variety of properties than just grey level properties for example, shape description (Sepp and Matti, 2005; Vuduc, 1997). Using these properties, the primitives can be identified, defined and assigned a label. For grey-level images, tone can be replaced with brightness.

1.1.3.4 Filter Bank Based Methods

Referred to in other literature as the spectral technique (Padayachee et al., 2006) because it applies the spatial and frequency domains to extract texture features. Filter bank techniques include, but are not limited to Laplacian of Gaussian filter, Gabor filters, wavelet transforms and the Fractal dimensions methods.

1.1.3.4.1 Laplacian of Gaussian filter

The Laplacian of Gaussian filter uses scales that correspond to the width of the filter to highlight structures (Incoronato et al., 2017). 2nd-order statistics can then be applied to an image to extract texture patterns (coarse) from the highlighted structures.

1.1.3.4.2 Gabor filters

Gabor filters are mainly suitable for image segmentation because they use edge detection in different directions and widths to filter image features.

1.1.3.4.3 Wavelet transforms

Wavelet transforms are mathematical algorithms (filters) that cut up data into various distinct frequency (low and high) coefficients to study each component with a resolution matched to its scale without losing spatial localization. High-frequency coefficients contain information on the directionality of the texture. Using a moving variable sized window, wavelets provide a more flexible way of analysing both space and frequency contents of an image (Aggarwal and K. Agrawal, 2012).

1.1.3.4.4 Fractal dimension analysis

Fractal dimension analysis relates the change at which the outer surface area of an object or feature, increases as the scale of measurement gets smaller (Padayachee et al., 2006). Parameters such as mean and standard deviation can be extracted (Incoronato et al., 2017).

A summary of the textural feature extraction and classification approaches established on the above methods.

Frequency based methods are considered less efficient, while statistical methods are particularly useful for random patterns or textures. Syntactic or structural methods give better results in complex patterns analysis. Potential limitations exist in radiomics image analysis. The diverse radiomic texture features applied in clinical trials and clinical practices present challenges in that the acquisition parameters are not standardized. A wide range of imaging equipment, acquisition techniques and reconstruction parameters have been identified to be possible limiting factors that influence the computed values of quantitative image features (Lu et al., 2016). There exist studies that focused on texture variation caused by the intra- and inter-variability between tumours, and/ or scanner differences (Mackin et al., 2015). Mackin et al.'s investigation showed that the calculated image texture feature parameters without filtering are likely to be influenced by differences in the imaging protocols or CT scanner type (Larue et al., 2017; Mackin et al., 2015). In this study, image texture analysis would give attention to investigate robust texture characteristics or features that are either independent or dependent on the machine scan parameters using a non-variant phantom. The nature of a textured object can be mapped by

applying mathematical algorithms to generate patterns that characterize the different features existing in the object of interest. Invariant mathematical vectors produced by image processing algorithms would represent a uniform feature (cluster), which would be well separated from measurement vectors that correspond to different textures. In this sense, texture analysis can be considered as a pattern recognition or classification technique.

Review papers by Sanduleanu et al. and Alobaidle et al. state that most studies have shown the prognostic power of radiomic features in diagnostic radiology radiomics studies and the potential of predicting effects of irradiation in therapy (Sanduleanu et al., 2018; Alobaidli et al., 2014). Huynh et al. in their study of radiomics analysis of stereotactic body radiation therapy patients with lung cancer concluded that radiomics quantification has greater prognostic power than conventional data in predicting distant metastases and radiomics has power to predict survival rate (Huynh et al., 2016). Panth et al. found that 'the feature value for slow-growing tumours (gene-induced) was higher than for faster-growing tumours (no gene-induced group) upon combination with radiotherapy'. They concluded that there is a relationship between the genetic tumour changes and early effects of radiation treatment (Panth et al., 2015).

1.1.4 Study Problem Statement

There is little evidence in the published literature of studies that use mathematics to establish radiomic features that are independent of the CT scan technique parameters. Most studies published use experimental tests to assess robustness of radiomic features. In the South Africa context of studies, this research will be a novel study in the mathematical identification of robust radiomic features that are independent of the CT scan technique parameters. Around the world few studies (Mackin et al., 2015, 2017; Zheng et al., 2017; Lu et al., 2016) have been carried out to determine how acquisition parameters influence the computed values of quantitative image features in radiomics studies. Some radiomics studies have been conducted to investigate the impact that tumour volume had on radiomic texture features (Shafiq-ul-hassan et al., 2018; Byrd et al., 2015). It was observed through these studies that the tumour volume and other parameters such as pixel size, acquisition noise, lesion size, phantom size, and reconstruction method have some influence on the radiomic texture features values.

The stability of radiomic texture features may have a great impact on the diagnosis, segmentation and treatment of cancers. Stable radiomic features that remain relatively constant at constant physical acquisition parameters can be used to track radiotherapy treatment response by observing their behaviour throughout administration of the treatment course. In order to achieve the above, there is need to use an invariant test tool to investigate quantifiable image features at variable physical acquisition parameters. The findings of this study will assist in determining the correlation between radiomic features acquired in different imaging settings (e.g. scanner type, hospital, reconstruction algorithms) making it possible to compare different extracted feature values.

Already many studies performed using the Credence Cartridge Radiomics (CCR) phantom have demonstrated that imaging exposure and reconstruction settings have influence on radiomic feature values. Shafiq-ul-Hassan et al (Shafiq-ul-hassan et al., 2018) examined the effects of sampling voxel-size on the radiomic features. The study discovered that normalising the voxel-size or resampling image information using a nominal voxel size minimizes the dependency of radiomic features on voxel size. Also, Mackin et al. (Mackin et al., 2015) used the CCR phantom at four different manufacturer CT scanners. The researchers showed that radiomics texture features presented an estimated variance. Differences in the scanning protocol employed was reported to cause the intra-scanner variabilities.

1.1.5 Study Aim and Objectives

This study aims to determine the effect of CT scan parameters on radiomic texture features by imaging an invariant phantom. The investigation seeks to mathematically establish robust radiomic features that are independent of the CT scan technique variables.

The three objectives of the investigation are as follows:

- Identification of imaging parameter invariant radiomic features.
- Determine the intra- and inter-scanner variability of radiomic features using the Credence Cartridge Radiomics phantom.
- Retrospective application of identified robust radiomic texture features onto a clinical data set.

Chapter 2: Texture features and their relation to CT image formation

2.1 Introduction to theoretical robust radiomic features recognition

The purpose of this chapter 2 is to use the general principles of treating radiomic image features equations to fundamentally examine the level of radiomic features stableness in relation to CT imaging technique parameters. The features robustness is of critical significance for radiomic studies in that the use of robust features will ensure reproducibility in different studies and will assist to accurately prognosticate the subject of interest (Zwanenburg et al., 2019). This chapter investigated the effects of CT imaging parameters on the radiomic features at basic levels. The chapter intents to accomplish part of the objective that seeks to identify some robust radiomic features. Basic hand calculations using theoretical radiomic texture feature equations and image matrices extracted from the Credence Cartridge Radiomics phantom (CCR) images obtained on CT units.

This part of the study focussed on the theory of CT image formation against the CT techniques to relate image quality changes to radiomic features degree of variation. The thrust of using images in the radiology and oncology departments depends on the ease with which image information can be used to make clinical decisions. Radiomics is a branch of study that strives to improve personalised cancer care using images. Fundamental interpretations of the way CT scan techniques affects the radiomic features is required. Several studies (Mackin et al., 2018; Mahmood et al., 2017; Fave, 2015) have drawn conjectures about the robustness of radiomic texture features. The study by Larue et al. is of particular interest in this study, in that they could not find any correlation between CT slice thickness or tube current with radiomic texture features (Mackin et al., 2018).

2.1.1 CT Image quality

The image contrast, spatial resolution, image noise and artifacts are the four fundamental factors that interact to define the image details (Zukhi and Yusob, 2017b; Katkar et al., 2016; Goldman, 2007).

In CT imaging, contrast is influenced by the differences in the intensity of the x-rays ultimately reaching the detectors as a result of differential x-ray attenuation in different types of tissue. Image contrast resolution refers to the ability of an imaging procedure to consistently discern subtle differences in image density between tissues of closely similar grey level values.

Spatial resolution refers to the ability of the imaging unit to show on an image small objects that are close together, as separate objects. Spatial resolution in CT imaging is mainly determined by the size of the detector and the spacing between the sampling measurements. A reasonable spatial resolution is usually achieved if the size of the detector is comparable to the size of the objects to be resolved and sampling measurements spacing that is closer together.

The factors contrast and spatial resolution influence the signal-to-noise ratio (SNR) of an image. Both affect the x-ray quanta used to formulate structures per pixel in an image. Bushberg et al. pointed out the superiority

of the CT imaging modality's contrast resolution capabilities to other x-ray modalities (Bushberg et al., 2002). The contrast resolution capability of CT stands out in differentiating subtle soft tissue tumours. In clinical situations which the CT number difference between the tumour and the surrounding tissue is small (e.g., 20 CT numbers), and the noise in the CT numbers is smaller (e.g., 3 CT numbers), the tumour and surrounding tissues can be distinguished to a trained human observer or algorithm (Alsleem et al., 2013; Bushberg et al., 2002). On the other hand, attempting to increase the spatial resolution at constant FOV and dose levels by reducing the voxel size would reduce the number of x-rays per voxel. The reduction of the x-ray quanta per voxel would decrease the SNR, therefore a compromise between spatial resolution and contrast resolution is usually recommended. In relation to the above theory, radiomic texture features that depend on the pixel intensity distribution are therefore expected to be influenced by the factors that affect the contrast and spatial resolutions.

Image noise is the random fluctuations in the CT number of otherwise uniform materials observed on CT images. CT image noise is attributed to the limited number of photons to form an image and this is associated to the number of x-rays contributing to each detector measurement.

There is a known linear relationship between the slice thickness and the number of x-rays detected by the detector at a constant kV and mAs. The slice thickness in CT imaging affects the beam width entering the detector in a manner in which doubling the slice thickness approximately doubles the number of photons reaching the detector (Goldman, 2007). An improved contrast resolution and a higher SNR are achieved at larger slice thicknesses due to the increase in the number of x-rays detected for the same x-ray tube techniques. Under similar conditions, the spatial resolution is expected to be reduced due to the beam width increment, and partial volume effects become pronounced. To improve spatial resolution thin slices at increased mAs will partially compensate for the loss of x-ray photons due to the x-ray collimation. The usefulness of images is certain if there is increased SNR and reduced noise (Alsleem et al., 2013).

The combination of tube amperage and scan time (mAs) influence the beam intensity and the number of x-rays reaching the detector in a proportional manner. This affects the image noise in such that an increase in the mAs reduces the image noise because the number x-ray photons to be detected would increase proportionally.

The peak kilovoltage (kV) determines the beam quality of a CT x-ray beam. The kV defines the beam strength and influences the beam intensity to a certain extent. An increase in the kV increases the number of x-rays photons and the average energy of the x-ray beam. This promotes a greater number of x-rays to penetrate the object to reach the CT detectors. Image noise is expected to be reduced because of increased signal detected. Also the image contrast is expected to be enhanced due to the noise reduction, the higher the tube potential, the better the contrast-to-noise ratio (CNR) (Nagel, 2007).

There is a need to investigate the kV, mAs and slice thickness's influence on the probability density function of the ROI grey level intensities on CT images. This may assist the researchers to understand radiomic features robustness in relation to changes that might be formed on CT images due to the scan techniques.

2.1.2 First order statistical features

The first order features represent the distribution of the voxel intensities in an image within a defined region of interest (ROI). Let us consider $P(i)$ the density occurrence probability of a random grey level intensity i within an ROI drawn on an image I. The image I is such that $I(x,y) = i$ where (x,y) represents the voxel position (van Griethuysen et al., 2017). The normalised first order histogram $p(i)$ will be equal to $\frac{P(i)}{\sum P(i)}$. The grey level intensities i range from 0 to $Ng - 1$. Where Ng represents the discrete intensity levels

$$p(i) = \frac{P(i)}{\sum P(i)} = \frac{number\ of\ voxels\ with\ gray\ level,\ i,\ within\ a\ ROI}{total\ number\ of\ voxels\ in\ the\ ROI(N_p)} \quad (3)$$

Let us consider the fig 2 a two-dimensional 5x5 image

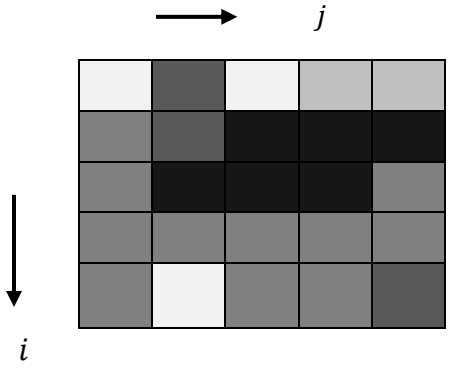

Fig 2. Two-dimensional (2D) image

Below is Fig 3 that represents the Key for reading the grey scale images

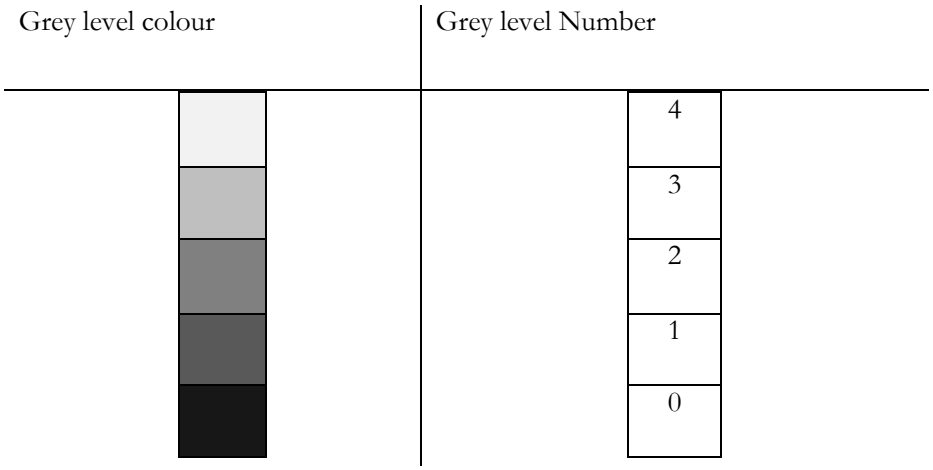

Fig 3. Grey tone colour and the corresponding level

The original image in fig 2 can be represented by the image matrix $P(i)$ in Fig 4. The grey-level intensities (N_g) range from 0 to 4.

$$P(i) = \begin{matrix} \text{Grey Level} \\ [0 \quad 1 \quad 2 \quad 3 \quad 4] \end{matrix} \quad \begin{matrix} \begin{bmatrix} 4 & 1 & 4 & 3 & 3 \\ 2 & 1 & 0 & 0 & 0 \\ 2 & 0 & 0 & 0 & 2 \\ 2 & 2 & 2 & 2 & 2 \\ 2 & 4 & 2 & 2 & 1 \end{bmatrix} \end{matrix} \quad \begin{matrix} \\ \begin{bmatrix} 0 \\ 1 \\ 2 \\ 3 \\ 4 \end{bmatrix} \end{matrix} \quad \text{Grey Level}$$

Fig 4. 5x5 grey scale image matrix

Equation 3 was used to formulate a normalized first order histogram $p(i)$,

$$p(i) = \begin{bmatrix} 0.09 & 0.02 & 0.09 & 0.07 & 0.07 \\ 0.05 & 0.02 & 0.00 & 0.00 & 0.00 \\ 0.05 & 0.00 & 0.00 & 0.00 & 0.05 \\ 0.05 & 0.05 & 0.05 & 0.05 & 0.05 \\ 0.05 & 0.09 & 0.05 & 0.05 & 0.02 \end{bmatrix}$$

Fig 5. 5x5 normalized grey scale image matrix

Mean (μ) feature

The mean grey level intensity μ of $p(i)$ (Fig 5) will be given by the equation 4 below:

$$\mu = \sum_{i=0}^{N_g-1} i \cdot p(i)$$

$$\mu = \sum_{i=0}^{4} i \cdot \begin{bmatrix} 0.09 & 0.02 & 0.09 & 0.07 & 0.07 \\ 0.05 & 0.02 & 0.00 & 0.00 & 0.00 \\ 0.05 & 0.00 & 0.00 & 0.00 & 0.05 \\ 0.05 & 0.05 & 0.05 & 0.05 & 0.05 \\ 0.05 & 0.09 & 0.05 & 0.05 & 0.02 \end{bmatrix} \quad (4)$$

$$\mu = 0 \times 0.09 + 0 \times 0.02 + 0 \times 0.09 + 0 \times 0.07 + 0 \times 0.07 + 1 \times 0.05 + 1 \times 0.02 + 1 \times 0 + 1 \times 0 + 1 \times 0 + 2 \times 0.05 + 2 \times 0 + 2 \times 0 + 2 \times 0 + 2 \times 0.05 + 3 \times 0.05 + 3 \times 0.05 + 3 \times 0.05 + 3 \times 0.05 + 3 \times 0.05 + 4 \times 0.05 + 4 \times 0.09 + 4 \times 0.05 + 4 \times 0.05 + 4 \times 0.02$$

$$\therefore \mu = 2.06$$

The mean feature of the grey level intensity within the normalised image matrix in fig 2 is 2.06. Studies by Alshipli and Kabir (Alshipli and Kabir, 2017), Katkar et al. (Katkar et al., 2016) and He et al. (He et al., 2016) showed that image noise has an inverse proportionality with slice thickness. If the slice thickness used to acquire the image in fig 2 is changed to a larger slice thickness, the contrast detail of the image is expected to improve as the noise is being reduced. The study by Alshipli and Kabir (Alshipli and Kabir, 2017) has demonstrated that large slice thicknesses reduce the image noise but the diagnostic content is compromised. Katkar (Katkar et al., 2016) concluded that the CT image detail is better at the smallest slice thickness in spite of the higher noise. The partial volume effect has been identified as the cause for the loss of fidelity on the representative anatomy in images acquired at a large slice thickness. The above analyses and observations fit well with homogenous images that are usually obtained in quality control test phantoms such as the CATPHAN uniformity slice insert or water phantoms.

2.1.3 Grey-Level Co-occurrence Matrix (GLCM) Features

GLCM represents the second-order joint probability function of an image within a defined region of interest (ROI). The GLCM was proposed and introduced in 1973 by Haralick et al. (Haralick et al., 1973). The Haralick et al. paper proposed extracting the texture features by first computing the co-occurrence matrix followed by calculating the texture features based on the created co-occurrence matrix. The GLCM follows the rule that the number of times the combination of grey-levels i and j occur in two voxels in an image that are separated by a distance, d, represented by the number of voxels in a given direction ($\theta = 0, 90, 270\ or\ 135$).

Let us consider Fig 6 a 2D 5x5 image

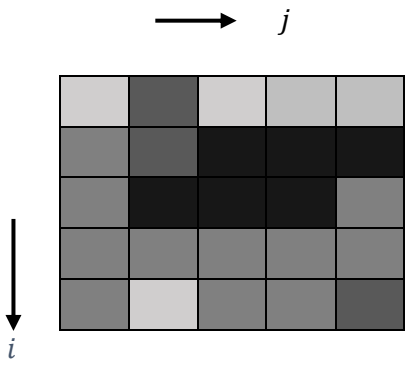

Fig 6. Two-dimensional image

The image in Fig 7 can be represented by an image matrix $P(i)$. In this case the grey-level intensities ($N_g - 1$) range from 0 to 4.

$$P(i) = \begin{bmatrix} 4 & 1 & 4 & 3 & 3 \\ 2 & 1 & 0 & 0 & 0 \\ 2 & 0 & 0 & 0 & 2 \\ 2 & 2 & 2 & 2 & 2 \\ 2 & 4 & 2 & 2 & 1 \end{bmatrix}$$

Fig 7. 5x5 grey scale image matrix

$$P(i) = \begin{bmatrix} 4 & 1 & 4 & 3 & 3 \\ 2 & 1 & 0 & 0 & 0 \\ 2 & 0 & 0 & 0 & 2 \\ 2 & 2 & 2 & 2 & 2 \\ 2 & 4 & 2 & 2 & 1 \end{bmatrix} \quad \begin{bmatrix} 8 & 1 & 2 & 0 & 0 \\ 1 & 0 & 2 & 0 & 2 \\ 2 & 2 & 10 & 0 & 2 \\ 0 & 0 & 0 & 2 & 1 \\ 0 & 2 & 2 & 1 & 0 \end{bmatrix} \quad \begin{bmatrix} 0.21 & 0.03 & 0.03 & 0.00 & 0.00 \\ 0.03 & 0.00 & 0.05 & 0.00 & 0.05 \\ 0.05 & 0.05 & 0.26 & 0.00 & 0.05 \\ 0.00 & 0.00 & 0.00 & 0.05 & 0.03 \\ 0.00 & 0.05 & 0.05 & 0.03 & 0.00 \end{bmatrix}$$

5 x 5 Image matrix Symmetric GLCM Normalized GLCM

Fig 8. GLCM of 5x5 matrix of an image for distance $d = 1$ and direction $\theta = 0^o$

The symmetrical GLCM matrix in Fig 8 is obtained by counting the pairs of voxels within a distance of 1 pixel from each other and an angle $\theta = 0 \; or \; 180$ (horizontal plane, i.e. voxels to the left and right of the centre voxel) of the 5x5 image matrix. The 5x5 matrix in Fig 7 was obtained from reading the grey scale level voxel values of the image in Fig 6. It must be noted that the angles of calculating a co-occurrence matrix can also be considered in the vertical directions, $\theta = 90, 270$, and diagonal directions $\theta = 45, 135, 225 \; and \; 315$.

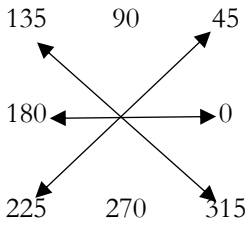

Fig 9. Some of the directions that are used to calculate the co-occurrence matrices

Some radiomics studies use the asymmetry matrices (GLCM obtained by counting the voxel pairs in a single direction only, to the right only or left only etc.) in their investigations whilst others use the symmetry matrices. In this study, only the symmetric GLCM matrices were explored. The GLCM matrix can be normalised by dividing each of the created GLCM matrix cell intensity by the total cell intensities of the GLCM matrix using equation 3 ($p(i,j) = \frac{P(i,j)}{\sum P(i,j)}$), where $P(i,j)$ is the co-occurrence matrix, $\sum P(i,j)$ is the total voxel intensities within the image or region of interest in an image and $p(i,j)$ is the normalised co-occurrence matrix.

Below are examples of the mathematical calculations performed for the 13 texture features following the Haralick's texture feature equations. The Normalised GLCM in Fig 8 was used to perform the calculations.

Mean feature

The mean feature (μ) is calculated as below

$$\mu = \sum_{i=0}^{N_g-1} i \cdot p(i,j)$$

$$\mu = 0 \times 0.21 + 0 \times 0.03 + 0 \times 0.03 + 0 \times 0 + 0 \times 0 + 1 \times 0.03 + 1 \times 0.03 + 1 \times 0 + 1 \times 0.05 + 1 \times 0 + 1 \times 0.05 + 2 \times 0.05 + 2 \times 0.05 + 2 \times 0.26 + 2 \times 0 + 2 \times 0.05 \quad (5)$$

$$\therefore Mean\ feature = 0.98$$

Energy feature

The Energy or angular second moment (ASM) feature is calculated as follows;

$$Energy = \sum_{i=0}^{N_g-1} \sum_{j=0}^{N_g-1} p(i,j)^2$$

$$Energy = (0.21)^2 + (0.03)^2 + (0.03)^2 + (0.03)^2 + (0.05)^2 + (0.05)^2 + (0.05)^2 + (0.05)^2 + (0.26)^2 + (0.05)^2 + (0.05)^2 + (0.03)^2 + (0.05)^2 + (0.05)^2 + (0.03)^2 \quad (6)$$

$$\therefore Energy = 0.13$$

Variance feature

The Variance feature (σ^2) is used to measure the dispersion difference between the reference pixel and its neighbouring pixels.

$$\sigma^2 = \sum_{i=0}^{N_g-1} \sum_{j=0}^{N_g-1} (i-\mu)^2 p(i,j)$$

$$\begin{aligned}\sigma^2 = {} & (0-1.69)^2 \times 0.21 + (0-1.69)^2 \times 0.03 + (0-1.69)^2 \times 0.03 + (0-1.69)^2 \times 0 + \\ & (0-1.69)^2 \times 0 + (1-1.69)^2 \times 0.03 + (1-1.69)^2 \times 0 + (1-1.69)^2 \times 0.05 + (1- \\ & 1.69)^2 \times 0 + (1-1.69)^2 \times 0.05 + (2-1.69)^2 \times 0.05 + (2-1.69)^2 \times 0.05 + (2-1.69)^2 \times \\ & 0.26 + (2-1.69)^2 \times 0 + \ (2-1.69)^2 \times 0.05 + (3-1.69)^2 \times 0 + (3-1.69)^2 \times 0 + (3- \\ & 1.69)^2 \times 0 + (3-1.69)^2 \times 0.05 + (3-1.69)^2 \times 0.03 + (4-1.69)^2 \times 0 + \ (4-1.69)^2 \times \\ & 0.05 + \ (4-1.69)^2 \times 0.05 + \ (4-1.69)^2 \times 0.03 + \ (4-1.69)^2 \times 0\end{aligned} \tag{7}$$

$$\therefore \sigma^2 = 1.65$$

The standard deviation (σ) is therefore calculated as the square root of the variance feature.

$$\therefore \sigma = \sqrt{1.65} = 1.29 \tag{8}$$

Entropy feature

Entropy refers to the measure of the disorder or chaos within the image pixel arrangement that is irreversible or irremediable. The concept of Entropy is derived from the thermodynamics state of energy lost as heat energy and is irrecoverable.

$$Entropy = -\sum_{i=0}^{N_g-1} \sum_{j=0}^{N_g-1} p(i,j)\, log_2\, p(i,j)$$

$$\begin{aligned}Entropy = {} & -(0.21 \times log_2 0.21 + 0.03 \times log_2 0.03 + 0.03 \times log_2 0.03 + 0 + 0 + 0.03 \times \\ & log_2 0.03 + 0 + 0.05 \times log_2 0.05 + 00.05 \times log_2 0.05 + 0 + 0 + 0 + 0.05 \times log_2 0.05 + \\ & 0.03 \times log_2 0.03 + 0 + 0.05 \times log_2 0.05 + 0.05 \times log_2 0.05 + 0.03 \times log_2 0.03 + 0)\end{aligned} \tag{9}$$

$$\therefore Entropy = -3.41$$

Contrast feature

The measure of the intensity or grey-level variations between a reference pixel and its neighbouring pixels is calculated using the contrast feature.

$$Constrast = \sum_{n=0}^{N_g-1} n^2 \left\{ \sum_{i=0}^{N_g-1} \sum_{j=0}^{N_g-1} p(i,j)_{|i-j|=n} \right\}$$

$$\begin{aligned} Contrast = {} & (0-0)^2 \times 0.21 + (0-1)^2 \times 0.03 + (0-2)^2 \times 0.03 + (0-3)^2 \times 0 + (0- \\ & 4)^2 \times 0 + (1-0)^2 \times 0.03 + (1-1)^2 \times 0 + (1-2)^2 \times 0.05 + (1-3)^2 \times 0 + (1-4)^2 \times \\ & 0.05 + (2-0)^2 \times 0.05 + (2-1)^2 \times 0.05 + (2-2)^2 \times 0.26 + (2-3)^2 \times 0 + (2-4)^2 \times \\ & 0.05 + (3-0)^2 \times 0 + (3-1)^2 \times 0 + (3-2)^2 \times 0 + (3-3)^2 \times 0.05 + (3-4)^2 \times 0.03 + \\ & (4-0)^2 \times 0 + (4-1)^2 \times 0.05 + (4-2)^2 \times 0.05 + (4-3)^2 \times 0.03 + (4-4)^2 \times 0 \end{aligned} \quad (10)$$

$$Contrast = 1.85$$

Correlation feature

The correlation feature relates a reference pixel to a linearly positioned neighbouring pixel in a co-occurrence matrix. A correlation feature value of 1 would represent a perfect correlation and a 0 value means uncorrelated.

$$Correlation = \frac{1}{\sigma_x \sigma_y} \sum_{i=0}^{N_g-1} \sum_{j=0}^{N_g-1} ijp(i,j) - \mu_x \mu_y$$

$$\begin{aligned} Correlation = {} & (0-1.69)\times(0-1.69)\times 0.21 + (0-1.69)\times(1-1.69)\times 0.03 + (0-1.69)\times(2-1.69)\times 0.03 + (0-1.69)\times(3-1.69)\times 0 + (0-1.69)\times(4-1.69)\times 0 + \\ & (1-1.69)\times(0-1.69)\times 0.03 + (1-1.69)\times(1-1.69)\times 0 + (1-1.69)\times(2-1.69)\times 0.05 + (1-1.69)\times(3-1.69)\times 0 + (1-1.69)\times(4-1.69)\times 0.05 + \\ & (2-1.69)\times(0-1.69)\times 0.05 + (2-1.69)\times(1-1.69)\times 0.05 + (2-1.69)\times(2-1.69)\times 0.26 + (2-1.69)\times(3-1.69)\times 0 + (2-1.69)\times(4-1.69)\times 0.05 + (3-1.69)\times(0-1.69)\times 0 + \\ & (3-1.69)\times(1-1.69)\times 0 + (3-1.69)\times(2-1.69)\times 0 + (32-1.69)\times(3-1.69)\times 0.05 + (3-1.69)\times(4-1.69)\times 0.03 + (4-1.69)\times(0-1.69)\times 0 + (4-1.69)\times(1-1.69)\times 0.05 + \\ & (4-1.69)\times(2-1.69)\times 0.05 + (4-1.69)\times(3-1.69)\times 0.03 + (4-1.69)\times(4-1.69)\times 0 \end{aligned} \quad (11)$$

$$\therefore Correlation = 0.76$$

Homogeneity / Inverse difference moment (Idm) feature

The IDM quantifies the closeness of the GLCM elements distribution to the elements in the GLCM diagonal. IDM measures the homogeneity of an image.

$$IDM = \sum_{i=0}^{N_g-1} \sum_{j=0}^{N_g-1} \left(\frac{1}{1+(i-j)^2}\right) \cdot p(i,j)$$

$$\begin{aligned} IDM = {} & \left(\frac{1}{1+(0-0)^2}\right)\times 0.21 + \left(\frac{1}{1+(0-1)^2}\right)\times 0.03 + \left(\frac{1}{1+(0-2)^2}\right)\times 0.03 + \left(\frac{1}{1+(0-3)^2}\right)\times 0 + \\ & \left(\frac{1}{1+(0-4)^2}\right)\times 0 + \left(\frac{1}{1+(1-0)^2}\right)\times 0.03 + \left(\frac{1}{1+(1-1)^2}\right)\times 0 + \left(\frac{1}{1+(1-2)^2}\right)\times 0.05 + \left(\frac{1}{1+(1-3)^2}\right)\times \\ & 0 + \left(\frac{1}{1+(1-4)^2}\right)\times 0.05 + \left(\frac{1}{1+(2-0)^2}\right)\times 0.05 + \left(\frac{1}{1+(2-1)^2}\right)\times 0.05 + \left(\frac{1}{1+(2-2)^2}\right)\times 0.26 + \\ & \left(\frac{1}{1+(2-3)^2}\right)\times 0 + \left(\frac{1}{1+(2-4)^2}\right)\times 0.05 + \left(\frac{1}{1+(3-0)^2}\right)\times 0 + \left(\frac{1}{1+(3-1)^2}\right)\times 0 + \left(\frac{1}{1+(3-2)^2}\right)\times 0 + \end{aligned} \quad (12)$$

$$\left(\frac{1}{1+(3-3)^2}\right)\times 0.05+\left(\frac{1}{1+(3-4)^2}\right)\times 0.03+\left(\frac{1}{1+(4-0)^2}\right)\times 0+\left(\frac{1}{1+(4-1)^2}\right)\times 0.05+$$
$$\left(\frac{1}{1+(4-2)^2}\right)\times 0.05+\left(\frac{1}{1+(4-3)^2}\right)\times 0.03+\left(\frac{1}{1+(4-4)^2}\right)\times 0$$

$$\therefore IDM = 0.66$$

Sum Average Feature (SA)

$$SA = \sum_{i=0}^{2(N_g-1)} \left(ip_{x+y}(i)\right) \tag{13}$$

Where:

$$p_{x+y}(k) = \sum_{i=0}^{N_g-1}\sum_{j=0}^{N_g-1} p(i,j), \qquad k = i+j, \qquad k = \{0,1,2,\dots,2(N_g-1)\} \tag{14}$$

$$SA = (0\times 0.21)+\left(1\times(0.03\times 0.03)\right)+\left(2\times(0.05+0+0.03)\right)+\left(3\times(0+0.05+0.05+0)\right)+\left(4\times(0+0+.26+0+0)\right)+\left(5\times(0.05+0+0+0.05)\right)+\left(6\times(0.05+0.05+0.05)\right)+\left(7\times(0.03+0.03)\right)+(8\times 0) \tag{15}$$

$$\therefore SA = 3.33$$

Sum Variance Feature (SV)

$$SV = \sum_{i=0}^{2(N_g-1)} (i-SA)^2 p_{x+y}(i)$$

$$SV = ((0-3.33)^2\times 0.21)+\left((1-3.33)^2\times(0.03\times 0.03)\right)+\left((2-3.33)^2\times(0.05+0+0.03)\right)+\left((3-3.33)^2\times(0+0.05+0.05+0)\right)+\left((4-3.33)^2\times(0+0+.26+0+0)\right)+\left((5-3.33)^2\times(0.05+0+0+0.05)\right)+\left((6-3.33)^2\times(0.05+0.05+0.05)\right)+\left((7-3.33)^2\times(0.03+0.03)\right)+((8-3.33)^2\times 0) \tag{16}$$

$$\therefore SV = 4.89$$

Sum Entropy Feature (SE)

$$SE = -\sum_{i=0}^{2(N_g-1)} p_{x-y}(i)\log p_{x-y}(i) \tag{17}$$

$$SE = -\{0.21 \times log0.21 + (0.03 \times 0.03) \times log(0.03 \times 0.03) + (0.05 + 0 + 0.03) \times log(0.05 + 0 + 0.03) + (0 + 0.05 + 0.05 + 0) \times log(0 + 0.05 + 0.05 + 0) + (0 + 0 + .26 + 0 + 0) \times log(0 + 0 + .26 + 0 + 0) + (0.05 + 0 + 0 + 0.05) \times log(0.05 + 0 + 0 + 0.05) + (0.05 + 0.05 + 0.05) \times log(0.05 + 0.05 + 0.05) + (0.03 + 0.03) \times log(0.03 + 0.03) + 0\}$$

$$\therefore SE = 1.93$$

Difference Average Feature (DA)

$$DA = \sum_{i=0}^{N_g-1} i \cdot p_{x-y}(i) \tag{18}$$

Where:

$$p_{x-y}(k) = \sum_{i=0}^{N_g-1} \sum_{j=0}^{N_g-1} p(i,j) \tag{19}$$

$, k = |i-j|, k = \{0, 1, 2, \dots, 2(N_g - 1)\},$

$$DA = 0 \times (0.21 + 0 + 0.26 + 0.05 + 0) + 1 \times (0.03 + +0.05 + 0 + 0.03 + 0.03 + 0 + 0.05 + 0.03) + 2 \times (0.03 + 0 + 0.05 + 0.05 + 0 + 0.05) + 3 \times (0 + 0.05 + 0.05 + 0) + 4 \times (0 + 0) \tag{20}$$

$$\therefore DA = 0.87$$

Difference Variance Feature (DV)

$$DV = \sum_{i=0}^{N_g-1} (i - DA)^2 \cdot p_{x-y}(i)$$

$$DV = (0 - 0.87)^2 \times (0.21 + 0 + 0.26 + 0.05 + 0) + (1 - 0.87)^2 \times (0.03 + +0.05 + 0 + 0.03 + 0.03 + 0 + 0.05 + 0.03) + (2 - 0.87)^2 \times (0.03 + 0 + 0.05 + 0.05 + 0 + 0.05) + (3 - 0.87)^2 \times (0 + 0.05 + 0.05 + 0) + (4 - 0.87)^2 \times (0 + 0) \tag{21}$$

$$\therefore DV = 1.09$$

Difference Entropy Feature (DE)

$$DE = -\sum_{i=0}^{N_g-1} p_{x-y}(i)\, log\big(p_{x-y}(i)\big)$$

$$\begin{aligned} DE = {} & (0.21 + 0 + 0.26 + 0.05 + 0) \times log(0.21 + 0 + 0.26 + 0.05 + 0) + (0.03 + \\ & +0.05 + 0 + 0.03 + 0.03 + 0 + 0.05 + 0.03) \times log(0.03 + +0.05 + 0 + 0.03 + 0.03 + \\ & 0 + 0.05 + 0.03) + (0.03 + 0 + 0.05 + 0.05 + 0 + 0.05) \times log(0.03 + 0 + 0.05 + 0.05 + \\ & 0 + 0.05) + (0 + 0.05 + 0.05 + 0) \times log(0 + 0.05 + 0.05 + 0) + 0 \end{aligned} \tag{22}$$

$$\therefore DE = 1.21$$

Information Measures of Correlation Feature 1

$$Information\ Measure\ of\ Correlation\ 1 = \frac{HXY - HXY1}{\max\{HX, HY\}} \tag{23}$$

Information Measures of Correlation Feature 2

$$Information\ Measure\ of\ Correlation\ 2 = \sqrt{1 - e^{-2(HXY2 - HXY)}} \tag{24}$$

Where:

p_x - is the marginal row probabilities,

$$p_x(i) = \sum_{j=0}^{N_g-1} p(i,j) \tag{25}$$

p_y - is the marginal column probabilities,

$$p_y(i) = \sum_{i=0}^{N_g-1} p(i,j) \tag{26}$$

$$p_x(i) = p_y(j)$$

For symmetric a co-occurrence matrix. This will result in the following calculations

$$p_x(0) = p_y(0) = 0.21 + 0.03 + 0.03 + 0 + 0 = 0.27 \tag{27}$$

$$p_x(1) = p_y(1) = 0.03 + 0 + 0.05 + 0 + 0.05 = 0.13$$

$$p_x(2) = p_y(2) = 0.05 + 0.05 + 0.26 + 0 + 0.05 = 0.41$$

$$p_x(3) = p_y(3) = 0 + 0 + 0 + 0.05 + 0.03 = 0.08$$

$$p_x(4) = p_y(4) = 0 + 0.05 + 0.05 + 0.03 + 0 = 0.13$$

H - is the entropy of $p(i,j)$,

$$H = -\sum_{i=0}^{N_g-1}\sum_{j=0}^{N_g-1} p(i,j)\, log_2\big(p(i,j)\big) \tag{28}$$

HX - is the entropy of p_x,

$$HX = -\sum_{i=0}^{N_g-1} p_x(i)\, log_2(p_x(i)) \tag{29}$$

HY - is the entropy of p_y,

$$HY = -\sum_{i=0}^{N_g-1} p_y(i)\, log_2\big(p_y(i)\big) \tag{30}$$

For a symmetric matrix HX = HY

$$HX = HY = 0.27 \times log0.27 + 0.13 \times log0.13 + 0.41 \times log0.41 + 0.08 \times log0.08 + 0.13 \times log0.13 = 0.35 \tag{31}$$

$$\therefore HX = -1.44$$

HXY is the entropy which is -3.41

HXY1

$$HXY1 = -\sum_{i=0}^{N_g-1}\sum_{j=0}^{N_g-1} p(i,j) \log\Big(p_x(i)p_y(j)\Big)$$

$$HXY1 = -(0.21 \times \log(0.27 \times 0.27) + 0.03 \times log(0.27 \times 0.13) + 0.03 \times log(0.27 \times 0.41) + 0 \times log(0.27 \times 0.08) + 0 \times log(0.27 \times 0.13) + 0.03 \times log(0.13 \times 0.27) + 0 \times log(0.13 \times 0.13) + 0.05 \times log(0.13 \times 0.41) + 0 \times log(0.13 \times 0.08) + 0.05 \times log(0.13 \times 0.13) + 0.05 \times log(0.41 \times 0.27) + 0.05 \times log(0.41 \times 0.13) + 0.26 \times log(0.41 \times 0.41) + 0 \times log(0.41 \times 0.08) + 0.05 \times log(0.41 \times 0.13) + 0 \times log(0.08 \times \tag{32}$$

$0.27) + 0 \times log(0.08 \times 0.13) + 0 \times log(0.08 \times 0.41) + 0.05 \times log(0.08 \times 0.08) + 0.03 \times log(0.08 \times 0.13) + 0 \times log(0.13 \times 0.27) + 0.05 \times log(0.13 \times 0.13) + 0.05 \times log(0.13 \times 0.41) + 0.03 \times log(0.13 \times 0.08) + 0 \times log(0.13 \times 0.13))$

$$\therefore HXY1 = -2.89$$

HXY2

$$HXY2 = -\sum_{i=0}^{N_g-1}\sum_{j=0}^{N_g-1} p_x(i)p_y(j)log(p_x(i)p_y(j))$$

$$HXY2 = -((0.27 \times 0.27) \times \log(0.27 \times 0.27) + (0.27 \times 0.13) \times log(0.27 \times 0.13) + (0.27 \times 0.41) \times log(0.27 \times 0.41) + (0.27 \times 0.08) \times log(0.27 \times 0.08) + (0.27 \times 0.13) \times log(0.27 \times 0.13) + (0.13 \times 0.27) \times log(0.13 \times 0.27) + (0.13 \times 0.13) \times log(0.13 \times 0.13) + (0.13 \times 0.41) \times log(0.13 \times 0.41) + (0.13 \times 0.08) \times log(0.13 \times 0.08) + (0.13 \times 0.13) \times log(0.13 \times 0.13) + (0.41 \times 0.27) \times log(0.41 \times 0.27) + (0.41 \times 0.13) \times log(0.41 \times 0.13) + (0.41 \times 0.41) \times log(0.41 \times 0.41) + (0.41 \times 0.08) \times log(0.41 \times 0.08) + (0.41 \times 0.13) \times log(0.41 \times 0.13) + (0.08 \times 0.27) \times log(0.08 \times 0.27) + (0.08 \times 0.13) \times log(0.08 \times 0.13) + (0.08 \times 0.41) \times log(0.08 \times 0.41) + (0.08 \times 0.08) \times log(0.08 \times 0.08) + (0.08 \times 0.13) \times log(0.08 \times 0.13) + (0.13 \times 0.27) \times log(0.13 \times 0.27) + (0.13 \times 0.13) \times log(0.13 \times 0.13) + (0.13 \times 0.41) \times log(0.13 \times 0.41) + (0.13 \times 0.08) \times log(0.13 \times 0.08) + (0.13 \times 0.13) \times log(0.13 \times 0.13)) \quad (33)$$

$$\therefore HXY2 = -2.88$$

Information Measures of Correlation Feature 1

$$Information\ Measures\ of\ Correlation1 = \frac{-3.41 - (-2.89)}{\max(-1.44, -1.44)} \quad (34)$$

$$\therefore Information\ Measures\ of\ Correlation1 = 0.36$$

Information Measures of Correlation Feature 2

$$Information\ Measures\ of\ Correlation2 = \sqrt{1 - e^{-2(-2.88-(-3.41))}}$$

$$Information\ Measures\ of\ Correlation2 = 0.81 \tag{35}$$

It is possible that HXY > HXY2, which would result in returning complex numbers. In these cases, a value of 0 is returned for IMC2. This affects some of the values in *Table 7* to *Table 12*.

The Haralick texture features calculations that have been presented in this section are examples of the method employed in some part of this study to investigate the influence CT technique parameters. In the illustrations, a 5x5 co-occurrence matrix obtained from 5x5 matrix of image intensities obtained from an image ROI of 5x5 pixel matrix. The size of the matrix and space within this document was considered when crafting the demonstration of the algorithms. The images used in the following part of the study where from the CCR phantom. This part of the study strictly uses phantom images that were acquired at CT machines using standard acquisition protocols described in Chapter 3 of this document. To control the experiment, the images were not pre-processed or had filter applied to them for either smoothing of any other purpose.

2.1.4 Software Description

To segment and extract radiomics texture features 3D Slicer software was used in part of this study. 3D Slicer is a Harvard Medical School developed free and open source software package for image analysis and scientific visualization (Jennings et al., 2012; Pieper et al., 2006). The use of 3D slicer for clinical investigations includes tumour segmentations and radiomics quantitative feature enumerations. 3D-Slicer is available and easily accessible by download for free and 3D slicer has been widely employed in non-small cell lung (NSCLC) tumour image quantitative studies and has proven to be robust. Velazquez et al. (Velazquez et al., 2013) have concluded in their study on NSCLC that the 3D Slicer algorithm tumour segmentations were comparable and had a low variability to those manually delineated by physicians.

MATLAB® 2017a software package was also used to segment and extract pixel intensities. This was performed on specific insert (cartilage) central slice image. The pixel intensities extracted were used in hand calculation stage of this study.

Chapter 3: Materials and Methods

3.1 Materials and Methods

3.1.1 Introduction to the material and methods

This chapter 3 builds up on the previous chapter which explored the mathematical layout of some of the algorithms that are used in the software used to calculate radiomic texture features. The previous chapter as much as it reviews literature, it executed the hand (manual) calculations of a selected radiomics texture features. This chapter 3 develops the experimental techniques that were used to fulfil the objectives of the study. The Credence Cartridge Radiomics phantom (CCR) was imaged at two manufacturer CT scanners (2 Toshiba Aquillion Long bore CT and 2 GE Lightspeed units). Two programming softwares (3D Slicer and Matlab 2017a package) were used to process the CCR phantom images. The Matlab 2017a software package was used to segment and therefore extract image data to get image matrices at variable CT technique parameters. The Matlab extracted image matrices were used to perform radiomic texture feature calculations. The hand GLCM texture features enumeration was done with assistance of Microsoft excel spreadsheets.

The 3D Slicer software with plugins of PyRadiomics was also used to segment the CCR phantom images. Radiomic texture features were extracted from the region of interests (ROIs) on the PyRadiomics platform. For each insert segmented phantom insert 16 set of a list of radiomic texture features were extracted to Microsoft excel spreadsheet for analysis and presentation. This investigated the use of invariant tool to practically identify robust features and compare features from the different CT scanners used in this study.

To explore the use of the identified robust texture features on a patient data set. A section was designated for the patient cohort (cervical cancer patient group). The weekly obtained Cone beam Computed Tomography patient images was also segmented on the 3D Slicer PyRadiomics platform to extract the radiomic features for further analysis.

3.1.2 Phantom Study

Different CT machines available at the Universitas Academic Hospital complex (UAH) were used for data collection. The authority to access and use the UAH equipment was formally sought from the hospital management. The CCR phantom shown in Fig 10 below was supplied by the M D Anderson ~~Cancer~~ Centre, University of Texas.

The CCR phantom consisted of 10 different cartridges, each of the size 10.1 x 10.1 x 3.2 cm^3. The properties of the cartridges resembled various human tissue textures. The phantom cartridges were made of the following materials; Cartridge 1 composed of plaster resin, the second was made of natural cork, acrylic made the third cartridge, high density cork for the fourth cartridge, glued and pressured rubber particles made up the fifth cartridge, sycamore wood was used to make the sixth cartridge and the seventh up to the tenth cartridges were

composed of acrylonitrile butadiene styrene plastic with honeycomb holes that made the filling levels to be between 50% and 20% with a 10% decrement from cartridge 7 to 10 (Yasaka et al., 2017; Mackin et al., 2015).

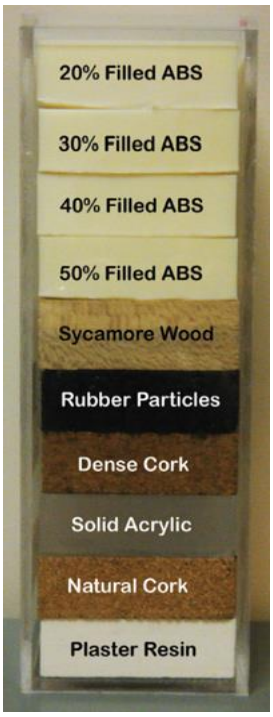

Fig 10. The credence cartridge radiomics (CCR) phantom(Mackin et al., 2017)

3.1.2.1 Acquisition

In general, the use of medical images in the detection of tumours during any stage of cancer treatment or the diagnosis stage depends on the trained clinical professional's ability to perceive the contrast and other image properties with accuracy. The above is true if all the images used are clinically acceptable fit for the purpose, thus a quality control (QC) program that ensures good picture quality must be in place for the machines used for patient imaging. In this study, the image quality QC was performed before the CCR phantom was imaged on each of the machines used.

To determine the intra-and inter-scanner variability of the radiomic texture features, the CCR phantom was acquired using the CT machines – 2 General Electric (GE) and 2 Toshiba large bore.

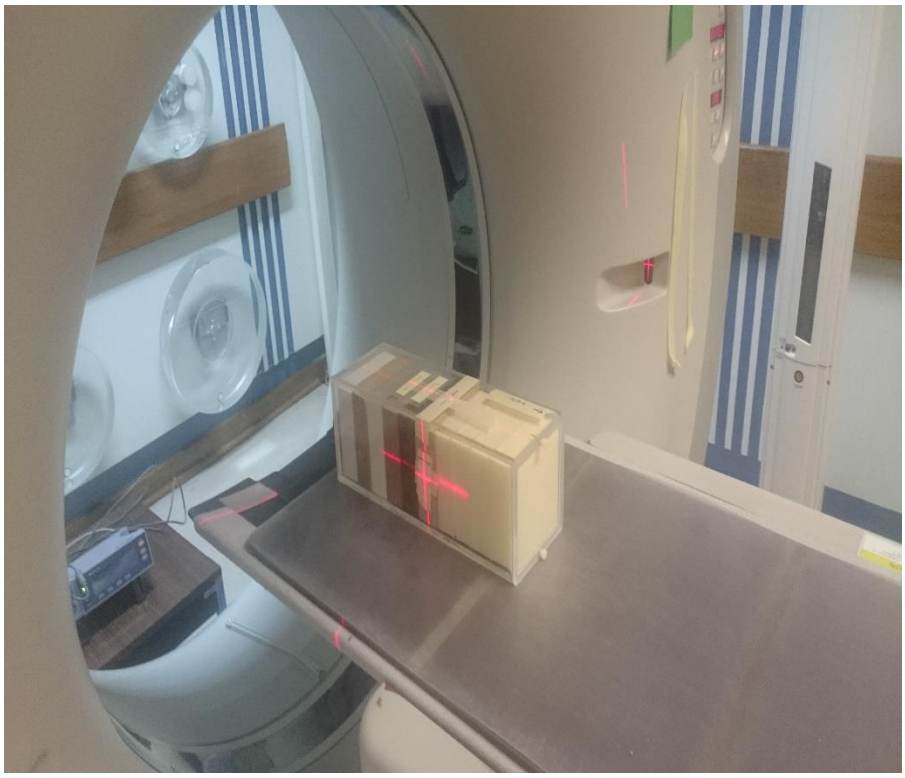

Fig 11. Phantom Study scan set-up

The set-up in Fig 11 was used to scan the CCR phantom on all the CT scanners. The CCR phantom has a marker that was used to align the phantom at the laser crosshairs of the CT scanners, used for patient or phantom alignment before scanning. Three CT technique parameters (mAs, slice thickness and kVp) were investigated in the phantom study. A reconstruction interval of 1 was used during the phantom imaging hence an adjacent interval or zero inter-slice gaps was used for all scans. To investigate the effects of changing the mAs on the radiomic features, a single fixed slice thickness (5mm) and 120kVp were selected, then the mAs was varied from a 75 mAs to 400 mAs. The kVp was changed from 80 kV to 135kVp with the slice thickness and mAs fixed at 5 mm and 300 mAs respectively. This was to investigate the effects of kVp variation. During the mAs and kVp variation acquisitions, the pixel size sampling was set fixed by making the field of view (FOV) at which the images of the phantom were acquired constantly. A FOV of 160.9 mm was used and this corresponded with a pixel size ranging 0.31 mm. The pixel size was calculated as FOV/matrix size and a matrix size of 512 by 512 was kept constant for all scans also. This meant that the voxel size was a fixed parameter for the mAs and kVp investigations. Only the slice thickness study had the voxel size changing as slice thickness vary. Therefore, there was a total of 90 phantom sets for the mAs, kVp and slice thickness study for each unit. To facilitate inter-scanner comparison, close similar acquisition and reconstruction parameters were used across different scanners as shown in *Table 1* and *Table 2*.

Table 1: Imaging protocol of the CCR phantom at the Toshiba Aquillion/LB CT scans

Scanning parameters	CT Unit
Tube voltage	80, 100, 120 and 135 kVp
Tube current	75, 100, 150, 200, 250, 350 & 400 mAs
Field of View	160.9 mm
Slice thickness	1.0, 2.0, 3.0 and 4 mm
Reconstruction algorithm	Standard, Thorax, abdomen and head
Pitch	1
Matrix size	512

Table 2: Imaging protocol of the CCR phantom at the GE Lightspeed scans

Scanning parameters	CT Unit
Tube voltage	80, 100, 120 and 140 kVp
Tube current	20, 50 to 350 mAs in steps of 25mAs
Field of View	160.9 mm
Slice thickness	0.625, 1.25, 2.5, 3.75 and 5 mm
Reconstruction algorithm	Standard, Thorax, abdomen and head
Pitch	1
Matrix size	512

3.1.3 Contouring and Feature Extraction

For importing, exporting and contouring purposes, a sophisticated open-source software platform for biomedical research called 3D Slicer was used (Yip et al., 2017; Velazquez et al., 2013; Jennings et al., 2012). MATLAB® 2017a software package was also used to segment and extract pixel intensities. This was performed on specific insert (cartilage) central slice image.

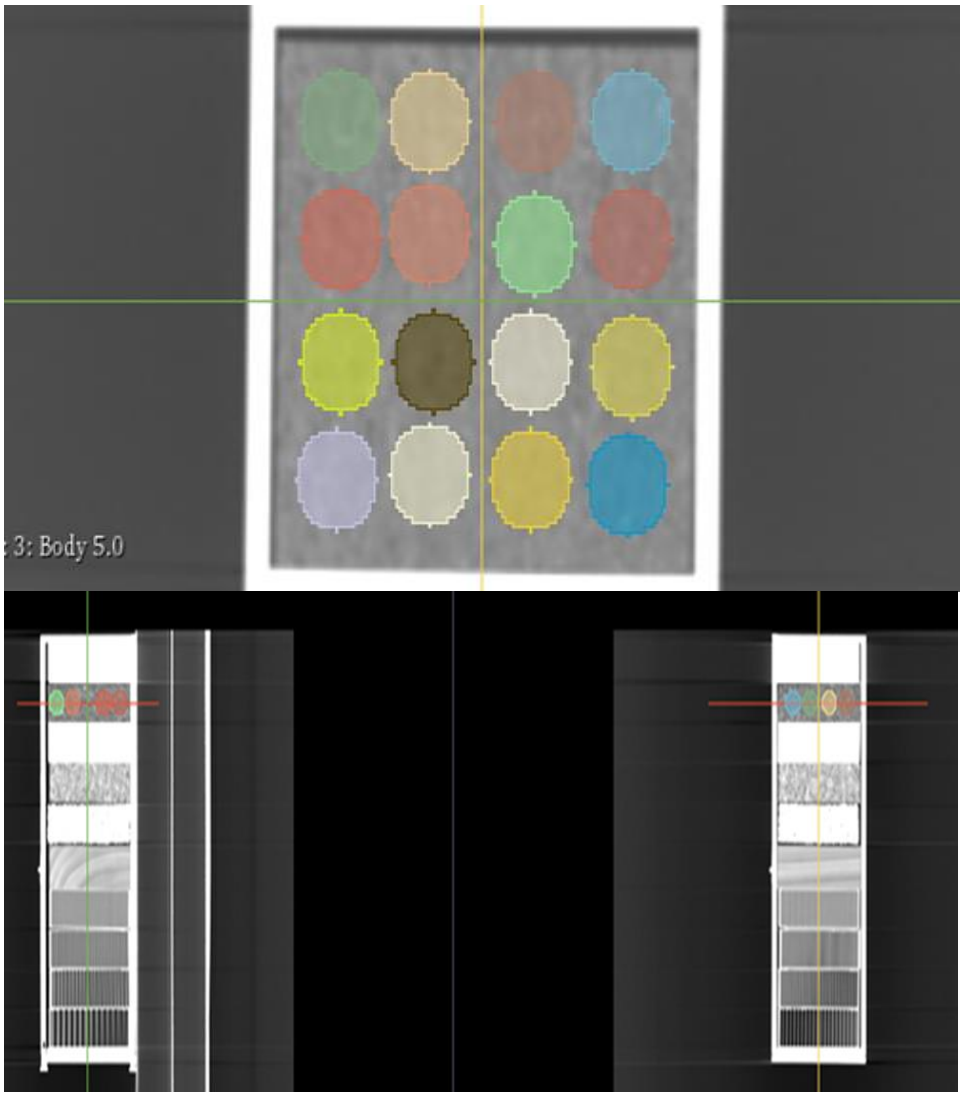

Fig 12. 3d slicer CCR phantom ROI contours delineation set-up

As illustrated in Fig 12, spheres of a 20 mm diameter each were used to draw ROIs on the CCR phantom images. Initially, a Cartesian plan was inserted on the axial phantom insert image that was going to be segmented. Then four spherical ROIs were contoured on the four regions of the Cartesian plan giving a total of 16 spherical ROIs drawn per CCR insert. The spherical ROIs were kept identical (2 cm diameter) in size for all images used. Radiomic features were extracted and calculated using the radiomics extension of 3D Slicer (PyRadiomics) (Balvay et al., 2019; Griethuysen et al., 2017; Jennings et al., 2012).

A single square segment that covered 90% of the CCR phantom insert as displayed in Fig 13 was used to extract image matrices on Matlab 2017a package. A 512x512 image matrix was extracted to Microsoft excel spreadsheet per image. Using the 512x512 image matrix, four small 10x10 matrices were further extracted around the origin

of the bigger matrix. The 10x10 image matrices were used to perform radiomics hand calculations using the mathematical equation examples in chapter 2. The sizes of the co-occurrence matrices obtained from these 10x10 image matrix relied on the range of the pixel intensities within the ROI. The significance of the features values was evaluated by employing the co-efficient of variance (COV %) (Kim et al., 2016; Yan et al., 2015). Features that produced a COV % that was systematically small (less than 10%) through the test-retest method were considered robust (Molina et al., 2016; Reed et al., 2002). Consistently small dispersions of the feature values around the mean of that feature obtained as a result of CT image acquisition parameter systematic change determines the robustness of the feature. The 10x10 image matrices were also used to analyse the relationship between image noise and CT imaging technique parameters.

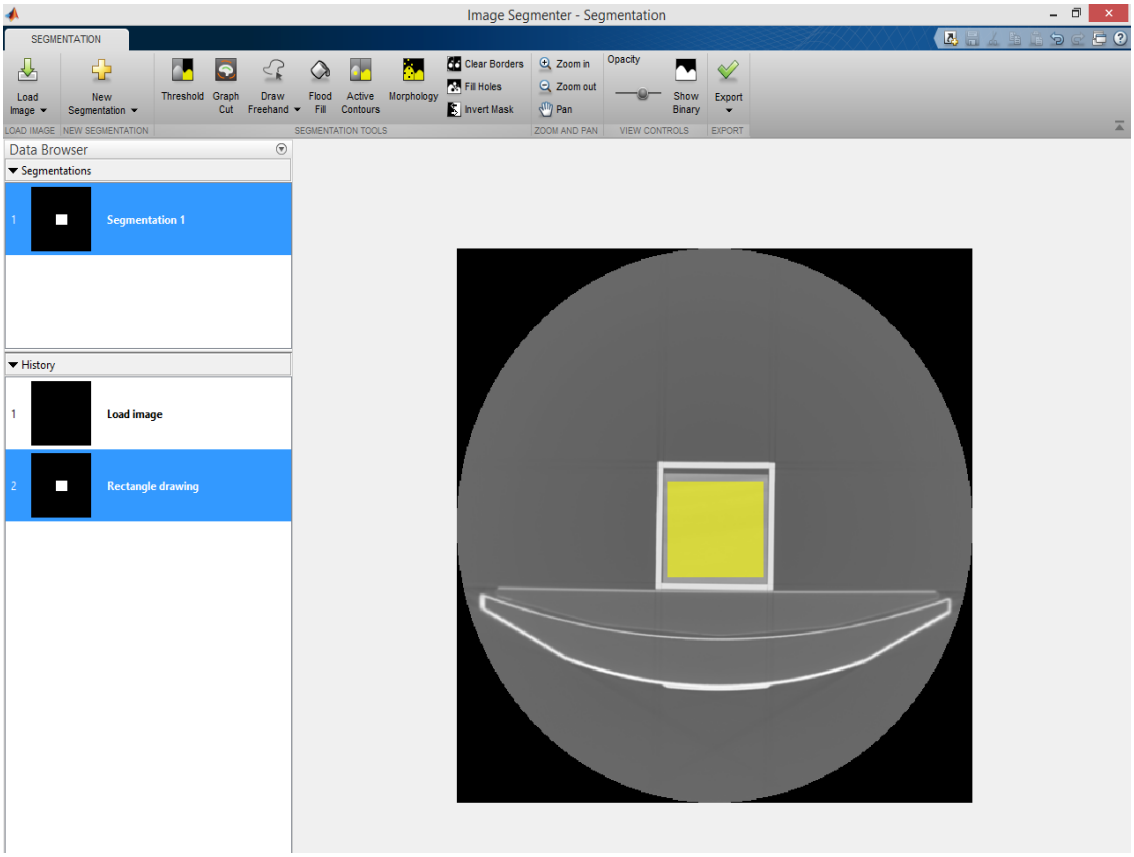

Fig 13. Matlab 2017a package CCR phantom segmentation

3.1.4 Impact of the volume region of interest (ROI) on radiomic texture features

Two schools of thought existed about which ROI to use for the patient data sample investigation. The first idea was to use the PTV ROI already existing on the patient image data set and the second idea was to use a fixed ROI to be inserted inside the PTV. There was therefore a need to evaluate the impact of the ROI volume

on the radiomics texture features. The outcome of this evaluation was to be employed in the whole study by choosing the appropriate volume of ROI to extract radiomic texture feature data from images.

The cervical cancer treatment patient data used in this study had the uterus delineated by experts (Dosimetry Medical Physicist and Radiographers) to represent the PTV for radiotherapy treatment purposes. This was because, at the Universitas Academic Hospital oncology department in Bloemfontein, cervix cancer patients were mainly treated through radical 3D conformal planning which conforms the radiation beams to the whole uterus. Also, the images used were acquired through the Cone Beam Computed Tomography (CBCT) imaging modality which did not offer better visibility of tissue differences. The CBCT images did not clearly reveal the tumour but the uterus and bladder was clearly seen and easily delineated.

Initially the study intended to use the uterus delineated on the Monaco planning simulation software, as the base ROI from which the radiomic features would be extracted from on 3D slicer. This meant all the shape parameters used to calculate the shape features and all the other features that made use of those shape parameters would depend on the shape and size of the uterus. Other radiotherapy studies have shown that the uterus shape and size can vary between treatment fractions due to changes in bladder fillings (Hoogeman et al., 2017; Ye et al., 2017; Virendra et al., 2015). The changes of the uterus positions were attributed to the bladder location and anatomy. The bladder is located directly in front of the uterus. The bladder anatomy allows it to expand and contract depending on the amount of fluid it will be holding at a particular point in time. The changes in the bladder volume would greatly influence the shape and size of the uterus, in that if full the bladder pushes against the uterus leading to uterus changing size or shape. This meant the shape of the ROI could change when either the bladder is full, half-full, one-quarter full or empty.

Hence the second suggestion was to use a fixed volume ROI drawn inside the uterus using 3D Slicer software to extract the texture features. This would overcome the dependence of the radiomic texture features on volume or number of voxels in the ROI. Using a fixed volume would promote biological factors to be the only factors that influence radiomic texture features changes as the treatment progresses rather than some physical factors.

A study was conducted to investigate the assumption that the size of the sampling ROI could cause changes in the values of the robust radiomic feature values. This would also justify the use of fixed size ROIs segments within the base ROI (Uterus) to extract radiomic texture features.

The rubber insert image samples from the CCR phantom was used. Using the 3D slicer software, six sphere ROIs of varying diameters were drawn. The diameters of the ROI were 2 cm, 1.5 cm, 1 cm, 0.5 cm, 0.3 cm and 0.1 cm respectively. The radiomic texture features were then enumerated using PyRadiomics extension of the 3D slicer. Fig 14 show ROIs of varying volume that were used to evaluate the effect of volume ROI on radiomic

texture. A sample of texture features extracted was then plotted against the diameters of the spheres ROI as shown in Fig 36 and Fig 37 in the results section.

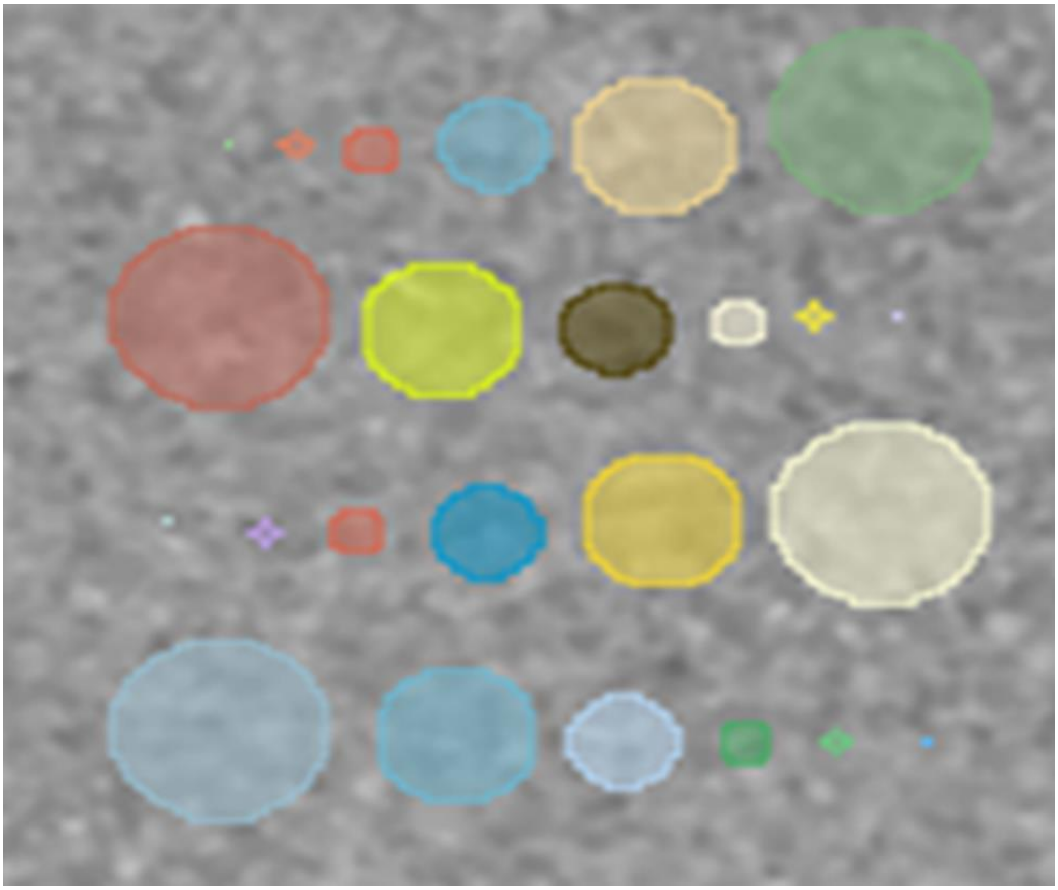

Fig 14. Representation of the phantom image with ROI drawn to evaluate the effect of ROI volume on radiomic texture features.

3.1.5 Normalising the radiomic texture features data

Two approaches were considered and employed when normalising the radiomics calculated texture features values. The first approach involved equation 36 below

$$f_n = \frac{\left(\frac{f_p - f_b}{f_b}\right)}{\left(\frac{\sigma_t}{\mu_t}\right)} \tag{36}$$

Where f_n is the patient normalised feature definition, f_p is the calculated feature value at a specific imaging parameter (e.g. this can be a feature value at 50 mAs, 100mAs or any other value used during acquisition), f_b is

the feature value at a given baseline (e.g. 5mm for slice thickness analysis, 300mAs for tube current analysis and or 140 kV for tube potential difference investigations), σ_t is the standard deviation of the tumour texture feature values and μ_t is the tumour feature mean value. Using equation 36 the texture feature variations caused by changing a given imaging technique parameter (kV, mAs and/or slice thickness) that were being investigated in this study could be assessed in relation to the tumour differences (inter patient variation). If calculated based on the σ_t and μ_t of a patient's treatment fraction, the dependence of the imaging parameter changes due to the stage of treatment were assessed.

The second approach was using the z-score standardisation/ normalisation process. Equation 37 was used to perform the feature calculation normalisation;

$$f_z = \frac{f_p - \mu_p}{\sigma_p} \tag{37}$$

Where f_z is the –z-score normalised feature value definition, f_p is the calculated feature value at a specific imaging parameter (e.g. this can be a feature value at 50 mAs, 100 mAs or any other value used during acquisition), μ_p is the mean value of the calculated feature at the specific parameter being investigated, σ_p is the standard deviation value of the calculated feature at the specific parameter being investigated.

3.1.6 Patient group

The data that was used to monitor the robust radiomic texture features was from patients who underwent cervical cancer radiotherapy radical treatment with concurrent chemotherapy at the Universitas Academic Hospital Annex from 2016 to 2017. The patients were treated using 3D conformal external beam radiation therapy. The patient group were all stage three cancer patients, but the extent of the stage was not the same. This group of patients did not have the same type of cancer, some had Squamous cell carcinomas, and at least 1 had Adenocarcinoma, see *Table 3* below. The data was used for another study in at Universitas Academic Hospital that had an Ethics number 28/2014A. This meant the data samples was acquired prior to this study hence the study was retrospective. Ethical approval was obtained from the University of the Free State and Department of Health research committees to use the patient images for this study. The analyses were performed using the kV Cone Beam CT (kV CBCT) images and CT images, clinical factors, and outcomes data from a set of 6 patients treated. The inclusion criteria for patients in this study were the presence of a pathologically proven, the tumour not surgically removed, locoregional metastasis and the use of the bladder protocol during the imaging sessions of 25 treatment fractions. The exclusion criteria for this investigation; the patients must not have a positive pregnancy screening, the imaging bladder protocol was not strictly followed

for the imaging stage of the patient (pre-treatment), body weight that exceeded the limits of the treatment couch and the images not visible enough for the uterus to be segmented.

The goal of this part of the study was to determine the variations on the radiomic features pre-treatment and at the end of treatment. This was to determine the biological differences in the tumour region along the treatment time thus could be used as a measure of the clinical relative biological effectiveness (RBE). Though factors such as the type of tumour cells, beam energy, depth of a tumour from the surface, dose per fraction and the linear energy transfer (LET) determine the RBE. In this patient study group the treatment administered was a 2Gy per fraction photon dose for 25 fractions with a brachytherapy boost of more than 2Gy to the prescription point. CBCT images acquired on the first day of treatment was used and the subsequent start of every week CBCT and the last fraction.

Table 3: Shows a sample of cervical cancer patient data

Patient	Stage	Age	Endo /Exo	Parametrial Invasion	Vaginal Involvement	Adeno/ Squam	Pre-treatment Tumour size	Chemo Cycles	Chemo (mg)	Previous Chemo Cisplatin
A	IIIB	48		Bi-lateral	Sup 2/3	*Squam	34x50 mm	6	39 mg	
B	IIIB	44	+Endo	Left		*Squam	50x45 mm	5	39 mg	4 cycles
C	IIIB1	67	-Exo	Bi-lateral	1/2	¬Adeno	76x44 mm	6	48 mg	
D	IIIB	60	-Exo	Bi-lateral		*Squam	81x75 mm	6	48 mg	3 cycles
E	IIIB1	62		Right	Sup 2/3	*Squam		6	46 mg	
F	IIIB1	53	-Exo	Left		*Squam	50x48 mm	6	43 mg	1 cycle

*Squam is Squamous cell carcinomas, ¬Adeno is Adenocarcinomas, +Endo is Endocervix, -Exo is Exocervix

3.1.7 Imaging Parameters

The patients were imaged weekly during their treatment with the institutional bladder protocol on the Toshiba Aquilion/ LB (large bore) and on the Elekta kV CBCT for the pre-treatment set-up at National Hospital-Annex in Bloemfontein. Before CT imaging, all patients who were involved in the study were given clear instructions specifying their fluid intake. Patients were required to drink about 500-700 cm^3 of water at least 1 hour before the scans and another 500 cm^3 30 minutes before the scan. The CT was first performed with a full bladder. Then, in the same position, another set of CT images were acquired after the patients were asked to empty their bladders. The patient images were acquired using the pelvic imaging protocol. The peak tube voltage of 120

kV, tube current of 32 mA, and exposure time of 40 seconds on the Elekta kV CBCT. At the Toshiba machine a peak tube voltage of 135 kV, tube current of 300 mA, and the rotation time of 0.75 seconds were used to acquire the pelvic images. The acquired images were reconstructed into a 512x512 pixel matrix with an image thickness of 3 mm and an in-plane resolution of 1.6 pixels per mm thus a pixel size of 0.625x0.625 mm^2.

The patient study focused on the kV CBCT produced images because it was the modality that was used to scan the patients frequently at the Linac before treatment was delivered. kV CBCT images were routinely acquired for patient setup verification at the Linac and at least once a week a set of images was being obtained. The weekly kV CBCT image data set was used in this study. There are drawbacks in using kV CBCT images for studies that require an enormous amount of detail from the images. The drawbacks include relatively poor image quality than regular CT. This is attributed to the increased amount of scatter from the wider distance between the x-ray source and the detectors panel of the kV CBCT. Also different detector types are used in CT and kV CBCT. kV CBCT uses a flat-panel detector. The flat panel detector that is used in kV CBCT has very low spatial resolution abilities as compared to the diode detectors used in conventional CTs thus contributing to poor image quality being produced by the kV CBCT. The kV CBCT mechanical set-up around the Linac's iso-centre produces challenges in improving the kV CBCT image qualities in that the distance between the x-ray source and the detector is big as compared to a conventional CT. The large distance between the x-ray source of the kV CBCT and the detector will in-turn promote more X-rays scattering that will reach the detector during imaging. The kV CBCT imaging scan time of close to 1 minute is longer than conventional CT images (7-14 seconds) and patients are prone to perform slight movements during the scan, which can introduce subtle motion artefacts in kV CBCT images. The pelvis images were reconstructed to a 512x512 matrix grid for a 5 mm slice thickness used at the Elekta Synergy Linear Accelerator kV CBCT. The peak kilo-voltage used for the kV CBCT acquisition was 120kVp, 32 mA and an exposure time of 40 seconds.

3.1.8 Feature extraction region of interest

The use of CT images alone to delineate the target volumes in radiotherapy patient treatment presents limitations in differentiating soft tissues and the tumour. This is attributed to the tissue attenuation coefficients that are relatively the same in value. Usually, other imaging modalities (MRI, PET) images that give a better soft tissue contrast differentiation are fused with CT images of the same target region to draw the region of interest (ROI). The above allows the delineation of the gross palpable volume (a tumour) and the corresponding clinical and planning treatment volumes. Ideally, radiomics studies consider only the tumour ROI for analysis.

As can be observed from Fig 15 below, there was no clear tumour observable on the CBCT images for cervical cancers except on exceptional cases were big and coarse calcifications existed. In practice, kV CBCT images are mainly used for patient set-up at the Linac before external beam radiotherapy. Specific land markers like

bones or fiducial markers inside an organ which can be clearly visible on CBCT images, usually assist for the purpose of Linac pre-treatment set-up.

The clinical treatment volume (uterus) was manually contoured and was used as the base region of interest (ROI) for feature extraction. The base ROI drawing was performed on the Monaco simulation software workstation used for patient images pre-treatment planning. The 3D slicer software was then used to delineate 5 ROIs that are 2 cm diameter spheres inside the uterus. The 5 ROIs within the uterus were of a better statistical significance but the drawback on this was the fact that the kV CBCT images could not provide a clear visible tumour. The radiomic texture features were then calculated and extracted using the 3D Slicer software. To ensure that meaningful observations could be drawn from the results extracted, a ROI that produced values that were extreme outliers as compared to other 4 ROIs were excluded from the further data processing. The interquartile range method was identify and remove outlier feature values before averages used in plotting graphs were calculated. In this interquartile range method outliers were identified to any value below the 25th percentile and any value above the 75th percentile of the sample. This means the results presented on the patient data section involved either 5 ROIs or 4 ROIs for each uterus information processed.

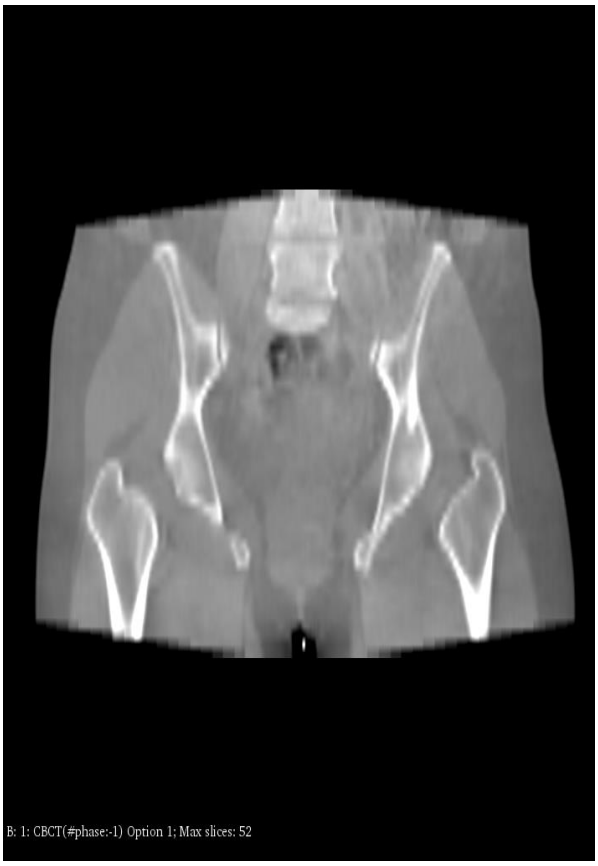

a)

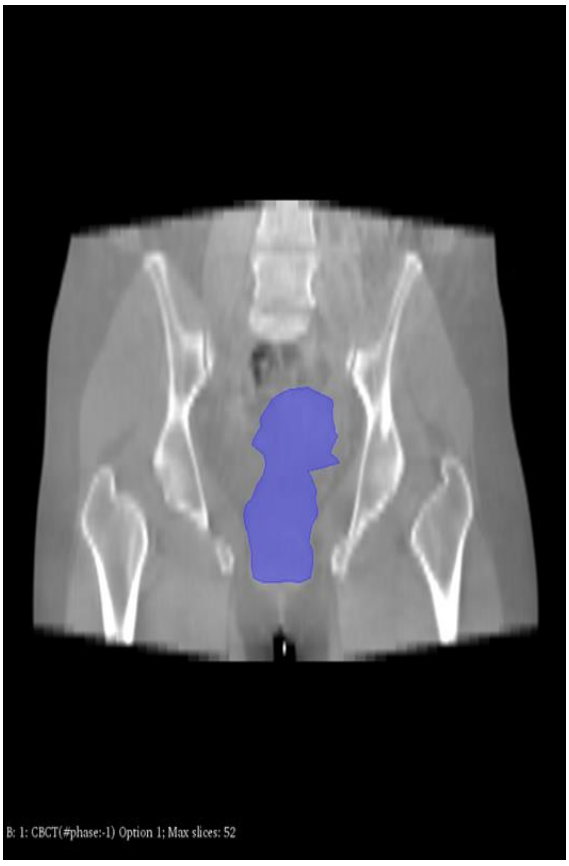

b)

Fig 15. Representation of the patient images uterus segmentation for feature extraction in a 3D view. The first image a) of Fig 15 show the anatomy sample of the image data sample before the clinical treatment volume was drawn as shown in b).

Fig 16 below shows the example of 2 cm diameter spheres contouring inside the uterus ROI. Images that had no visible uterus were excluded from the study.

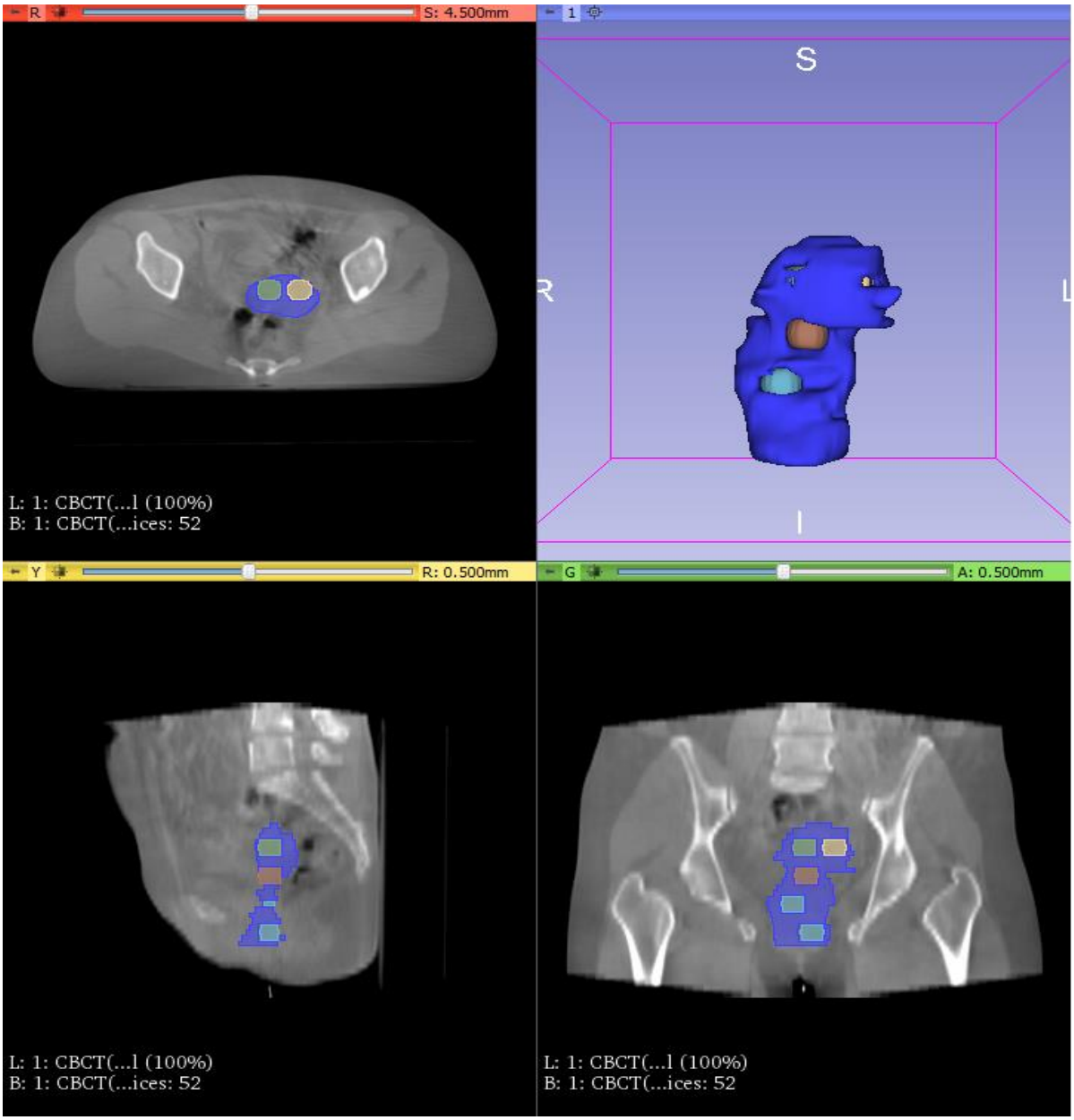

Fig 16. Representation of the patient images with the 5 ROIs contoured inside the uterus segment for feature extraction in a 3D view PyRadiomics

A similar approach as outlined in Fig 16 is shown in Fig 17. Fig 17 represents the delineation of 2 cm diameter spheres inside the bladder ROI. The bladder 2 cm diameter sphere ROIs were employed in extracting the radiomic texture features that were used to normalise the tumour 2 cm diameter spheres extracted texture features. In this study, the coefficient of variation of the bladder texture features values for each treatment fraction was used to normalise the tumour texture features of that fraction as shown in equation 36. This method of normalisation assumes that the bladder is filled with a fluid solution which makes it a homogeneous volume, hence the variation of tumour texture features during the irradiation treatment course can be determined without data integrity loss.

To exclude the effect of various pre-processing techniques on the texture features, no pre-processing was performed on the image data sets used in this study. The ROI volume was fixed at 2 cm diameter sphere segmented within the uterus and the bladder of the patient data set. The minimum number of voxels in the patient data sample ROI is 789. This satisfied the minimum number of voxels required to adequately derive intensity variations that did not result from a change in the volume of the ROI. This was supported by a publication by Brooks F.J. and Grigsby P.W. (Brooks and Grigsby, 2014) which observed that smaller tumour volumes did not contain enough intensity data for heterogeneity quantifiers. This meant small ROI volumes could cause a significate loss of data integrity because they did not meet the minimum volume (700 voxels) assumed to prevent degradation of information by under-sampling in the ROI. Therefore, spheres of 2 cm diameter that sampled at least 789 voxels were used throughout this study to delineate the ROI for feature extraction purposes.

The size of the phantom cartridge was the other factor that prompted the 2cm diameter sphere choice. The cartridge was 10 cm long, 10 cm wide and 3 cm thick. The thickness of the cartridge limited the volume ROI to be less than 3 cm diameter or/ thick. Considering that the phantom cartridges were stacked one against another in the phantom, there existed greater chances of the influence of partial volume effect to regions that were close to edges of the cartridge. Therefore the centre of the sphere was placed at the centre of the cartridge image such that at least 0.5 cm from the edges of each cartridge being sampled was excluded. 5 spheres were placed inside the tumour or bladder ROI to ensure precision and accuracy of the radiomic texture features extracted.

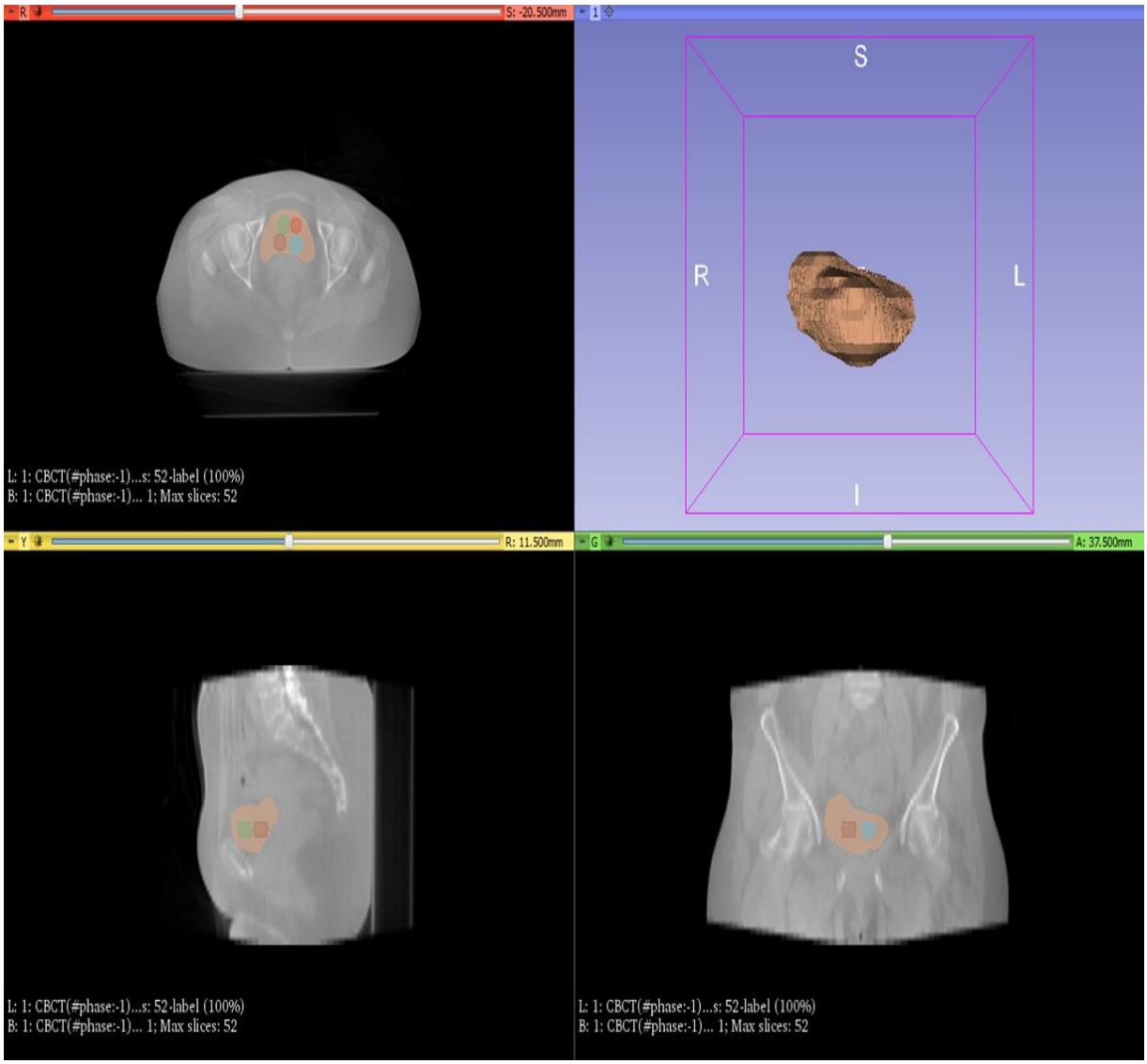

Fig 17. 2 cm diameter spheres segmentation inside the bladder ROI

3.1.9 Radiomics Feature Calculation Software

The 3D Slicer software package with the radiomics plug-ins extensions installed was used for the calculation of all radiomic features in this study. The software was an open-source called PyRadiomics (J. J. M. van Griethuysen et al., 2017). PyRadiomics was compatible with both python 2.7 and python 3 versions (3.4 and 3.5). The 3D Slicer platform provided a graphical user interface to the PyRadiomics library which allowed viewing and segmenting images. The segments performed on another software could be imported with the image structures for further processing on the 3D slicer platform to extract the radiomic features (using PyRadiomics) from specific segments.

3.1.10 Statistical software analysis

Microsoft Office Excel package and MATLAB 2017a package are the main software employed in this study to draw statistical and analytic observations and inferences.

The coefficient of variance (COV) was used to show the variability of the tumour radiomics feature values under the patient study. The COV was also used to show the robustness of the radiomic features used for the patient analysis study. The COVs were classified into the following four classes; very small ($COV \leq 5\%$), small ($5\% < COV \leq 10\%$), intermediate ($10\% < COV \leq 20\%$), and large ($COV > 20\%$) range of variation (Kim et al., 2016; Yan et al., 2015) . The COV was calculated by dividing the standard deviation (SD) by the average feature value and then multiplied by 100 to produce a percentage.

Chapter 4: Results Presentation

4.1 Results

4.1.1 Introduction to result section

This chapter 4 reports the outcomes of the impact of changing the CT imaging parameters on the radiomic features. The previous chapter outlined in detail the techniques involved in the experimental investigation of this study. The use of features that are not stable due to scan technique parameters in radiomics studies might compromise the outcomes of such studies. Therefore assessing radiomic texture features robustness against the CT scan technique parameters. The work was thus performed to improve the general radiomic frameworks (Zwanenburg et al., 2019).

The first task was to use a CT scanner to variably change the imaging parameters (changing one parameter at a time whilst keeping all the other parameters constant) to acquire the CCR phantom. The CCR phantom images were then processes on PyRadiomics Python software platform. Text features were extracted and therefore analysed and the results presented in this chapter. Some of the CCR phantom images were also processed on Matlab software to extract 8x8 ROI matrices from the image pixel intensities arrays. The 8x8 image matrices were then processed to ascertain image noise relationship to slice thickness, kV and mAs changes. The 8x8 image matrices were also used to perform hand GLCM radiomic texture features calculations as was demonstrated in chapter 2 with assistance of Microsoft excel spreadsheets and Matlab. The results for the CT image noise relationship to CT acquisition parameters and the GLCM radiomic texture features calculations were also presented in this chapter.

The second exercise was to use a variation of robust radiomics texture features on a clinical patient data set. Recalling that it was proposed on aim that radiomic texture features that are constant to the CT imaging parameters variations could be used on a clinical cohort to extract information about the radiation treatment.

4.1.2 Phantom results

The phantom analysis results were displayed in Fig 18 to Fig 35. Fig 18 below demonstrated the tube current-time product effects on the first order statistics metrics extracted from the 10 cartridges of the CCR phantom. The CCR phantom images were acquired on the GE and Toshiba scanners. It is important to know that the points plotted in Fig 18 to Fig 35 were average values of each texture feature normalised to the tumour values. Each plot point was calculated using equation 36. Thus each plot point was calculated from information extracted from 16 spheres of 2 cm diameter per insert was displayed in Fig 12. As a result of normalising the radiomic texture features using equation 36 the standard deviations of the un-normalised data of these features could not be used to plot the uncertainty of each point. Normalising the standard deviations of the points plotted in Fig 18 to Fig 35 would not yield a standard deviation therefore that data was meaningless for this study and could not be plotted as uncertainty bars.

Strong tube current dependence was noticeable on sycamore wood, dense cork and solid acrylic. All the other materials did not exhibit any variations when the tube current was varied. Sycamore wood, dense cork and solid acrylic materials had more uniform structures (no texture) hence the results express the change in image noise as the tube current was being varied. Below is the key for reading Fig 18,

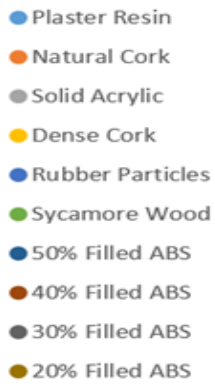

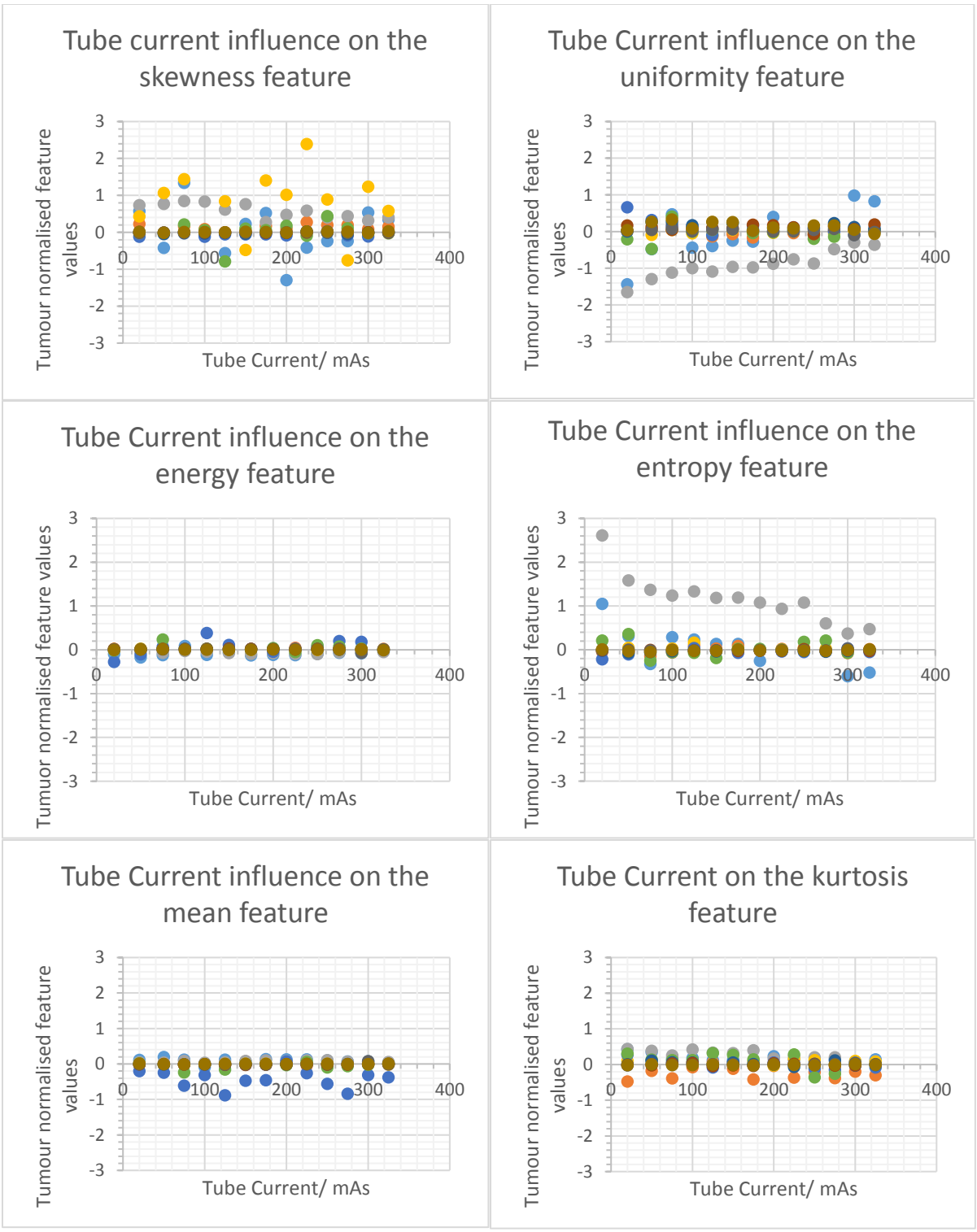

Fig 18. First order statistics patient normalised feature difference relationship with tube current variation for the 10 inserts of the CCR phantom images on the GE Brightspeed machine.

Fig 19 below consisted of 6 graphs that displayed the results of the relation between tube potential difference (kV) and first order statistics tumour normalised texture feature difference. Strong kV dependence was noticeable on rubber particles, dense cork and solid acrylic. All the other materials did not exhibit any variations as the kV was varied. Sycamore wood, dense cork and solid acrylic materials had more uniform structures (no texture) hence the results express the change in image noise as the kV was being varied.

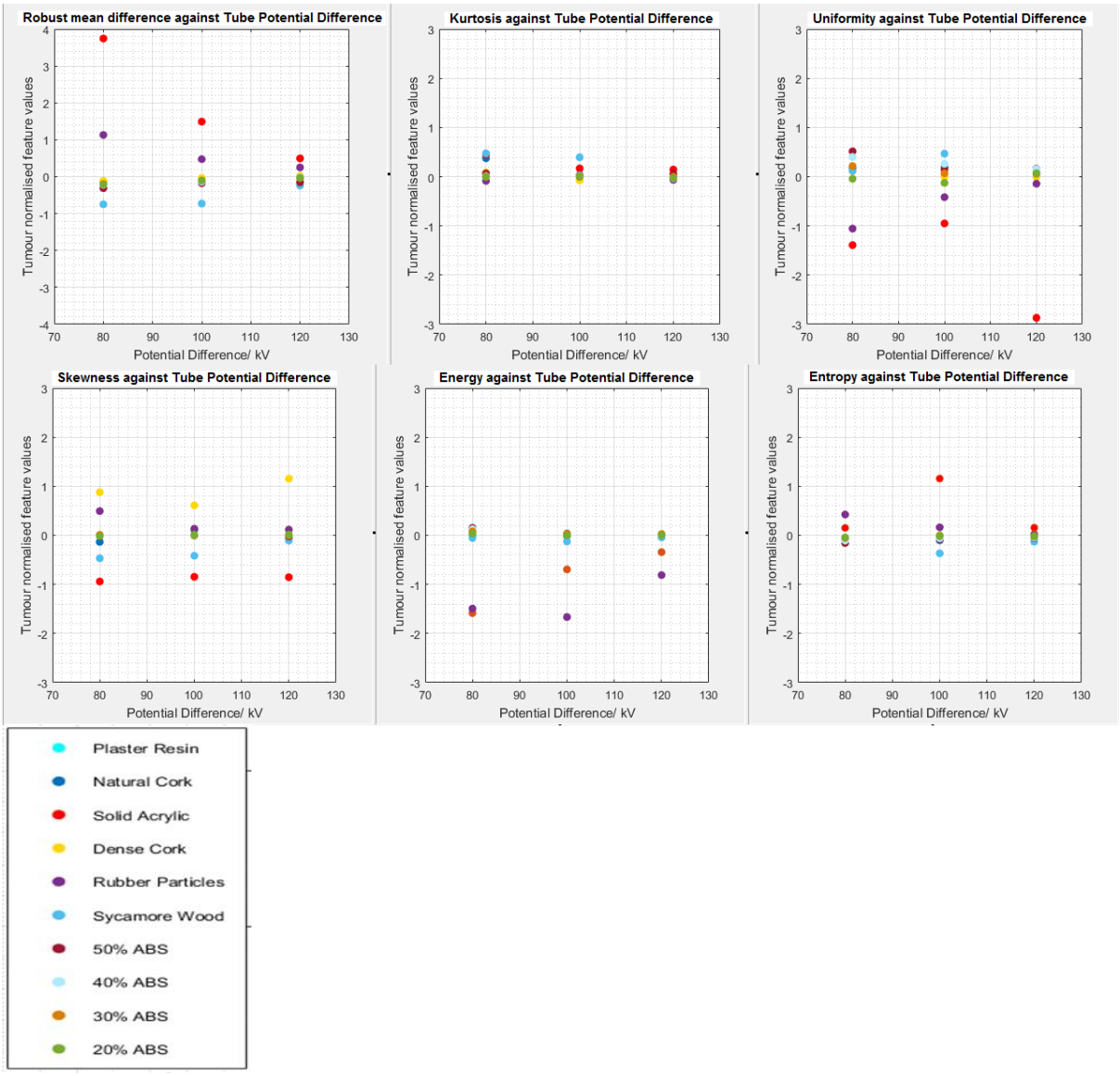

Fig 19. First-order statistics tumour normalised feature variability due to tube potential difference variation for the 10 inserts of the CCR phantom imaged on the GE Brightspeed machine.

Below is Fig 20 that shows the relationship between first order statistics features and the change in slice thickness. Strong slice thickness dependence was identified on rubber particles, dense cork and solid acrylic inserts. All the other insert materials did not exhibit any variations as the slice thickness was varied. Dense cork

and solid acrylic materials had more uniform structures hence the results express the change in image noise as the slice thickness was being varied. The ABS showed no dependence on the slice thickness variation. ABS has air characteristics hence there is less photon attenuation across the four ABS different percentage fillings.

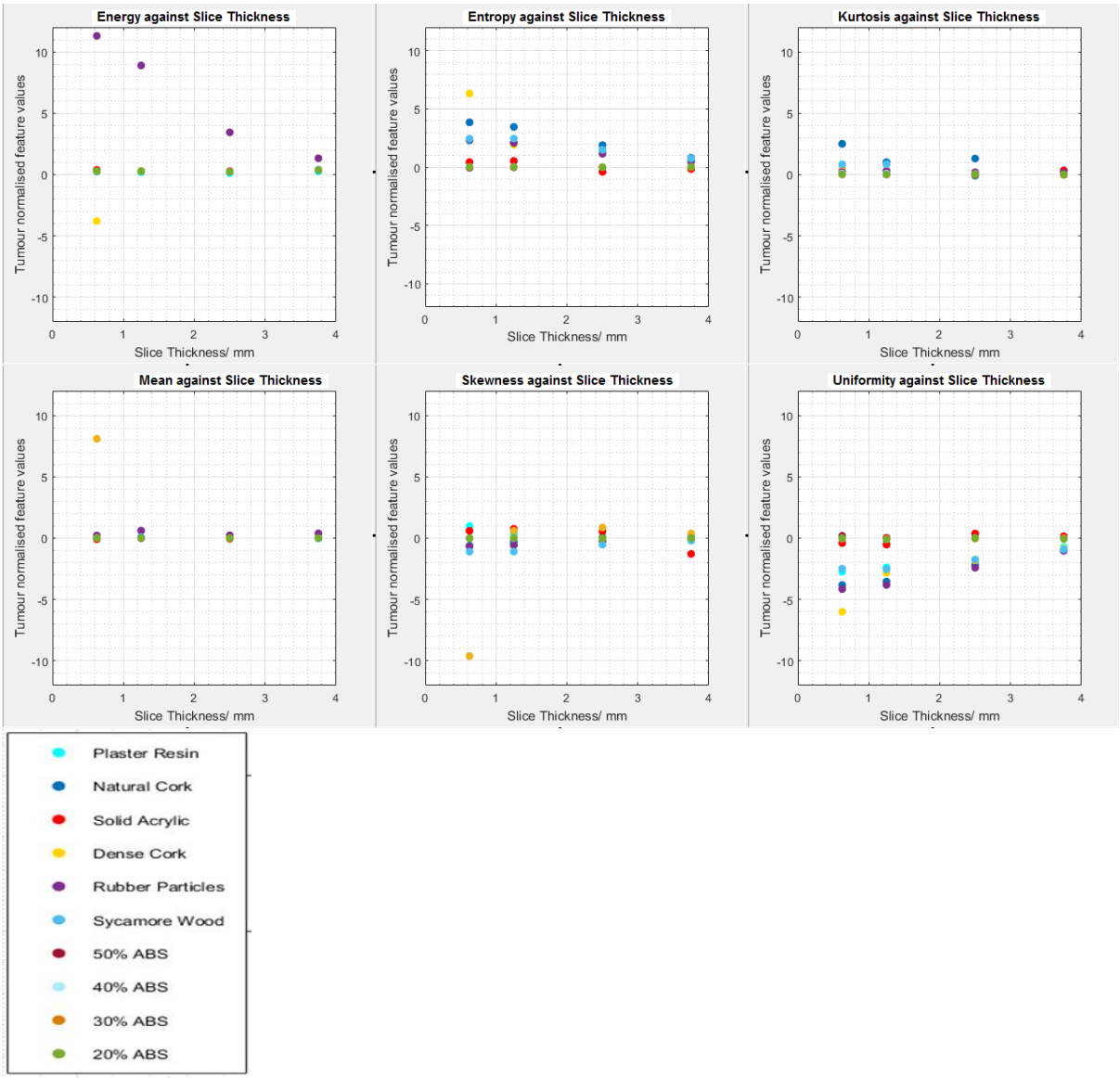

Fig 20. First-order statistics patient normalised feature difference trend due to slice thickness variation for the 10 inserts of the CCR phantom imaged on the GE Brightspeed machine.

The influence of cervical cancer tumour data used to normalise the phantom texture feature data was examined and presented in Fig 21. Fig 21 plots were obtained from the CCR phantom cartridge 2 images. The phantom data was obtained by changing the kV at constant mAs and constant slice thickness as well as other parameters that influenced texture feature values. Equation 36 was used to normalise the CCR cartridge 2 data. The mean

and standard deviation of each radiomic feature of the tumour extracted data at specific fractions (before treatment, 6th fraction, 11th fraction, 16th fraction, 20th fraction and 25th fraction) was used in equation 36.

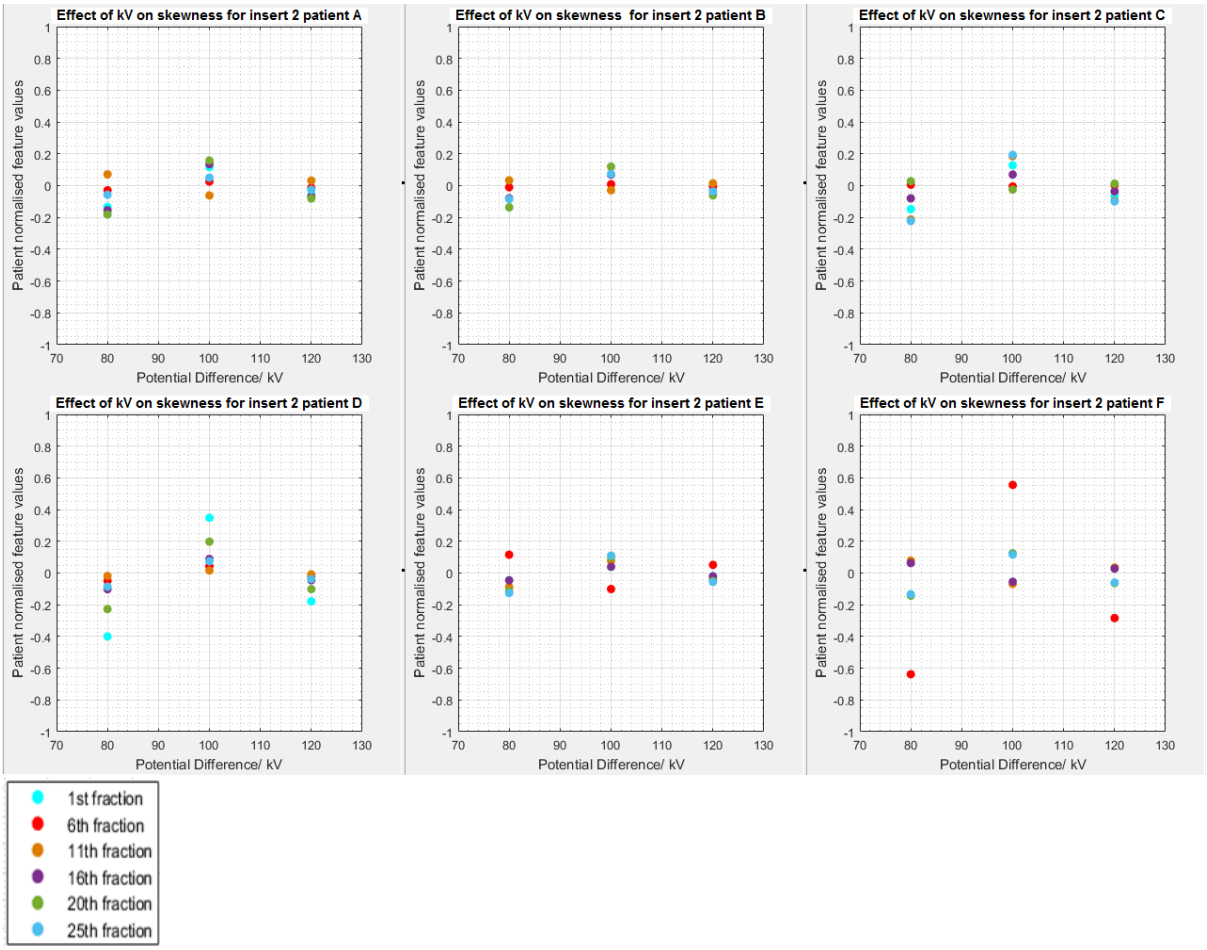

Fig 21. The effect of kV on a texture feature in relation to the tumour response to treatment. The six graphs illustrate the behaviour of the first order statistics feature, skewness, obtained from the 2nd insert for patients A to F.

Fig 22 and Fig 23 displayed the effect of the patient tumour data to the phantom data obtained by changing the kV imaging parameter using cartridge 9 and 10 (ABS cartridges). The graphs in Fig 22 and Fig 23 showed mostly a general decrease trend in the normalised feature values as the kV changed from low (80kV) to high (140kV). Few anomaly trends were also identified. Patient E in Fig 9 had a clear increase on its first fraction data whilst all the other fractions date showed the general decrease.

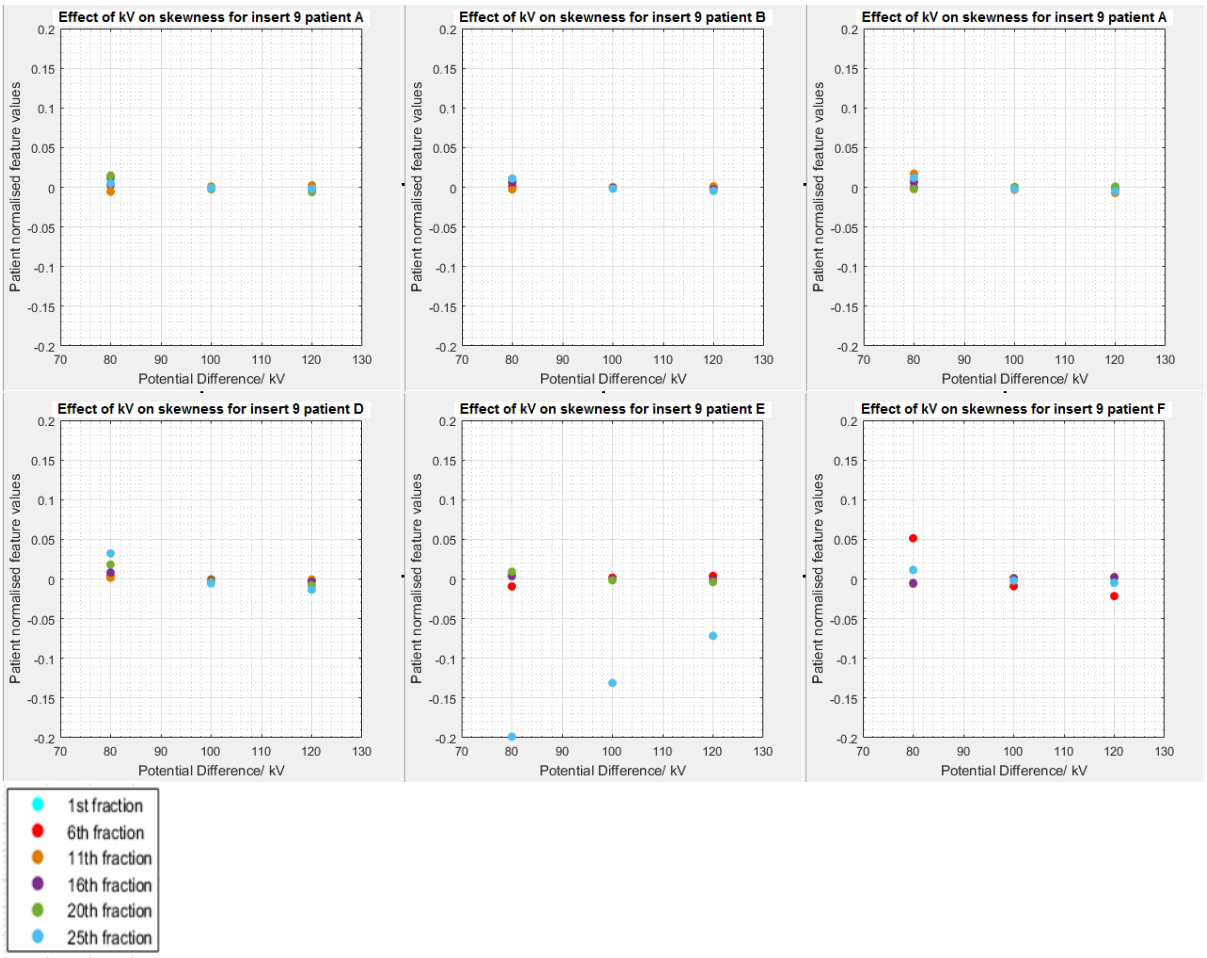

Fig 22. The effect of kV on a texture feature in relation to the tumour response to treatment. The six graphs demonstrate the behaviour of the first order statistics feature, skewness, obtained from the 9th insert for patients A to F.

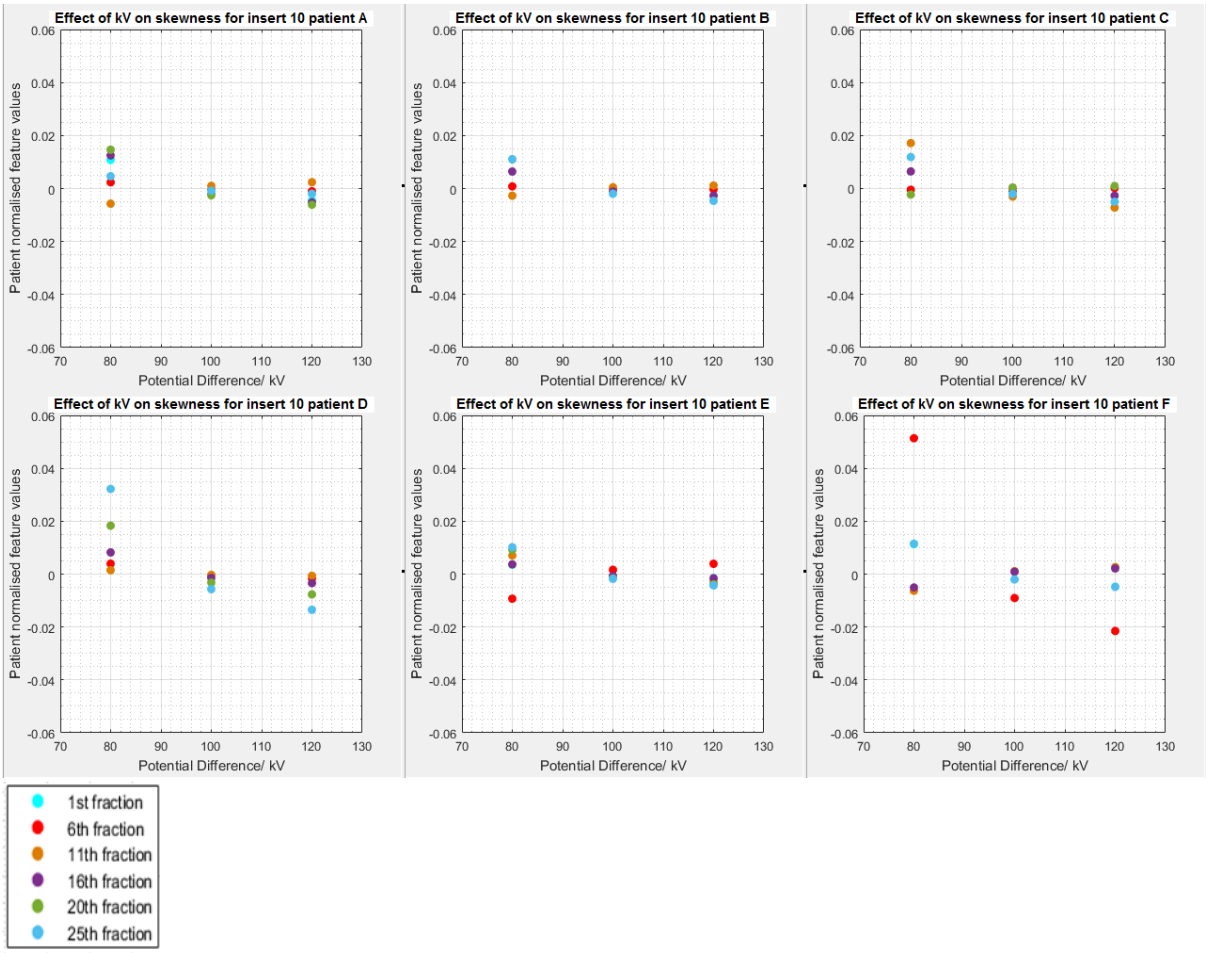

Fig 23. The effect of kV on a texture feature in relation to the tumour response to treatment. The six graphs display the behaviour of the first order statistics feature, skewness, obtained from the 10th insert for patients A to F.

Heat maps in Fig 24 to Fig 26 displayed the patient normalised CCR phantom texture features in four colours. The four colours indicated the extent of the radiomic texture features dependent on the tube potential difference (kV). The heat maps were used to identify radiomic texture features that were less dependent or completely independent of the imaging parameter being varied. Texture features that had green and greener colours across all the 10 cartridge materials in the heat map table were ideally robust, thus they were less dependent on the kV induced changes. The colours yellow and brown suggested greater dependence on the induced kV changes. The radiomic texture features presented in these maps where normalised to the cervical cancer tumour data using equation 36.

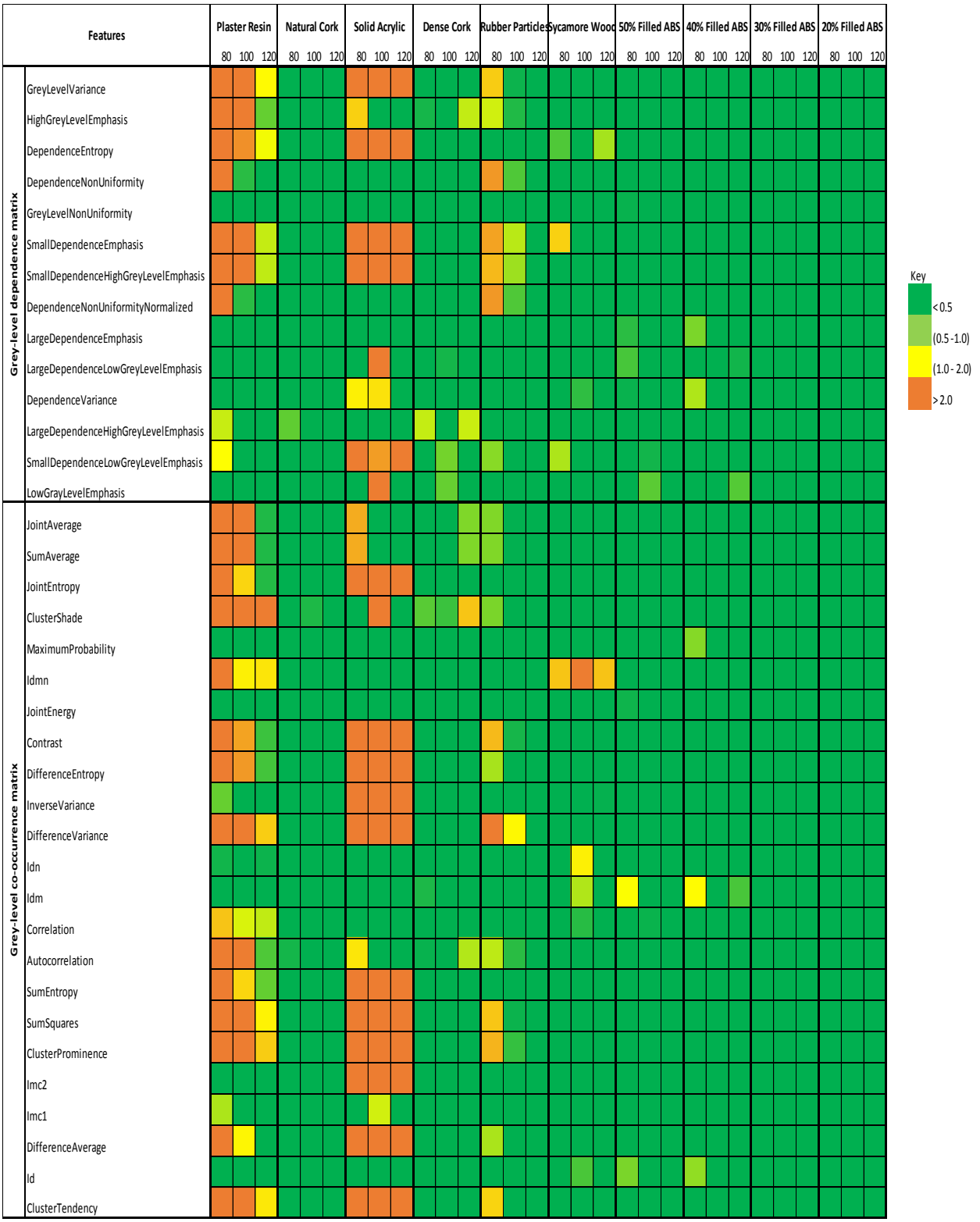

Fig 24. kV heat maps that represent the patient normalised GLDM and GLCM texture feature values of all the 10 cartridges that make up the CCR phantom shown in Fig 10, and the images used were acquired using a GE Light Speed Scanner.

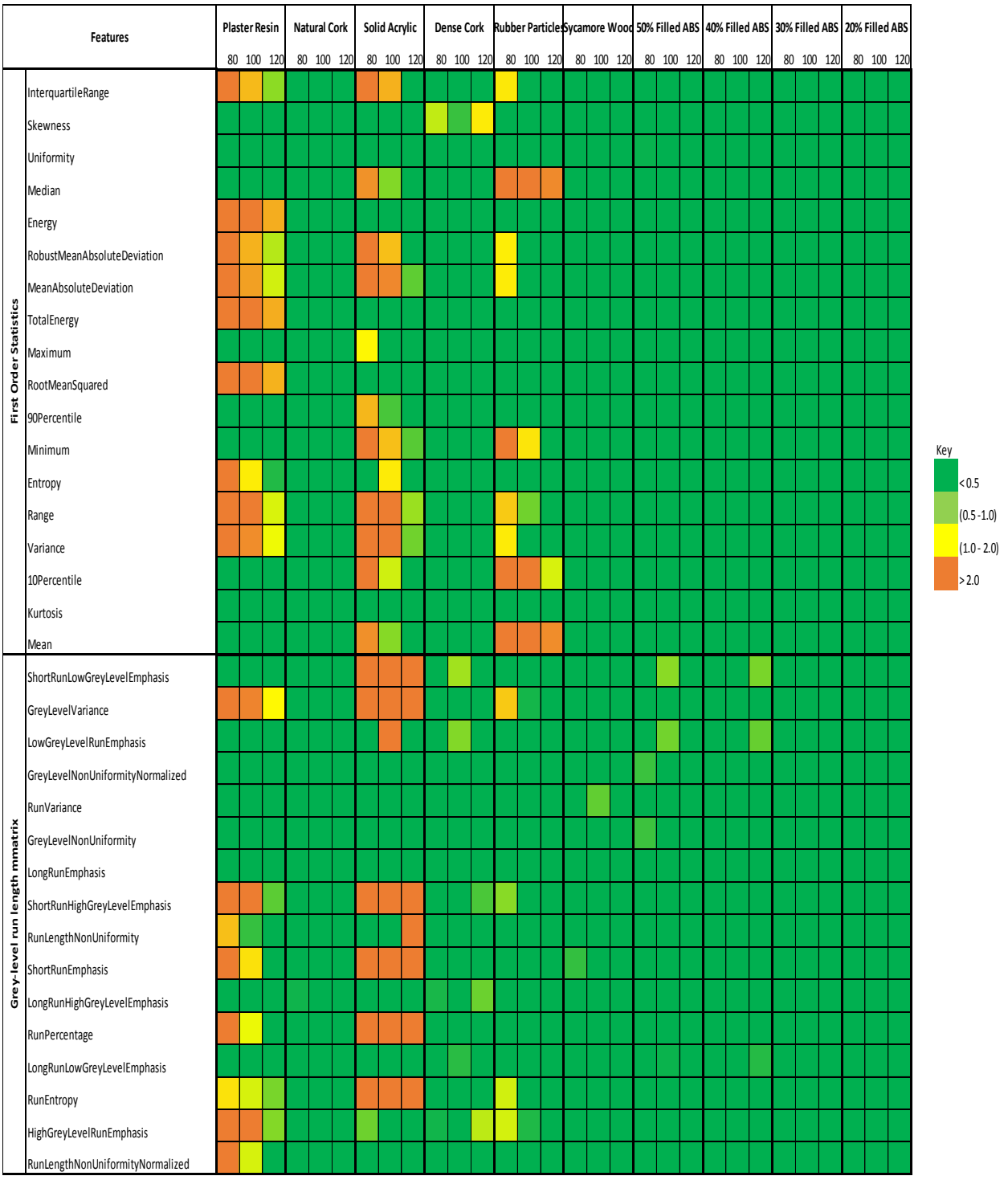

Fig 25. kV heat maps that represent the patient normalised first order statistics and GLRLM feature values of all the 10 cartridges that make up the CCR phantom shown in Fig 10, and the images used were acquired using a GE Light Speed CT machine.

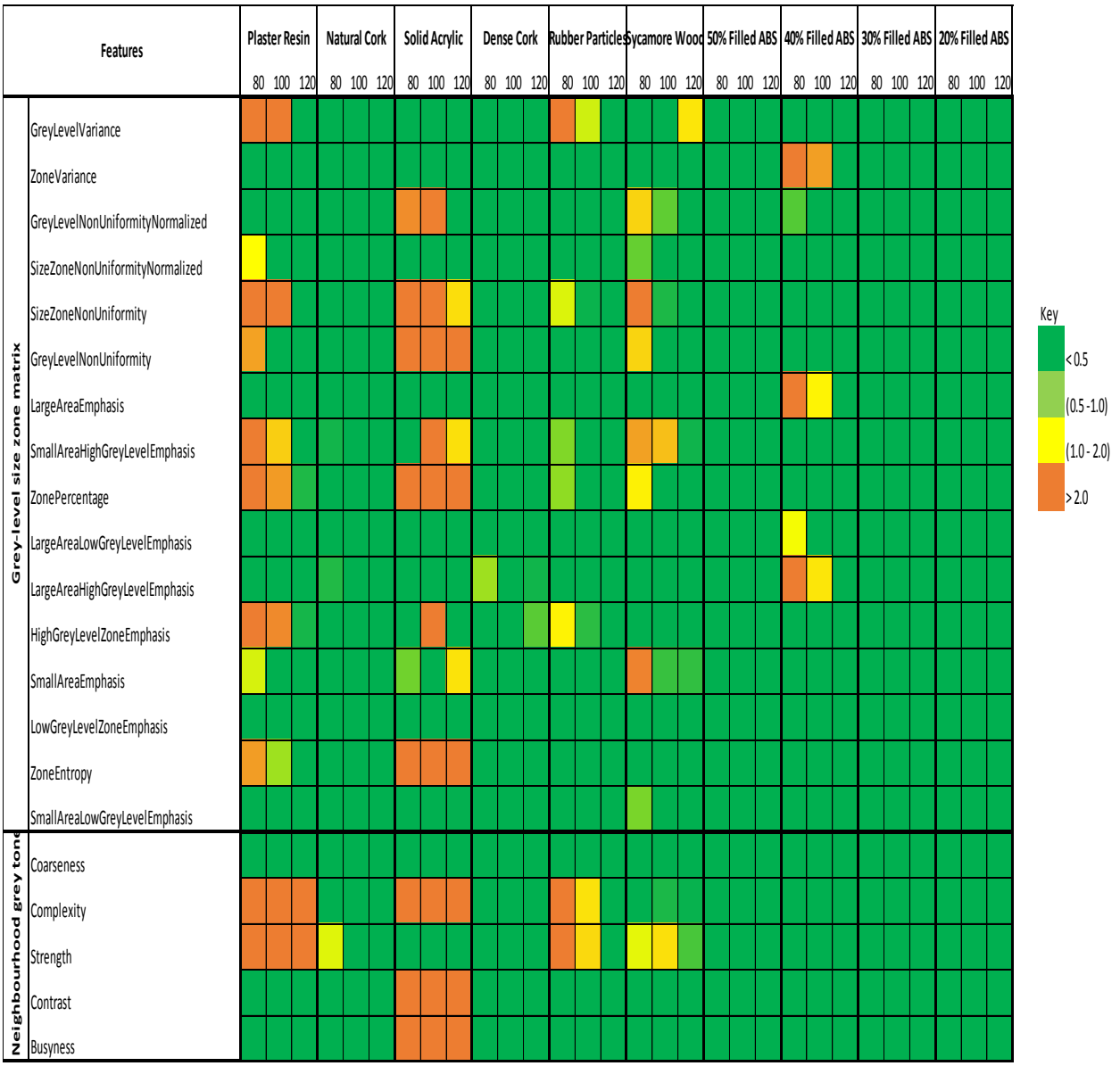

Fig 26. kV heat maps that represent the patient normalised GLSZM and NGTM feature values of all the 10 cartridges that make up the CCR phantom shown in Fig 10, and the images used were acquired using a GE Light Speed CT machine.

Fig 27 to Fig 32 heat maps displayed the behaviour of the radiomic texture features in relation to the mAs changes introduced during imaging. Positions that were coloured brown depend on the mAs. Regions that were coloured light green and yellow indicated texture features that was relatively independent of the mAs. Texture features that were in the green region across all the 10 cartridge materials in the heat map table were robust. The texture features were independent of the mAs induced changes.

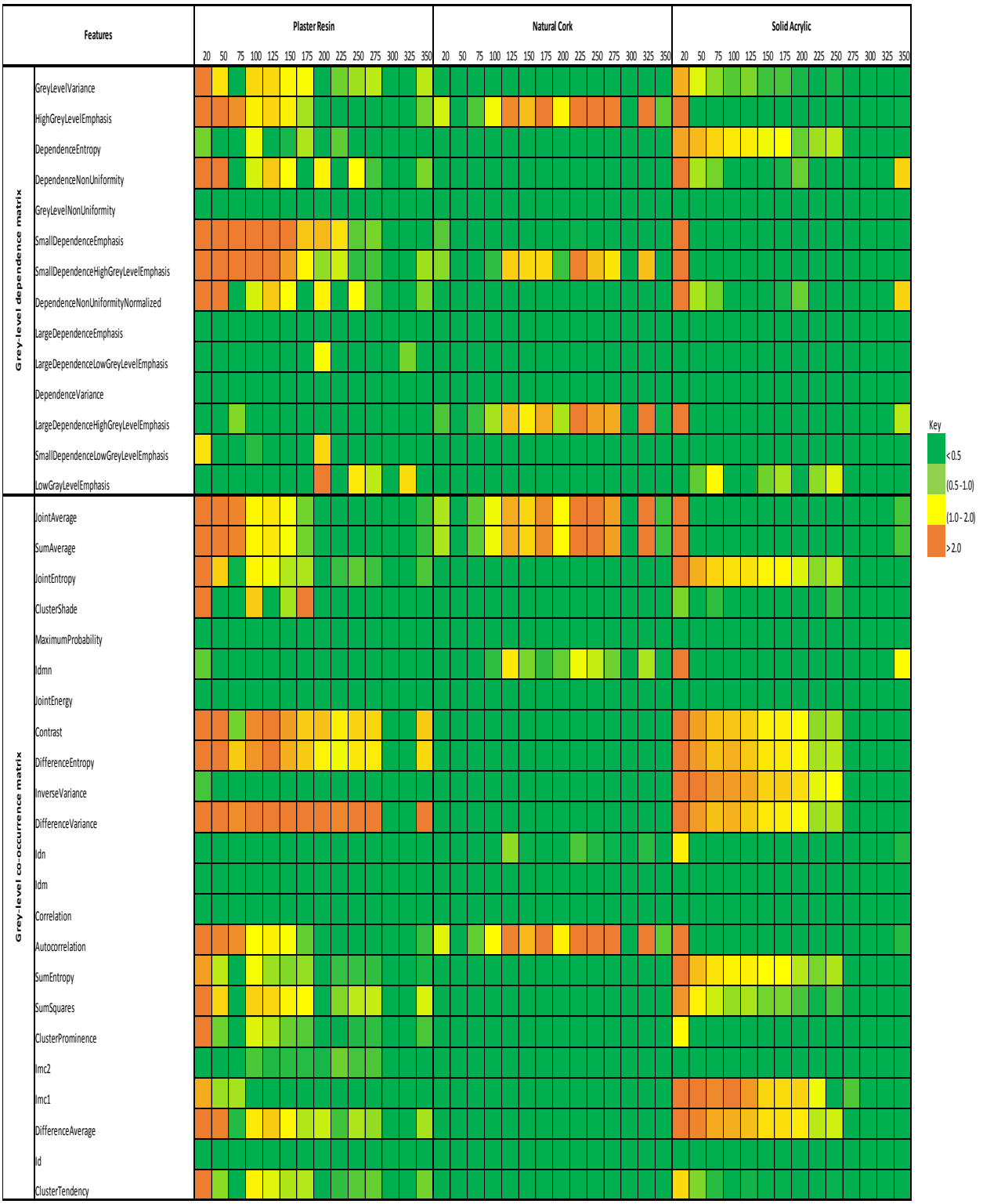

Fig 27. mAs heat maps that represent the patient normalised GLDM and GLCM texture feature values for the plaster resins, natural cork and solid acrylic cartridges that make up the CCR phantom shown in Fig 10, and the images used were acquired using a GE Light Speed CT machine.

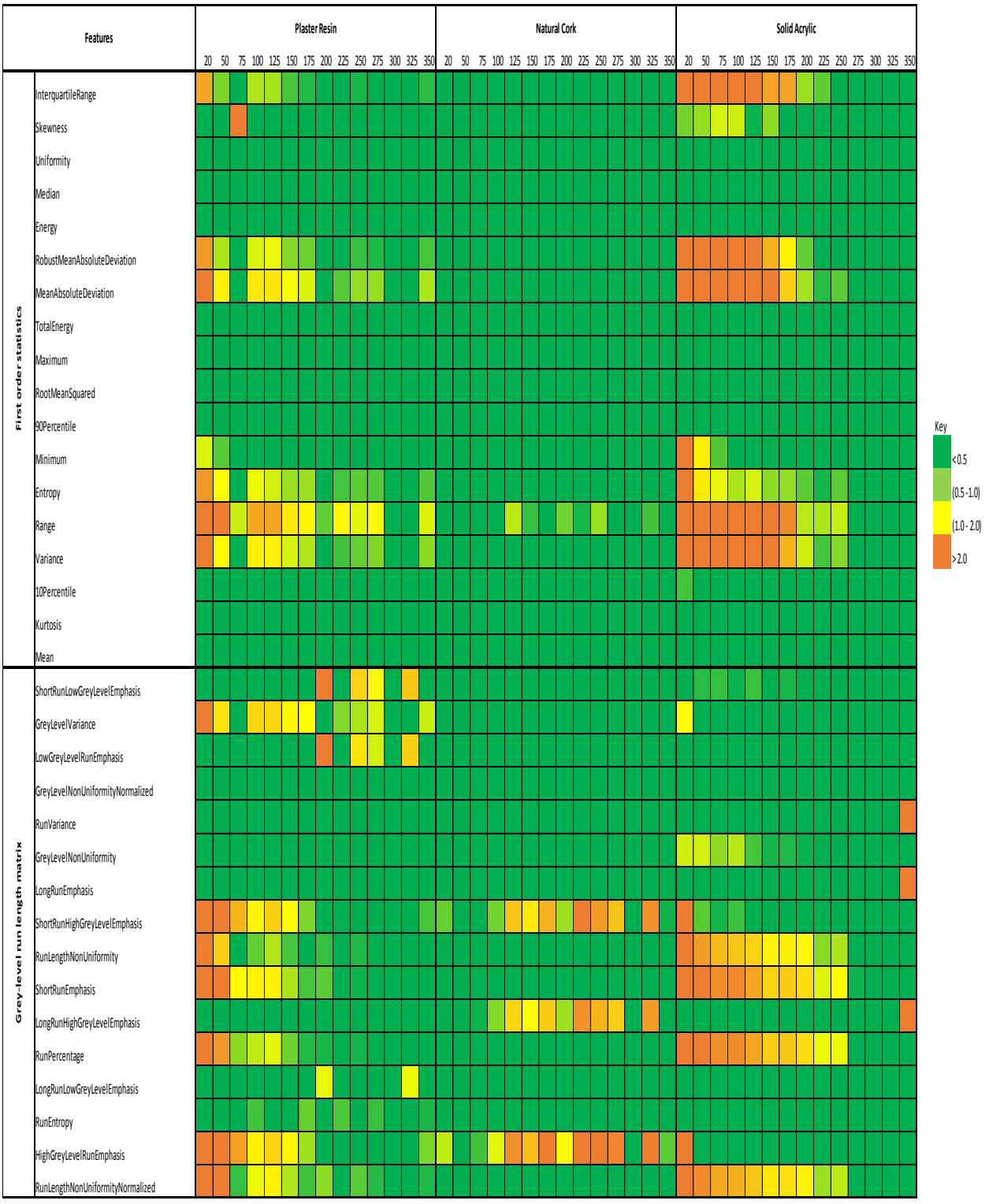

Fig 28. mAs heat maps that represent the patient normalised first order statistics and GLRLM feature values for the plaster resins, natural cork and solid acrylic cartridges that make up the CCR phantom shown in Fig 10, and the images used were acquired using a GE Light Speed CT machine.

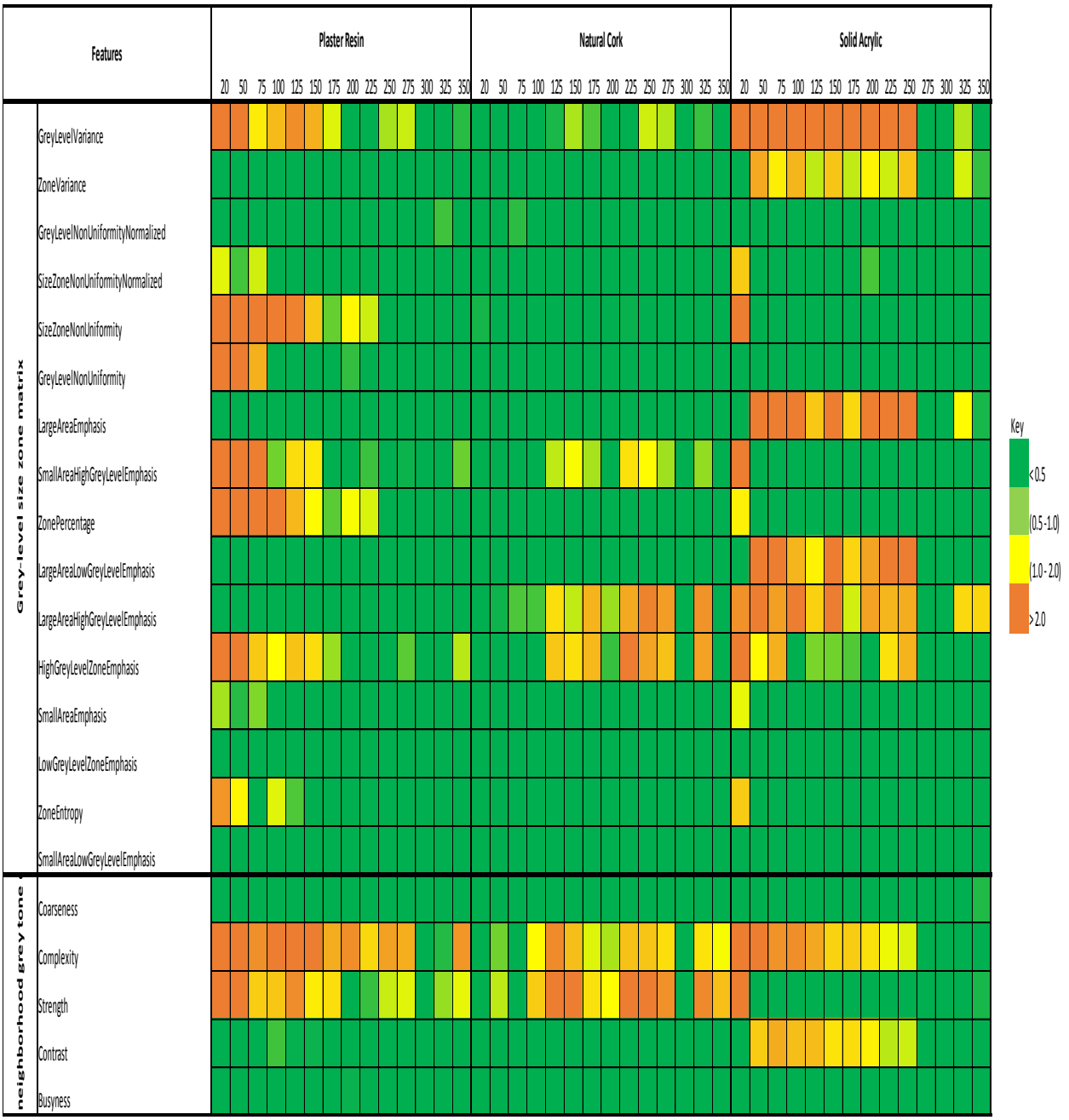

Fig 29. mAs heat maps that represent the patient normalised GLSZM and NGTM feature values for the plaster resins, natural cork and solid acrylic cartridges that make up the CCR phantom shown in Fig 10, and the images used were acquired using a GE Light Speed CT machine.

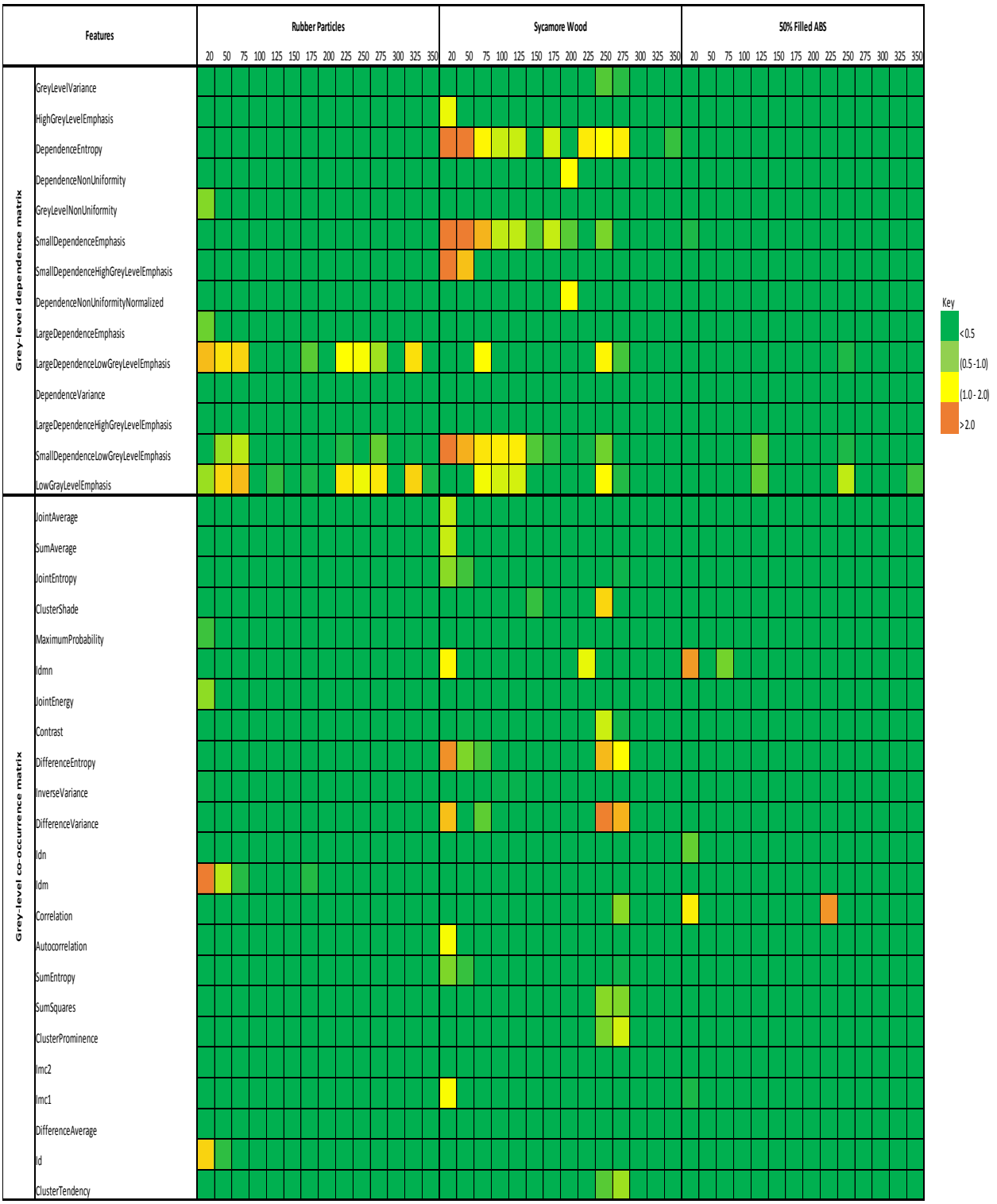

Fig 30. mAs heat maps that represent the patient normalised GLDM and GLCM texture feature values for the rubber particles, sycamore wood and 50% ABS cartridges that make up the CCR phantom shown in Fig 10, and the images used were acquired using a GE Light Speed CT machine.

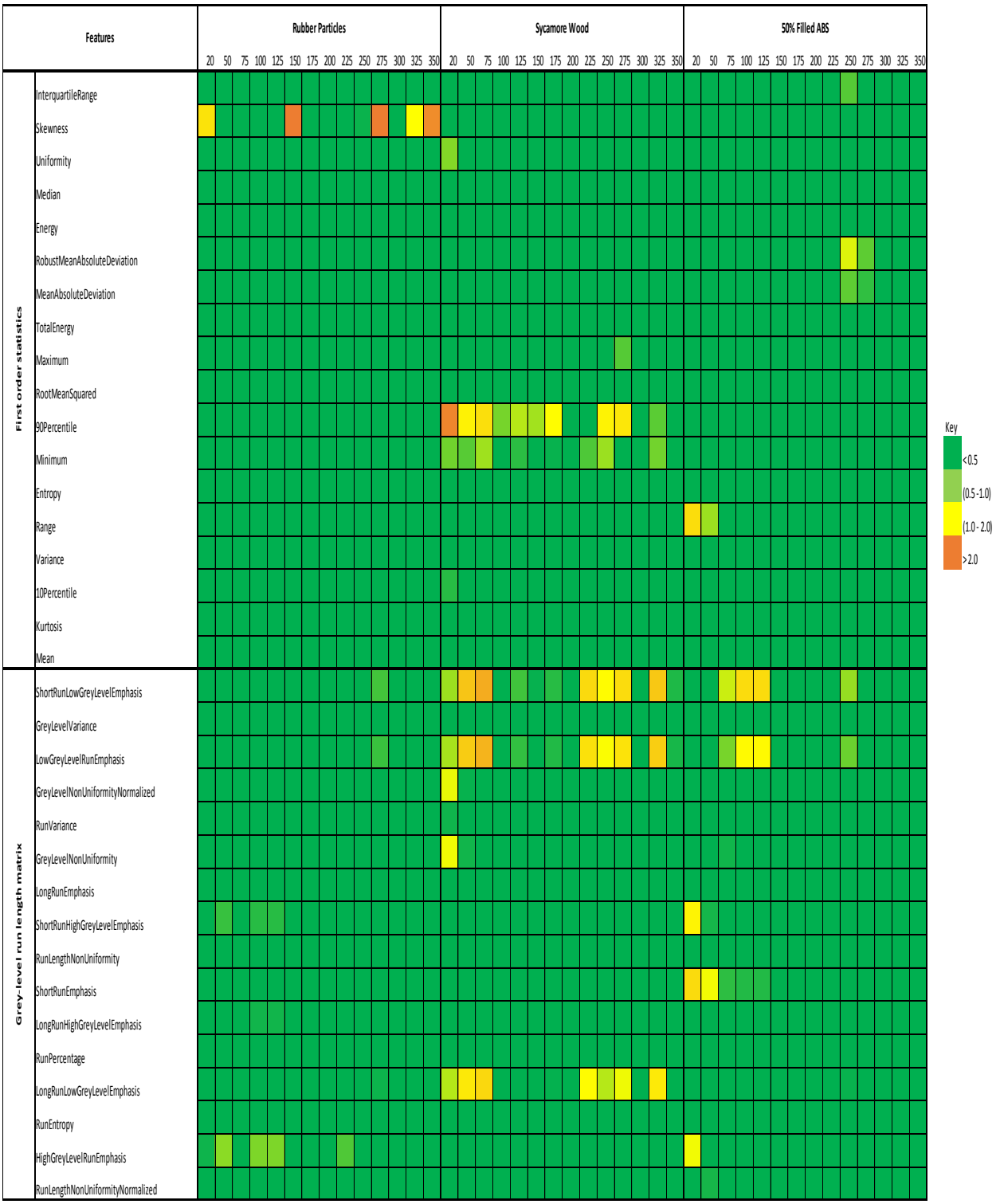

Fig 31. mAs heat maps that represent the patient normalised first order statistics and GLRLM feature values for the rubber particles, sycamore wood and 50% ABS cartridges that make up the CCR phantom shown in Fig 10, and the images used were acquired using a GE Light Speed CT machine.

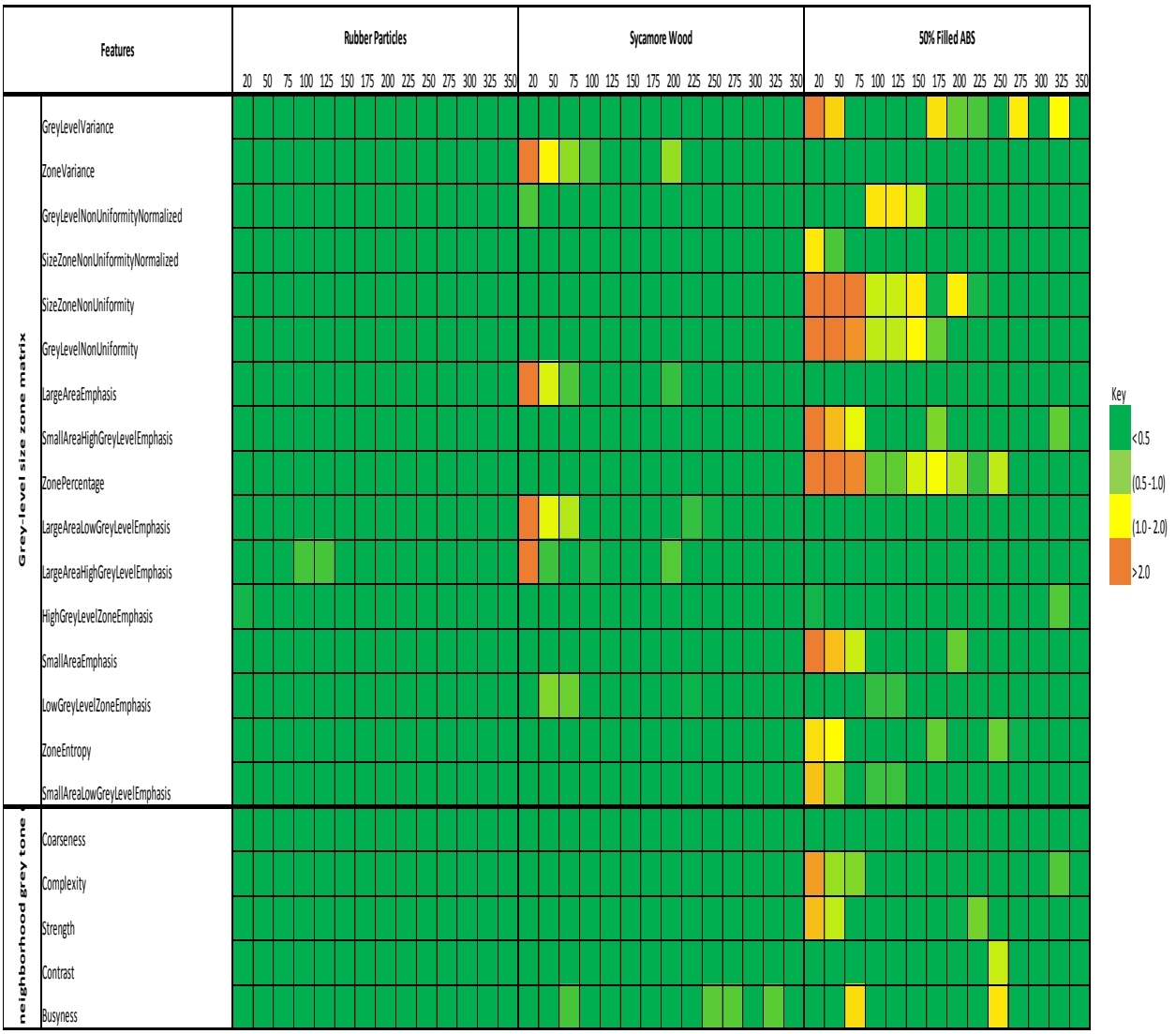

Fig 32. mAs heat maps that represent the patient normalised GLSZM and NGTM feature values for the rubber particles, sycamore wood and 50% ABS cartridges that make up the CCR phantom shown in Fig 10, and the images used were acquired using a GE Light Speed CT machine.

Fig 33, Fig 34 and Fig 35 below are heat maps that represent the patient normalised CCR phantom texture features in four colours. The four colours indicated the extent of the radiomic texture features dependent on the slice thickness. The colours represent the dependence of the texture features to the slice thickness with the greener colour representing less to non-dependence to the slice thickness. The colours yellow and brown suggested greater dependence on the induced slice thickness changes.

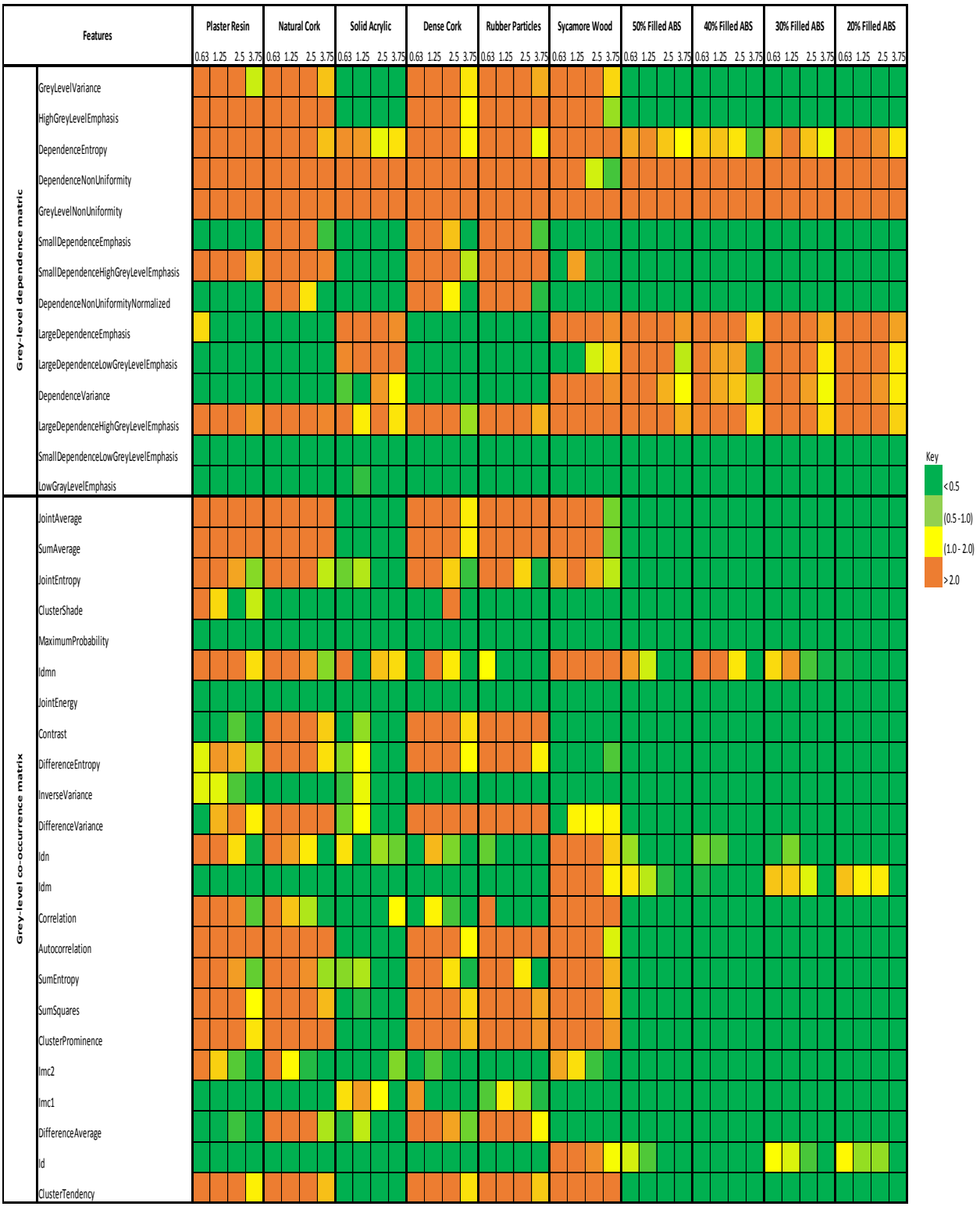

Fig 33. Slice thickness Heat maps that represent the patient normalised GLDM and GLCM texture feature values of all the 10 cartridges that make up the CCR phantom shown in Fig 10, and the images used were acquired using a GE Light Speed CT machine

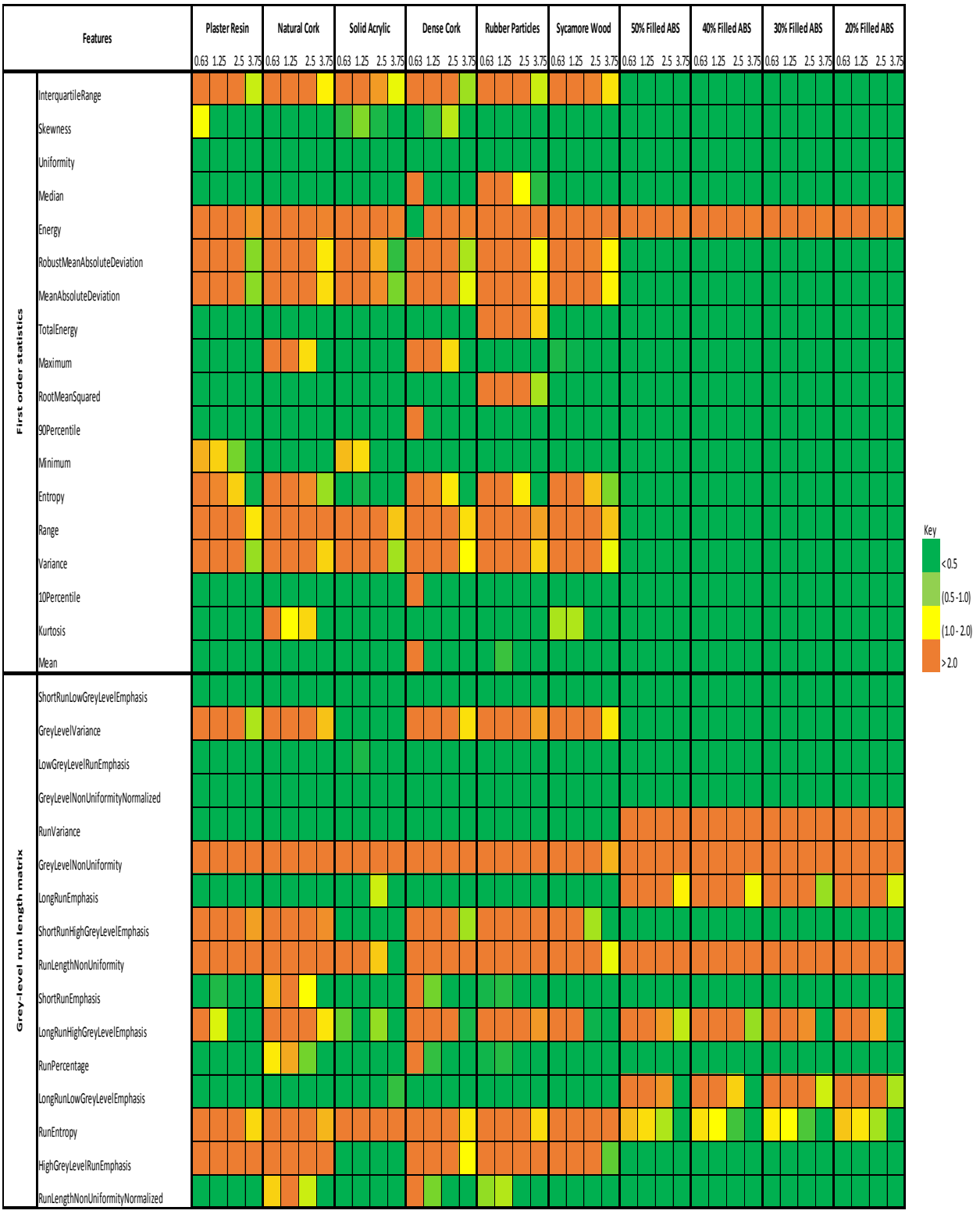

Fig 34. Slice thickness heat maps that represent the patient normalised first order statistics and GLRLM feature values of all the 10 cartridges that make up the CCR phantom shown in Fig 10, and the images used were acquired using a GE Light Speed CT machine

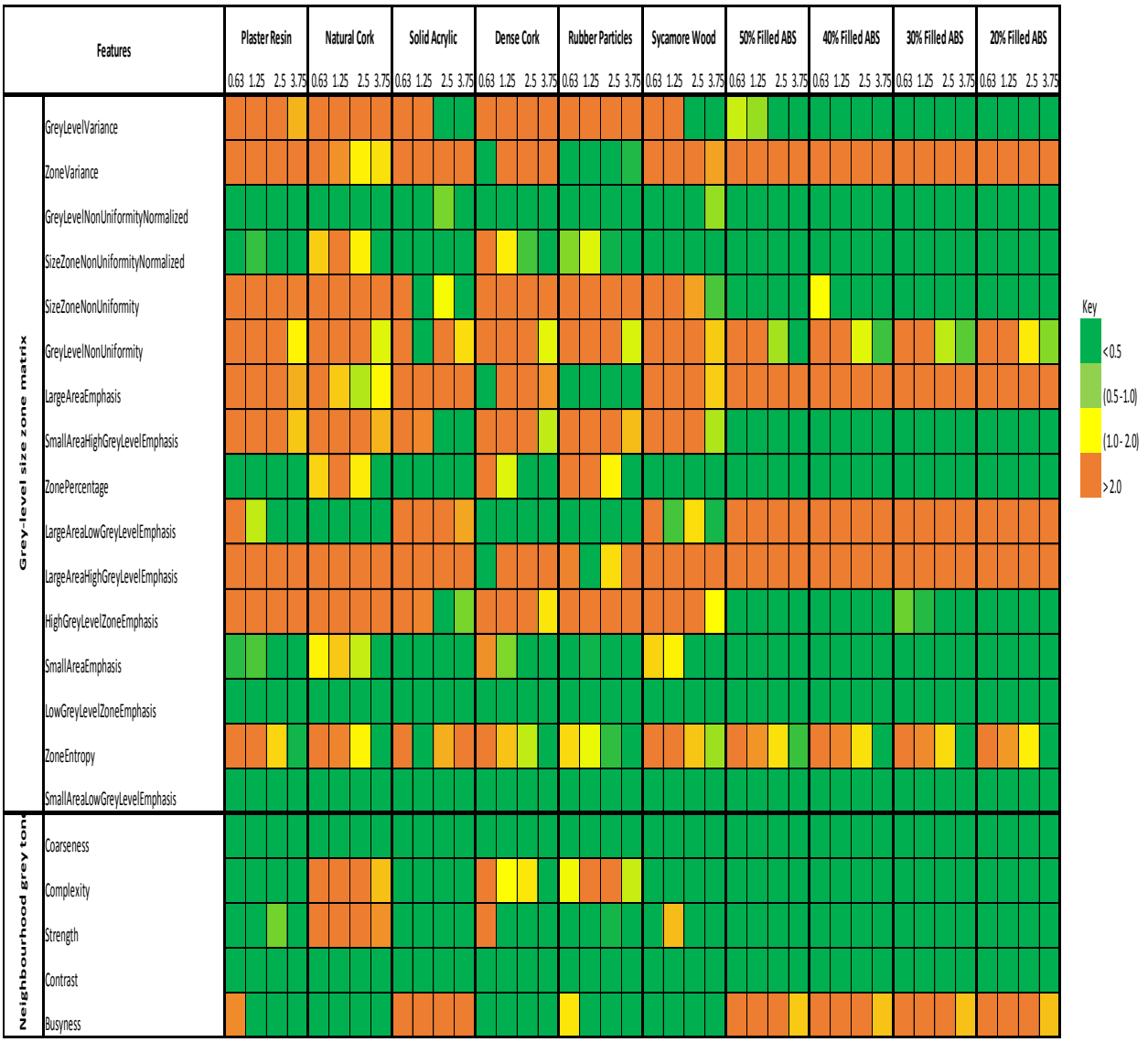

Fig 35. Slice thickness heat maps that represent the patient normalised GLSZM and NGTM feature values of all the 10 cartridges that make up the CCR phantom shown in Fig 10, and the images used were acquired using a GE Light Speed CT machine.

In this study, CCR phantom inserts (non-homogenous inserts, e.g. rubber and sycamore inserts and homogenous inserts e.g. acrylic) images were used to extract the pixel intensities at specific ROIs for the manual radiomic features calculations. Average image noise from four 10x10 ROI matrices obtained from the image pixel intensity matrix (512x512 image matrix) was estimated to ascertain its relationship to slice thickness, kV and mAs changes. *Table 4* to *Table 6* displays the results of the manner in which image noise varied with changes in CT technique parameters.

Table 4: Results of kilovoltage peak influence on image noise from acrylic insert.

Kilovoltage peak/ kV	Noise	Standard Deviation	COV%
80	11.34	0.24	2.15
100	11.33	0.56	4.96
120	11.11	0.36	3.25
140	11.05	0.15	1.32

Table 5: Results of slice thickness influence on image noise from rubber particles insert.

Slice Thickness/ mm	Noise	Standard Deviation	COV%
1	4.68	0.38	8.04
2	5.00	0.11	2.19
3	3.83	0.30	7.95
4	4.89	0.22	4.39
5	9.95	0.31	3.10

Table 6: Results of tube current influence on image noise from rubber particles insert.

Tube Current/ mAs	Noise	Standard Deviation	COV%
150	11.28	0.49	4.34
200	11.26	0.50	4.41
250	10.99	0.41	3.77
300	11.41	0.36	3.14
350	11.07	0.37	3.37

The results of the hand calculated radiomic texture features relationship to CT technique parameters was compiled in *Table 7* to *Table 12* below. *Table 7* and *Table 8* constituted the results of the manually computed grey level co-occurrence texture feature values that showed the impact of kV on the radiomic texture features. Examples of image matrices used to calculate the radiomic texture features are resembled by *Table 15* to *Table 18* in the appendix.

Table 7: kV influence on GLCM texture feature estimated using 10x10 matrices for data of wood insert.

Kilovoltage peak	***80 kV***	***100 kV***	***120 kV***	***140 kV***	***Average***	***StDv***	***%COV***
Mean (μ)	1129.14	1143.62	1150.70	1154.79	1144.6	9.8	0.9
Energy	0.02	0.03	0.03	0.04	0.0	0.0	24.9
Variance (σ^2)	16.32	7.18	7.87	5.15	9.1	4.3	46.8
Entropy	6.11	5.48	5.41	5.09	5.5	0.4	6.7
Contrast	24.82	8.05	6.05	4.71	10.9	8.1	74.4
Correlation	3.70	3.16	4.93	2.79	3.6	0.8	22.2
Homogeneity	0.21	0.41	0.29	0.41	0.3	0.1	25.8
Sum average	1140.20	1150.25	1162.42	1159.57	1153.1	8.7	0.8
Sum variance	39.61	20.68	25.75	15.89	25.5	8.9	34.8
Sum Entropy	-2.89	-2.62	-2.34	-2.55	-2.6	0.2	-7.7
Difference average	1121.95	1139.12	1141.14	1151.71	1138.5	10.7	0.9
Difference variance	9.25	3.55	1.46	1.78	4.0	3.1	78.1
Difference Entropy	-2.26	-1.86	-1.54	-1.60	-1.8	0.3	-15.5
HX	-2.65	-2.26	-2.26	-2.12	-2.3	0.2	-8.5
HXY1	5.28	4.52	4.53	4.24	4.6	0.4	8.3
HXY2	5.30	4.52	4.52	4.24	4.6	0.4	8.5
Imc1	-0.30	-0.42	-0.40	-0.40	-0.4	0.0	1.1
Imc2	0.00	0.00	0.00	0.00	0.0	0.0	0.0

Table 8: kV influence on GLCM texture feature estimated using 10x10 matrices for data of acrylic insert.

Kilovoltage peak	***80 kV***	***100 kV***	***120 kV***	***140 kV***	***Average***	***StDv***	***%COV***
Mean (μ)	128.80	144.07	150.67	155.18	144.7	10.0	6.9
Energy	0.01	0.02	0.02	0.03	0.0	0.0	28.8
Variance (σ2)	12.13	10.33	7.00	5.06	8.6	2.8	32.0
Entropy	6.55	6.21	5.80	5.54	6.0	0.4	6.4
Contrast	17.73	8.77	5.63	5.37	9.4	5.0	53.4
Correlation	3.26	5.94	4.19	2.37	3.9	1.3	33.5
Homogeneity	0.25	0.37	0.35	0.39	0.3	0.1	15.1
Sum average	135.60	151.13	159.34	160.36	151.6	9.9	6.5
Sum variance	30.78	32.53	22.38	14.86	25.1	7.1	28.1
Sum Entropy	-2.99	-2.98	-2.76	-2.53	-2.8	0.2	-6.7
Difference average	125.37	139.24	143.96	151.84	140.1	9.6	6.9
Difference variance	6.37	3.74	1.80	1.98	3.5	1.8	52.9
Difference Entropy	-2.20	-1.90	-1.63	-1.67	-1.9	0.2	-12.4
HX	-2.56	-2.48	-2.27	-2.15	-2.4	0.2	-7.0
HXY1	5.12	4.97	4.54	4.29	4.7	0.3	7.0
HXY2	5.12	4.97	4.54	4.29	4.7	0.3	7.0
Imc1	-0.56	-0.50	-0.56	-0.58	-0.5	0.0	0.7
Imc2	0.00	0.00	0.00	0.00	0.0	0.0	0.0

The results in *Table 9* and *Table 10* resembled the variability with which the grey level co-occurrence matrix features varied with slice thickness.

Table 9: Toshiba Unit: Slice thickness influence on GLCM texture feature estimated using 10x10 matrices of rubber insert.

Slice Thickness	***1mm***	***2mm***	***3mm***	***4mm***	***5mm***	***Average***	***StDv***	***%COV***
Mean (μ)	-530.01	-598.52	-528.72	-527.84	-581.77	-553.4	30.5	-5.5
Energy	0.02	0.02	0.02	0.02	0.01	0.0	0.0	18.9
Variance (σ2)	17.17	24.92	13.77	22.97	97.72	35.3	31.5	89.1
Entropy	6.15	6.30	6.24	6.08	6.74	6.3	0.2	3.7
Contrast	3.89	4.03	5.37	4.12	3.99	4.3	0.5	12.8
Correlation	15.22	22.90	10.24	20.91	95.73	33.0	31.7	96.0
Homogeneity	0.42	0.48	0.42	0.45	0.41	0.4	0.0	5.9
Sum average	-523.02	-586.03	-520.70	-518.67	-568.54	-543.4	28.3	-5.2
Sum variance	64.78	95.65	46.86	87.75	386.89	136.4	126.4	92.7
Sum Entropy	-3.30	-3.40	-3.14	-3.27	-3.70	-3.4	0.2	-5.6
Difference average	-535.40	-609.51	-535.23	-535.44	-593.37	-561.8	32.8	-5.8
Difference variance	1.33	1.82	2.22	1.68	1.32	1.7	0.3	20.0
Difference Entropy	-1.50	-1.57	-1.67	-1.51	-1.50	-1.6	0.1	-4.3
HX	-2.67	-2.87	-2.62	-2.74	-3.22	-2.8	0.2	-7.5
HXY1	5.35	5.73	5.20	5.48	6.43	5.6	0.4	7.7
HXY2	5.35	5.73	5.24	5.48	6.43	5.6	0.4	7.5
Imc1	-0.30	-0.20	-0.37	-0.22	-0.10	-0.2	0.1	2.2
Imc2	0.00	0.00	0.00	0.00	0.00	0.0	0.0	0.0

Table 10: GE unit: Slice thickness influence on GLCM texture feature estimated using 10x10 matrices of acrylic insert.

Slice Thickness	**1.25 mm**	**2.5 mm**	**3.75 mm**	**5 mm**	***Average***	***StDv***	***%COV***
Mean (μ)	561.09	562.27	563.46	564.44	562.8	1.3	0.2
Energy	0.02	0.03	0.03	0.04	0.0	0.0	30.2
Variance (σ^2)	17.90	8.82	7.72	5.48	10.0	4.7	47.4
Entropy	6.09	5.64	5.50	5.03	5.6	0.4	6.8
Contrast	11.50	4.91	5.06	2.38	6.0	3.4	56.5
Correlation	12.15	6.36	5.25	4.29	7.0	3.1	43.6
Homogeneity	0.26	0.37	0.36	0.51	0.4	0.1	24.2
Sum average	572.18	569.55	571.89	569.88	570.9	1.2	0.2
Sum variance	60.11	30.36	26.07	19.54	34.0	15.5	45.7
Sum Entropy	-3.03	-2.85	-2.79	-2.66	-2.8	0.1	-4.6
Difference average	552.86	556.82	556.84	560.20	556.7	2.6	0.5
Difference variance	3.34	1.60	1.67	0.94	1.9	0.9	46.8
Difference Entropy	-1.87	-1.56	-1.54	-1.30	-1.6	0.2	-12.9
HX	-2.59	-2.34	-2.31	-2.09	-2.3	0.2	-7.6
HXY1	5.33	4.69	4.63	4.19	4.7	0.4	8.7
HXY2	5.33	4.69	4.63	4.19	4.7	0.4	8.7
Imc1	-0.40	-0.41	-0.38	-0.40	-0.4	0.0	0.3
Imc2	0.00	0.00	0.00	0.00	0.0	0.0	0.0

Displayed in *Table 11* and *Table 12* are the results of the mAs influence on the radiomic features.

Table 11: Toshiba unit: mAs influence on GLCM texture feature estimated using 10x10 matrices of Wood material.

Tube Current/ mAs	***150***	***200***	***250***	***300***	***350***	***Average***	***StDv***	***%COV***
Mean (μ)	-529.46	-508.43	-515.02	-527.06	-513.68	-518.7	8.1	-1.6
Energy	0.01	0.01	0.02	0.01	0.02	0.0	0.0	46.4
Variance (σ2)	234.90	205.75	20.39	195.13	22.24	135.7	94.3	69.5
Entropy	6.84	7.13	5.80	6.92	6.07	6.6	0.5	7.9
Contrast	5.80	5.73	2.83	6.23	3.36	4.8	1.4	29.3
Correlation	232.00	202.88	20.90	-134.92	20.56	68.3	134.7	197.3
Homogeneity	0.38	0.38	0.45	0.34	0.47	0.4	0.0	11.6
Sum average	-505.33	-449.51	-502.03	-493.18	-499.36	-489.9	20.6	-4.2
Sum variance	966.55	1587.83	86.43	785.68	85.62	702.4	569.3	81.0
Sum Entropy	-4.00	-3.73	-3.25	-2.95	-2.93	-3.4	0.4	-12.6
Difference average	-557.09	-537.08	-526.61	-554.97	-526.57	-540.5	13.3	-2.5
Difference variance	2.15	2.03	0.90	2.10	1.32	1.7	0.5	29.4
Difference Entropy	-1.70	-1.68	-1.34	-1.68	-1.48	-1.6	0.1	-9.1
HX	3.58	3.61	2.67	3.64	2.77	3.3	0.4	13.4
HXY1	6.97	7.22	5.36	7.20	5.55	6.5	0.8	12.8
HXY2	7.17	7.35	5.10	7.20	5.55	6.5	0.9	14.7
Imc1	-0.03	-0.02	0.17	-0.07	0.19	0.0	0.1	-3.6
Imc2	0.69	0.59	0.00	0.65	0.00	0.6	0.0	6.8

Table 12: GE unit mAs influence on GLCM texture feature estimated using 10x10 matrices of Acrylic material.

Tube Current/ mAs	***150***	***200***	***250***	***300***	***350***	***Average***	***StDv***	***%COV***
Mean (μ)	563.81	564.98	565.69	566.06	566.81	565.5	1.0	0.2
Energy	0.02	0.03	0.03	0.03	0.02	0.0	0.0	8.6
Variance (σ2)	9.21	7.14	7.73	6.33	8.01	7.7	1.0	12.4
Entropy	5.68	5.39	5.33	5.34	5.54	5.5	0.1	2.5
Contrast	3.55	3.64	2.68	3.30	3.25	3.3	0.3	10.3
Correlation	7.43	5.32	6.29	4.53	6.38	6.0	1.0	16.5
Homogeneity	0.43	0.40	0.51	0.43	0.46	0.4	0.0	8.3
Sum average	570.63	571.96	571.40	571.15	572.62	571.6	0.7	0.1
Sum variance	33.27	24.93	27.83	21.42	28.78	27.2	4.0	14.5
Sum Entropy	-2.89	-2.78	-2.02	-2.71	-2.87	-2.7	0.3	-12.2
Difference average	558.52	559.57	561.25	562.48	562.44	560.9	1.6	0.3
Difference variance	1.25	1.17	1.11	1.10	1.19	1.2	0.1	4.6
Difference Entropy	-1.44	-1.33	-1.39	-1.42	-1.40	-1.4	0.0	-2.5
HX	-2.41	-2.30	-2.34	-2.26	-2.31	-2.3	0.1	-2.2
HXY1	4.83	4.61	4.65	4.49	4.62	4.6	0.1	2.3
HXY2	4.83	4.61	4.68	4.51	4.62	4.7	0.1	2.2
Imc1	-0.35	-0.34	-0.29	-0.38	-0.40	-0.4	0.0	-10.3
Imc2	0.00	0.00	0.00	0.00	0.00	0.0	0.0	0.0

Fig 36 and Fig 37 displayed the sensitivity of the radiomic texture features to the ROI volume. In Fig 36, the plotted feature values showed a decreasing trend as the sampling volume was increased. In Fig 37, the plotted feature values displayed an increasing trend as the sampling volume was increased. The observations indicated

that the features were sensitive and dependent on the number of voxels used in the calculation of the textural features. As the size of the ROI volume changes then the value of the feature sampled changes, either increasing or decreasing according to the behaviour of the texture feature.

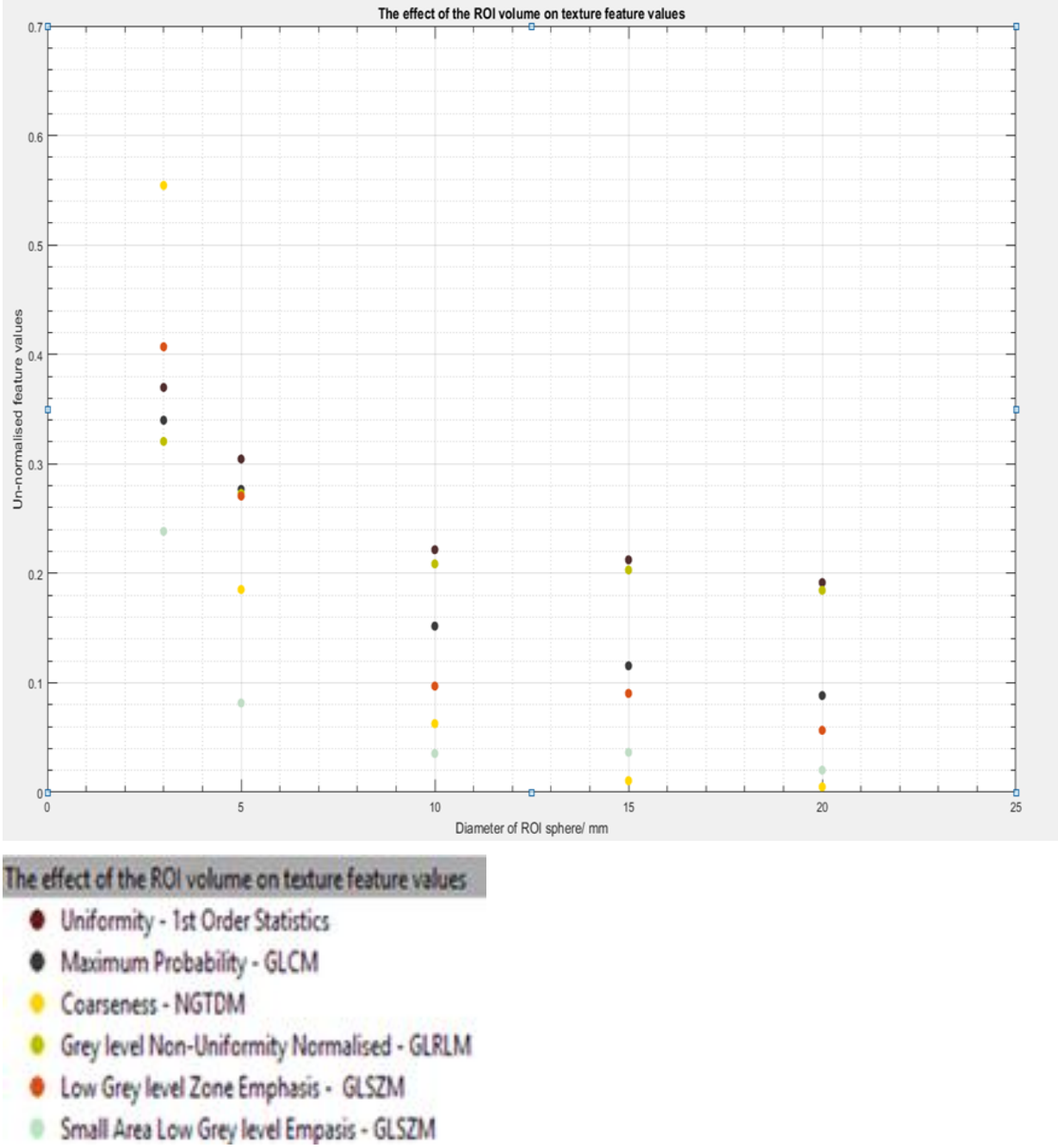

Fig 36. Comparison of sensitivity of textural features in relation to the sampling volume

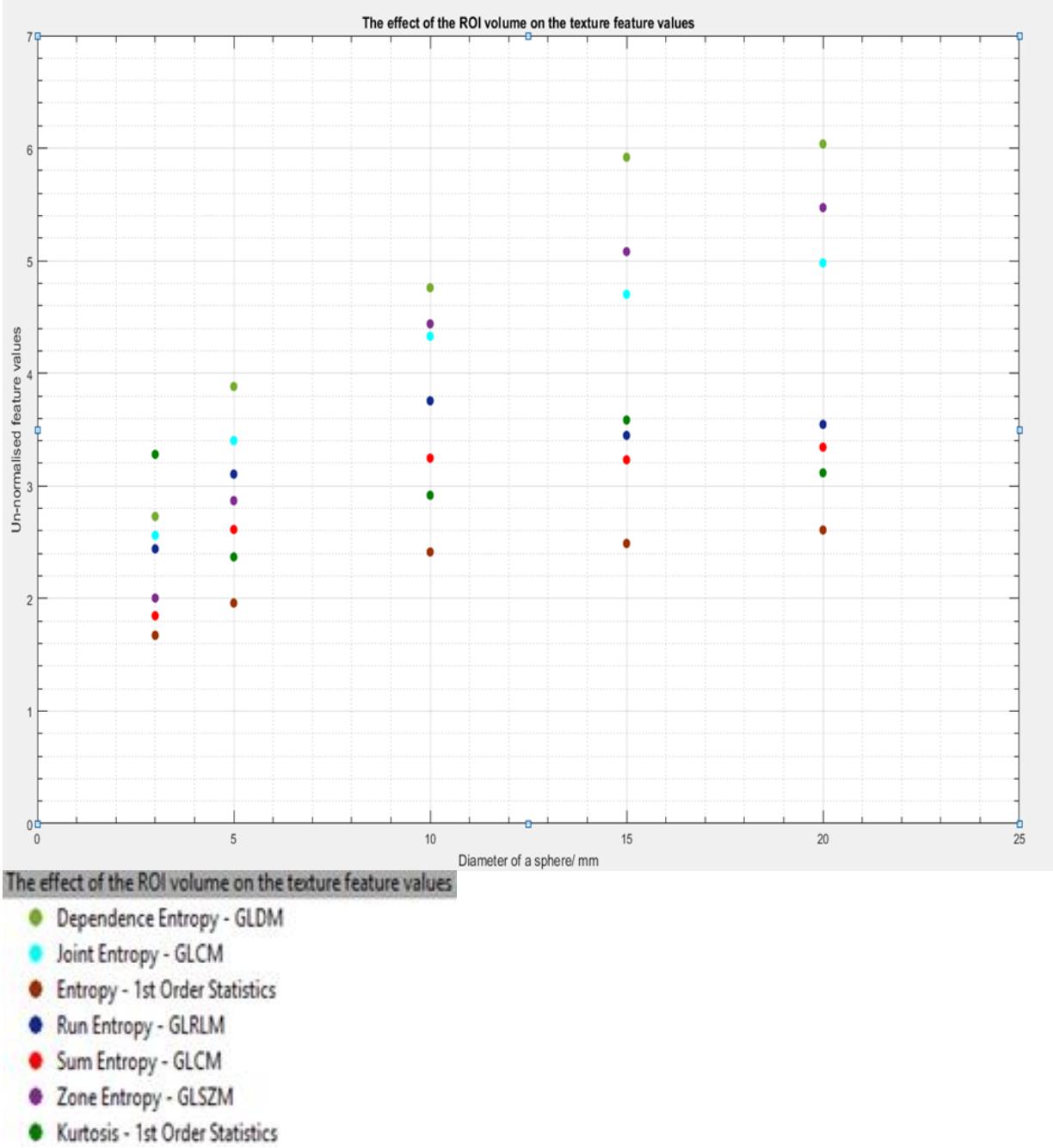

Fig 37. Comparison of sensitivity of textural features in relation to the sampling volume

4.1.3 Cervical cancer patient cohort results

Fig 38 to Fig 42 displayed the patient tumour response to radiotherapy fractionated treatment. The investigation utilised some selected robust radiomic features in capturing the subtle response of cervical cancer to radiotherapy treatment. Fig 38 to Fig 42 exhibit the characteristics of the GLCM texture features extracted from tumours of patients A to F respectively. The data used in plotting the graphs was obtained by finding the average tumour value from the individual patient A to F tumours extracted radiomic texture feature values. The

response or sensitivity of the tumours to radiotherapy treatment of all the patients in the cohort was being investigated. Un-normalised but comparable average data was used to plot the scatter plots and the standard deviation was inserted to show the uncertainty in the data.

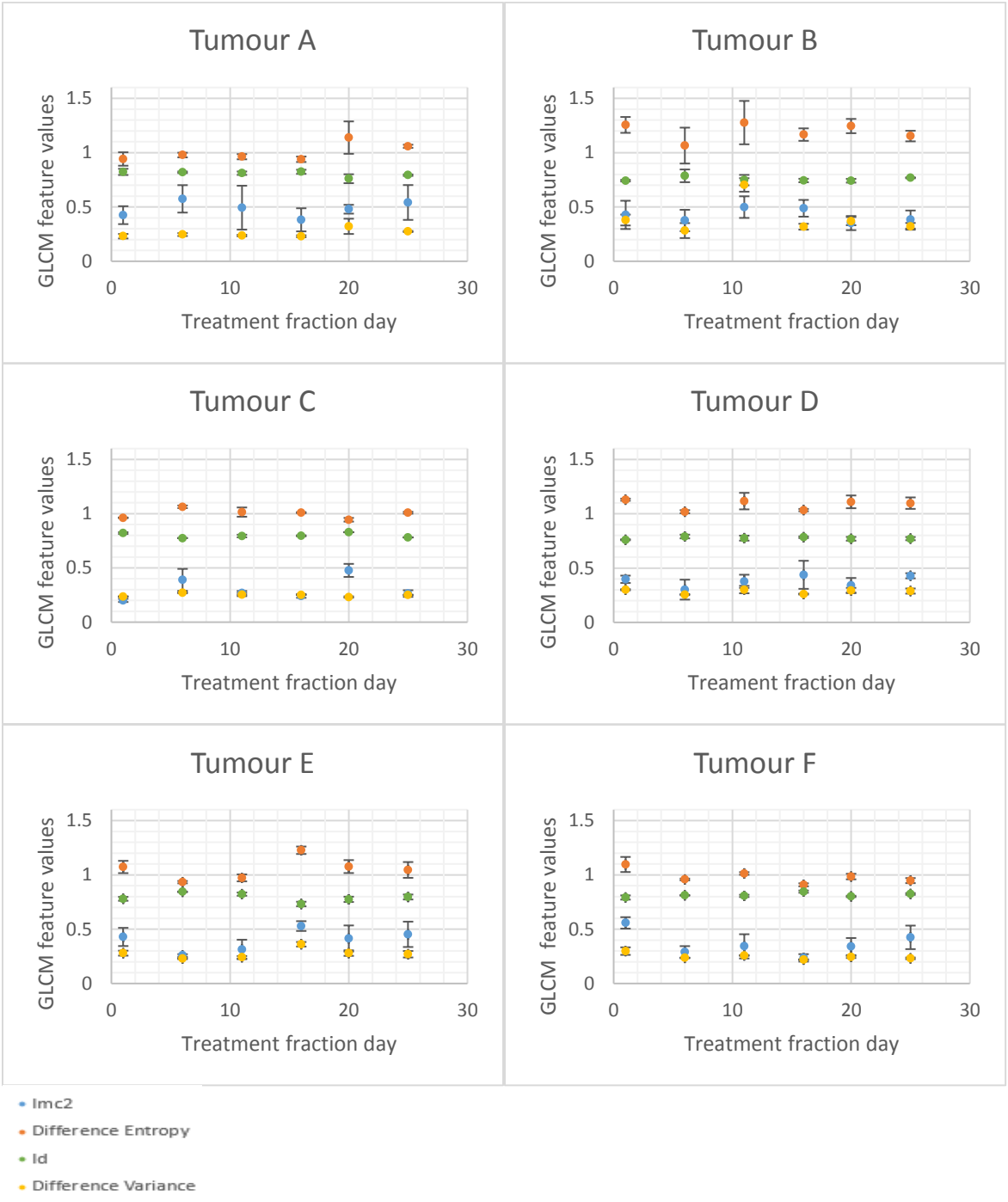

Fig 38. Graphical representation of selected GLCM robust radiomic features (e.g. difference entropy) and their behaviour during the radiotherapy treatment course of patients A to F. The graphs display the comparison of the tumours A to F, which was extracted from patients A to F respectively.

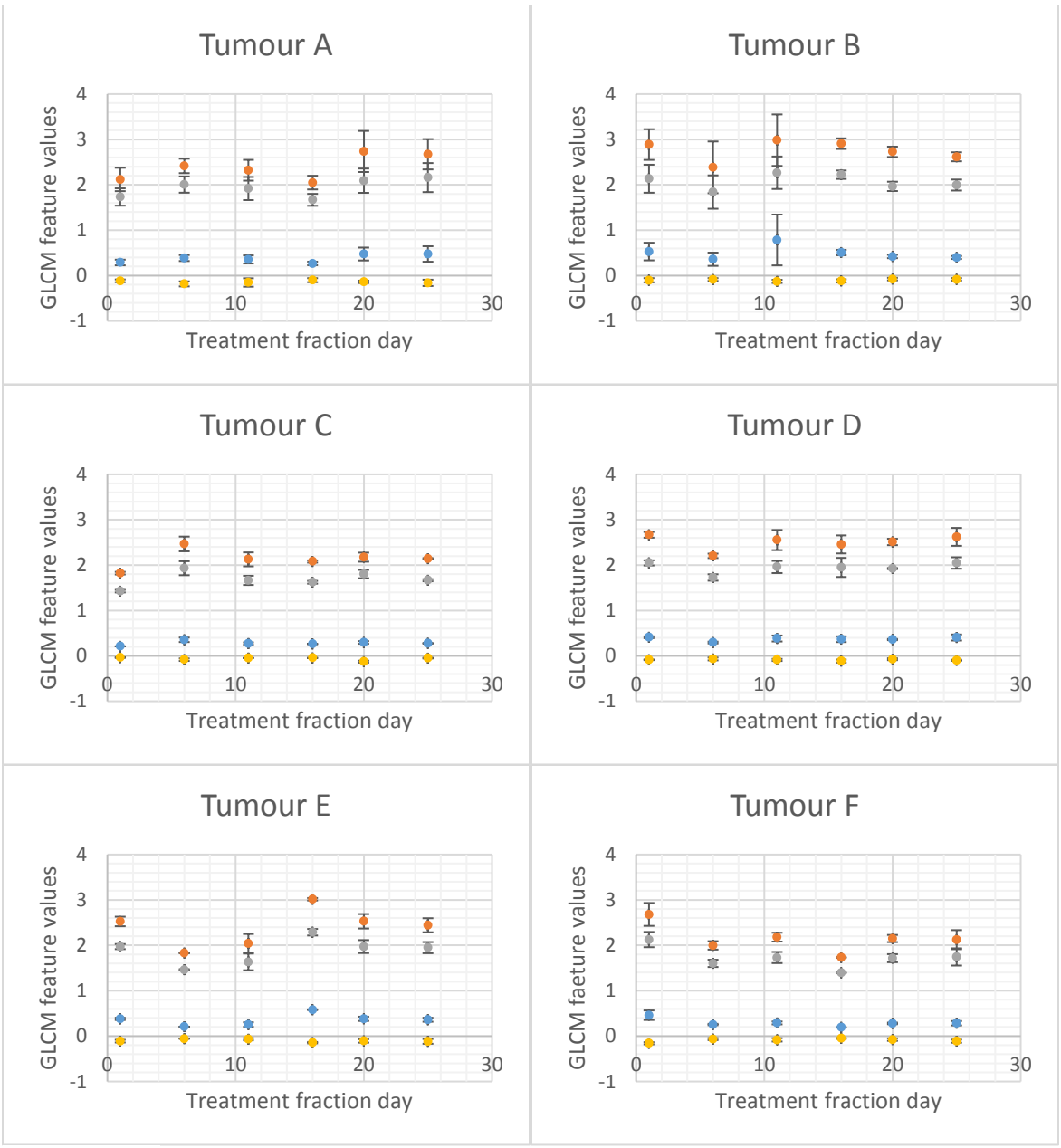

Fig 39. Graphical representation of the selected GLCM robust radiomic features (e.g. joint entropy) and their behaviour during the radiotherapy treatment course of patients A to F. The graphs allow comparison of the tumours A to F, which was extracted from patients A to F respectively.

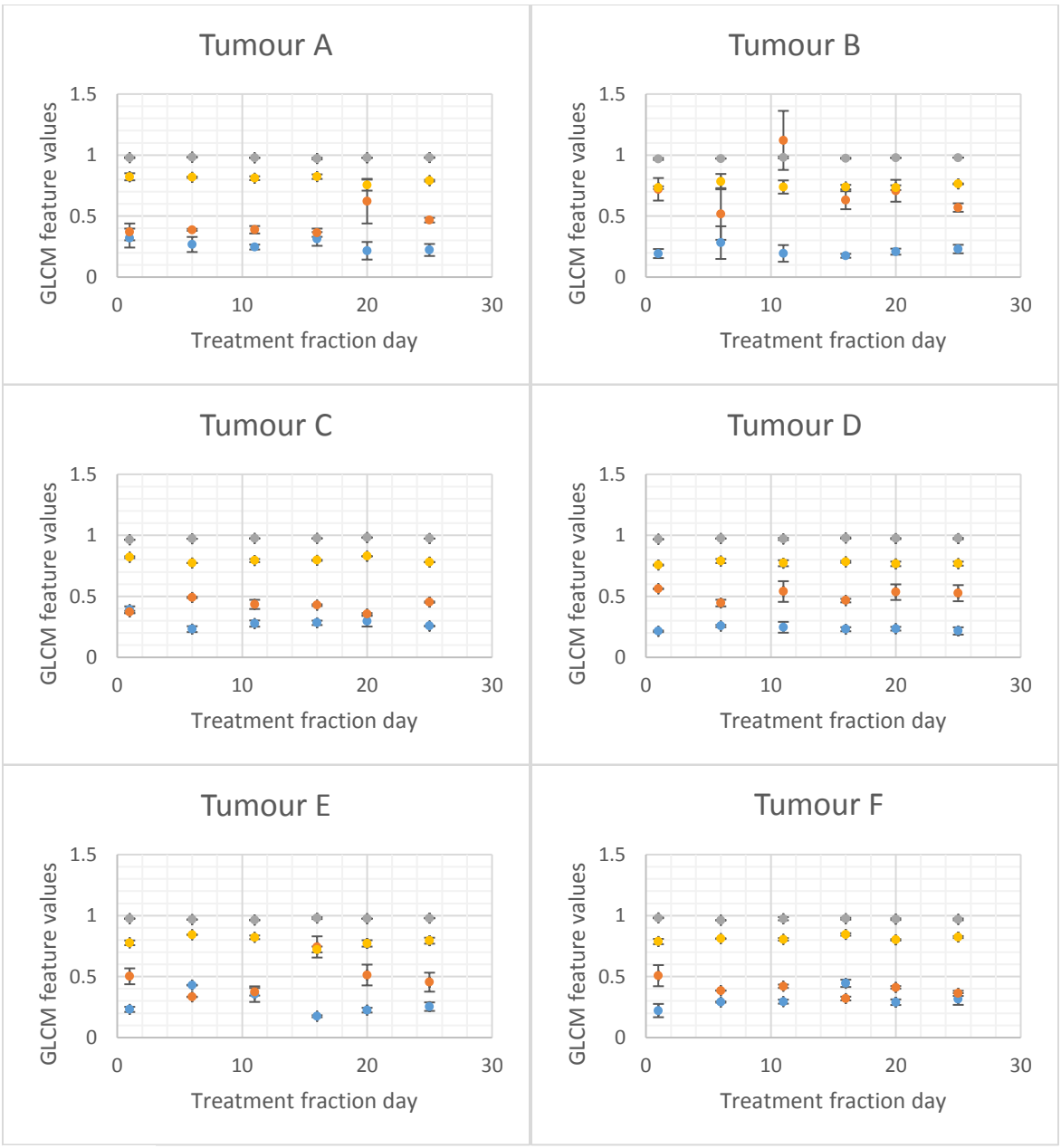

Fig 40. Graphical representation of the selected GLCM robust radiomic features (e.g. joint energy) and their behaviour during the radiotherapy treatment course of patients A to F. The graphs allow comparison of the tumours A to F, which was extracted from patients A to F respectively

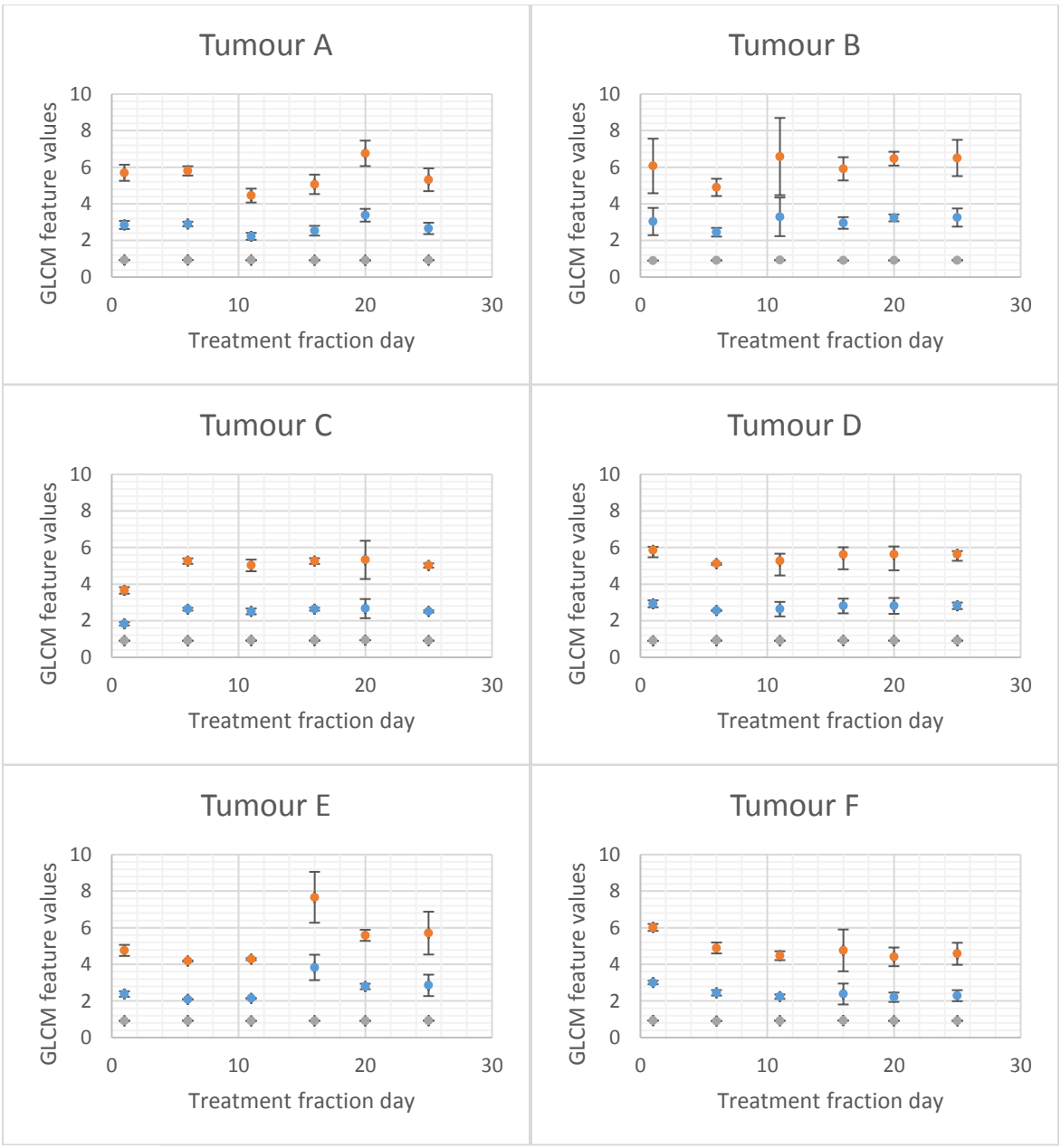

Fig 41. Graphical representation of the selected GLCM robust radiomic features and their behaviour during the radiotherapy treatment course of patients A to F. The graphs allow comparison of the tumours A to F, which was extracted from patients A to F respectively

Fig 42 displayed the patient tumour response to radiotherapy fractionated treatment. The 6 graphs were plotted using the average of the tumour texture features values normalised to the bladder texture features of this study

patient cohorts. The plotted feature values showed oscillating responses to the treatment fractions. The sinusoidal response of a tumour to treatment shows unequal peaks at different treatment fraction points. This means these features exhibits a personalised tumour sensitive to radiation treatment.

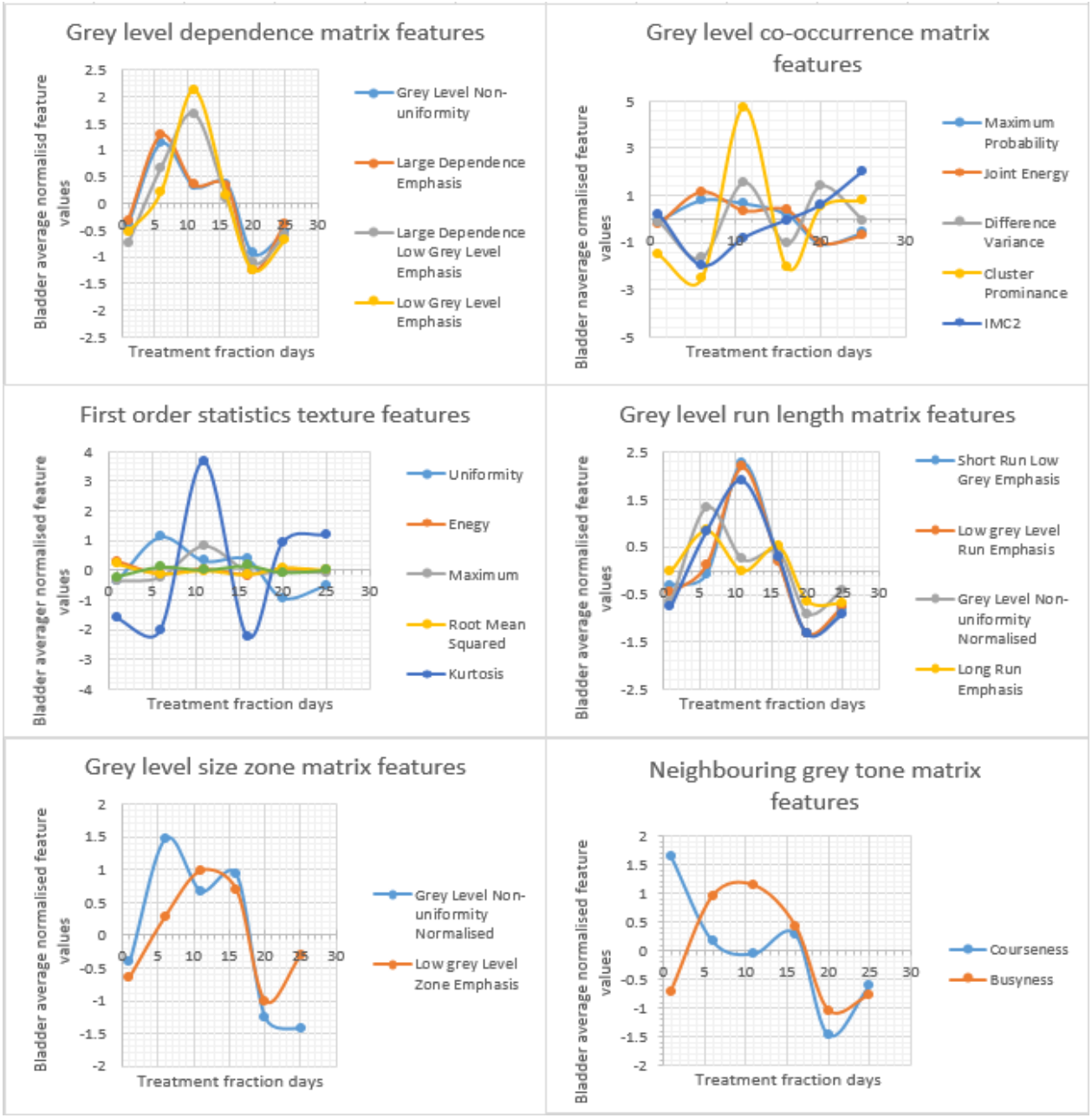

Fig 42. Graphical representation of the tumour average sensitivity to the radiotherapy fractionated treatment using texture features.

Table 13 presents the comparison of tumour variability within the patient cohort. The variability is represented by the coefficient of variance (COV) percentage between patient tumours. The COV% presented in *Table 13* was an average calculated from the treatment fraction COV% of each patient tumour data.

Table 13: Coefficient of variance (COV) in percentage (%) of GLCM radiomic features.

Patient Tumours	**A**	**B**	**C**	**D**	**E**	**F**
GLCM Features	**COV%**	**COV%**	**COV%**	**COV%**	**COV%**	**COV%**
Joint Average	8.8	17.0	6.5	9.8	8.8	10.6
Sum Average	8.8	17.0	6.5	9.8	8.8	10.6
Joint Entropy	10.8	9.8	3.6	5.3	4.7	5.4
Cluster Shade	5.5	191.2	-86.7	-178.8	-32.8	96.6
Maximum Probability	22.1	23.6	12.1	11.8	10.3	12.9
Idmn	0.4	0.4	0.1	0.5	0.3	0.7
Joint Energy	21.5	20.7	8.2	8.7	9.1	10.3
Contrast	11.9	17.4	2.9	8.4	11.2	5.7
Difference Entropy	4.7	7.1	1.5	3.4	4.2	2.5
Inverse Variance	9.3	7.2	2.5	5.4	6.7	4.8
Difference Variance	7.5	13.4	2.2	5.5	6.9	3.8
Idn	0.8	0.9	0.3	0.9	0.7	1.1
Idm	2.6	3.1	0.6	1.9	2.4	1.2
Correlation	25.4	38.6	16.0	23.8	25.3	21.5
Autocorrelation	17.2	33.4	12.8	19.3	17.2	20.3
Sum Entropy	11.5	9.7	4.1	5.2	5.3	6.1
Sum Squares	24.0	20.9	6.4	11.0	8.7	10.7
Cluster Prominence	57.8	45.8	21.7	33.1	22.0	38.3
Imc2	24.7	20.7	11.9	18.3	19.3	20.6
Imc1	-37.8	-33.5	-13.7	-24.8	-27.3	-30.6
Difference Average	10.3	11.4	2.4	6.9	8.9	5.3
Id	2.5	2.8	0.6	1.8	2.2	1.2
Cluster Tendency	30.5	26.1	8.9	14.7	13.2	14.7

Table 14 was created to show the variability of shape features through-out the whole study.

Table 14: Comparison of radiomic shape feature values within the patient cohort

Patient Tumours	**A**	**B**	**C**	**D**	**E**	**F**
Shape features						
Volume Number	1.0	1.0	1.0	1.0	1.0	1.0
Voxel Number	789.0	789.0	789.0	789.0	789.0	789.0
Maximum 3D Diameter	20.0	20.0	20.0	20.0	20.0	20.0
Maximum 2D Diameter Slice	20.0	20.0	20.0	20.0	20.0	20.0
Sphericity	0.9	0.9	0.9	0.9	0.9	0.9
Minor Axis	18.4	18.4	18.4	18.4	18.4	18.4
Elongation	1.0	1.0	1.0	1.0	1.0	1.0
Surface Volume Ratio	0.3	0.3	0.3	0.3	0.3	0.3
Volume	3945.0	3945.0	3945.0	3945.0	3945.0	3945.0
Major Axis	18.5	18.5	18.5	18.5	18.5	18.5
Surface Area	1373.0	1373.0	1373.0	1373.0	1373.0	1373.0
Flatness	0.8	0.8	0.8	0.8	0.8	0.8
Least Axis	15.6	15.6	15.6	15.6	15.6	15.6
Maximum 2D Diameter Column	18.9	18.9	18.9	18.9	18.9	18.9
Maximum 2D Diameter Row	20.0	20.0	20.0	20.0	20.0	20.0

Chapter 5: Discussion of findings

5.1 Discussion

In the previous chapter, the experimental results were presented in detail. The section below interprets the phantom study results and the patient study results. The phantom study discussion involved detailed analyses referring to the results plotted in Fig 18 to Fig 35. Fig 36 to Fig 37 which illustrated the effects of other image sampling parameters other than the CT image acquisition parameters on the radiomic features. The cervical cancer tumour data set results displayed in Fig 38 to Fig 42 were also included in this discussion section.

5.1.1 Phantom results discussion

The phantom results discussion section focussed on the interpretation of the results of the investigation of the dependence of radiomic texture features on the CT imaging parameters. The discussion also explained observations about the variability of radiomic features between scanners.

Fig 18 showed the tube current effects on image intensity histograms for the 10 cartridges of the CCR phantom acquired on the GE scanner. It was observed that the patient normalised feature difference values of the solid acrylic insert had greater feature values at low mAs as compared to the feature values at high mAs. This suggest that the radiomic features extracted from the solid acrylic insert were more dependent on tube current. The uniform structure of the solid acrylic insert did not give substantial texture information. Therefore, we assume the radiomic features variation observed in Fig 18 in relation to the solid acrylic insert were due to the mAs of acquisition increase or decrease. This might be associated to the image noise changes that were caused by a different number of photons reaching the CT detector as the mAs was changed. CT studies have demonstrated that there is a proportional relationship between image noise and variation in CT number values for a homogeneous area (Marwan Alshipli and Kabir, 2017; Monnin et al., 2017; Lalondrelle and Huddart, 2012).

The relationship between the mAs and the contrast resolution is complex. For increased mAs the image noise is expected to decrease in such a way that it enhances the image contrast. The enhanced contrast detail might therefore increase the ability to observe slight changes in the radiomic texture features. Dense cork and plaster resin materials displayed in Fig 18 demonstrated some relative dependence on the mAs variations at low mAs. The extent of mAs dependence observed for the dense cork and plaster resin materials inserts was low compared to the dependence of the solid acrylic material insert. All the other phantom inserts (rubber particles, natural cork and the 3 acrylonitrile butadiene styrene plastic) data plots showed smaller variations around the central axis (zero feature value) of the skewness, uniformity, entropy and kurtosis features graphs. Irrespective of the mAs changes, the radiomic texture feature values obtained from all of the ABS materials inserts, rubber particles and natural cork inserts were consistently smaller, closer to zero. The smaller dependence might have been caused by the nature of inserts. The natural cork, rubber particles and ABS materials were more textured materials. The impact of image noise due to mAs variation was significant on homogenous materials (solid acrylic, plaster resin inserts) as compared to more textured martials.

Fig 19 which consisted of 6 graphs. The graphs demonstrated the results of the relation between tube potential difference (kV) and the first order statistics radiomic features that were normalised using patient tumour data. The first order statistics features such as mean difference, uniformity and energy was observed to be dependent on the kV parameter. The kV dependence related to the type of the CCR phantom insert materials that was being analysed. The plaster resin, solid acrylic and rubber particles inserts illustrated a great kV dependence on low kVs. Except for the plaster resin, solid acrylic and rubber particles inserts, all the materials showed greater independence to changes of the kV of image acquisition. The kurtosis and energy features showed more robustness. It was observed from Fig 19 graphs that for most materials of the CCR phantom inserts, the kurtosis and energy feature values had values that approached zero, within ± 0.5 of the central axis (zero feature value). Except for skewness in the dense cork analysis, uniformity for solid acrylic and energy for the rubber particles analysis, all the texture features (kurtosis, energy, skewness, uniformity, mean and entropy) extracted exhibited gradual changes as the kV was varied from low to high kVs during the phantom acquisition. The texture feature values were within the range of 1 to -1.

When the kV was increased, the normalised feature difference values approach zero (either from positive or negative y-axis). Texture features that had their values closer to zero were more stable or robust and in this it happened at high kV. This might have been because at high kV the radiation attenuated signal detected at the CT detector was higher, reducing the noise effects. When the kV was increased the number of x-rays in the beam increased and the energy of the x-rays was also increased. More useful information was formed on the CT machine detector as compared to images acquired at low kV. Fundamentally there existed an indirect relationship between the kV and image noise, a complex direct relationship between kV and contrast detail. Considering the above analysis, it was observed that radiomic texture features extracted from materials with texture details such as the natural cork, sycamore wood and all the four ABS inserts follows the theoretical known trends and had normalised robust feature values that approached zero. The pattern observed in Fig 19 demonstrated the magnitude of the dependence of radiomic texture features was determined by the insert material from which the features were calculated. Also, the features dependence extent was influenced by the beam quality. In general, it was observed that the radiomic texture features were not absolutely independent of the kV but their dependence was a relative dependence.

Fig 20 displayed the relationship between first order statistics features and the change in slice thickness. As observed in the mAs and kV imaging parameters analysis, there existed some radiomic texture feature dependence on imaging parameters based on the material being analysed. Most of the cartridges show a great to moderate dependence on slice thickness at small slice thicknesses (< 2.5 mm). Less impact on the radiomic features was observed on features extracted from images obtained at bigger slice thickness (greater than 2.5 mm). This was assumed to be caused by the averaging effect (smoothing) on images acquired at large slice thicknesses. The smoothing effect influenced the images to have less image noise which might have been

accompanied by a reduced image detail. Thin slices reduce the number of transmitted photons in a region of interest, which lead to larger variations in pixel numbers and therefore increased image noise. To obtain the same noise level in a thin slice compared to a thick slice you need to increase the quantity of photons in the slice, i.e. increase mAs/kV/both. It is known theoretically that the square root of beam width (slice thickness) is inversely associated with image noise (Marwan Alshipli and Kabir, 2017; Monnin et al., 2017; Lalondrelle and Huddart, 2012). Therefore, the impact of large slice thickness on radiomic features was less dependent on the image noise, such that any changes noticed on the radiomic texture features might have been due to the nature of the material being analysed. Whereas the use of small slice thickness caused texture features to be more dependent because of increased image noise. Thin slices weakened robustness of texture features. Kurtosis, mean and skewness features displayed less variation when the slice thickness was changed from small to large. These texture features were robust and less dependent on slice thickness changes.

Fig 21 was plotted to ascertain the tumour data influence on the CCR phantom texture feature values. The average tumour texture feature values for a specific weekly fraction of a specific patient data set (patient A or B or C etc.) was used to normalise the phantom cartridge specific texture feature. It was observed in Fig 21 that there was no specific trend established on the plots due to the tumour fraction data. The trends established by kV effects (Fig 19) were more prominent. Variations established in the tumour texture features as a result of radiotherapy treatment progress did not seem to have a stronger influence on the phantom texture features. The acquisition parameters impact on the CCR phantom radiomic texture features was more significant than the influence tumour data. The tumour information used in the normalising process rather assisted in exhibiting the imaging parameter effects being investigated in relation to tumour variability.

Fig 21 to Fig 23 were plotted to investigate the effect of the patient tumour data on the ABS cartridges of the CCR phantom data obtained by changing the kV imaging parameter. The concepts discussed above for Fig 21 is the same as in Fig 22 and Fig 23 except that the phantom materials being discussed differ (Fig 21 uses CCR phantom insert 2, whilst Fig 22 and Fig 23 uses CCR phantom inserts 9 and 10). The graphs in Fig 22 and Fig 23 displayed a general decrease in the normalised feature values as the kV was changed from low (80kV) to high (140kV). It was observed that all the normalised texture feature values were very close to zero. This was because the material and structure of the acrylonitrile butadiene styrene plastic (ABS) from which the texture features were extracted. ABS had a honey comb shape with air spares that provided less attenuation to the CT photon beam, low or high energy beam. Theory points to an increase in the number of photons with high energy in the photon spectrum of the CT beam when the tube potential difference is changed from low to high. Noise in an image is caused by a low photon count on the CT detectors. ABS allowed most of the photons carrying the image detail to reach the CT detectors. The increase in kV reduced the noise detail on the images. The noise detail reduction was assumed to cause the decreasing trend in texture feature values as the kV was increased. The difference between texture feature values at 80kV and 140kV was very small because of the

material (ABS) from which the texture features were extracted. The ABS honey comb air spaces caused less attenuation to x-rays.

Heat maps in Fig 24 to Fig 26 represented the patient normalised CCR phantom radiomic texture features in four colours. These indicated the extent of the radiomic texture features dependence on the tube potential difference (kV). The study was interested in identifying radiomic texture features that were less dependent or completely independent of the CT imaging parameter that was being investigated. Texture features that displayed the colour green across all the 10 cartridge materials on the heat map table were ideally robust. These were the radiomic texture features that were within the limits $f_n < 0.5$, which resembled independence of the influence of CT acquisition parameter kV. Most normalised radiomic features that were extracted from inserts made of materials such as plaster resin, and solid acrylic were mainly dependent on the kV, they had values that were above 2.0 ($f_n > 2.0$). Rubber particles and sycamore wood exhibit a moderate number of features that were relatively dependent on the kV ($f_n > 0.5\ but < 1.0$). Highly homogenous material inserts (plaster resin, and solid acrylic) rendered most radiomic texture features weak. From that observation it was proposed that uniform material inserts did not have texture characteristics. The variations observed on the radiomic texture features obtained from uniform material inserts were influenced directly by the CT acquisition parameters. About 20 radiomic texture features of the 91 texture features extracted were less dependent on the kV ($f_n < 0.5$). Radiomic texture features extracted from materials natural cork, dense cork, sycamore wood and all the ABS inserts were relatively stable.

Heat maps in Fig 27 to Fig 32 represented the patient tumour data normalised CCR phantom texture features that depict the behaviour of the radiomic texture feature in relation to the mAs. Like heat maps displayed in Fig 24 to Fig 26, cells on the map that are coloured brown showed dependence upon the mAs. Regions that were coloured light green and yellow symbolise relatively independence to mAs. Texture features that showed green across all the 10 cartridge materials in the heat map table were considered robust. Most of the extracted radiomic texture features displayed a dependence on the mAs. The features exhibited brown coloured regions at low mAs (20 mAs, 50 mAs etc.) and the feature were green at high mAs (200 mAs and above). The trend was attributed to the decrease in the image noise from low mAs to high mAs. Increasing the mAs increases the x-ray quanta amount which had an effect of increasing the contrasts-to- noise ratio. High mAs result in improved image quality due to the decrease in image noise and increased signal-to-noise ratio. Low mAs reduces the photon quantity such that less number of x-rays reach the detector which cause less detail and more noise to be present in the image. Most features extracted from plaster resins and solid acrylic cartridges show that they dependent on mAs. Uniform materials seemed to promote measurement of the noise trend as the mAs was increased. Materials such as the natural cork, dense cork and sycamore wood that carry some texture in them had some radiomic features that were relatively dependent on the mAs change. There is greater dependence at low mAs and less dependence at higher mAs. Radiomic texture features were stable from 200

mAs and above because less variation in the texture feature values was observed. Image noise might have a greater impact on the stability of the radiomic texture features in that high noise variations causes high variations in the feature values.

Fig 30 to Fig 32 used the CCR phantom data obtained from the GE Electric CT unit and Fig 49 to Fig 50 used data obtained from the Toshiba Aquillion Large bore unit. The above mentioned heat maps showed the inter-machine relation between radiomic texture features obtained on different manufacturer CT units. It was observed that for approximately the same acquisition parameters the radiomic texture feature values were not the same. To relate the two sets of data is complex due to CT machines physical and mechanical parameter differences. Other studies that compared the image quality differences between CT machines, large bore (85 cm diameter) and normal bore (70 cm diameter) showed that the image quality parameters were not exactly the same but were comparable (Tomic et al., 2018; Mccann and Alasti, 2004; Garcia-Ramirez et al., 2002). In this study the radiomics texture features trends were comparable.

Heat maps in Fig 33 to Fig 35 represented the patient normalised CCR phantom radiomic texture features that indicate the extent of the features dependent on the slice thickness. Theory points to the averaging effect caused by increasing the slice thickness. Large slice thickness increase the number of transmitted photons in a region of interest, which lead to smaller variations in pixel numbers and therefore decreased image noise. Reducing noise should improve contrast. Small slice thickness causes the number of photons within each voxel to decrease, resulting in increased image noise. Thin slices improve spatial resolution and will introduce blur/loss of detail. Consider the GLCM radiomic features in Fig 33, the features maximum probability, joint energy, inverse difference, inverse variance and information measure correlation 1 and 2 were the robust features that did not get influenced by slice thickness changes. The GLDM had only the radiomic features: small dependence low grey level emphasis and low grey level emphasis that were entirely independent of the slice thickness changes as shown in Fig 33. Fig 34 had the first order statistics features; skewness, uniformity, kurtosis and mean that were robust and independent of the slice thickness manipulations of the experiment. These first-order statistics features were robust, their values were observed to be influenced by the distribution of pixel intensities with the ROI of enumeration. Only parameters that can affect the arrangement of the pixel intensities in the ROI can influence the features. The coarseness and contrast NGTM radiomic texture features were independent of the slice thickness as shown in Fig 35.

Table 4 showed an inverse relationship between the kV and image noise which agreed with observations from other studies that an increase in kV reduces CT image noise (Alsleem et al., 2013; Godoy et al., 2011; Funama et al., 2005). The investigations by Godoy et al. and Funama et al. suggested that low kV offers an increased SNR and CNR due to the prominent photoelectric interactions involved that enhances the image contrast. Thus, their observation suggest that image noise does not affect the image quality at low kV. Iodine contrast

injected was the cause. Though other studies that tested kV using different body parts observed that, low kV reduces the beam quality which increases the image noise, leading to reduction in image quality and diagnostic accuracy of CT images (Murakami et al., 2010; Seibert, 2004; Huda et al., 2000; Ertl-wagner et al., 1980).

Table 5 to *Table 6* did not provide clear trends of the relationship of the technique parameters (Slice thickness and mAs) against image noise. Zukhi et al.(Zukhi and Yusob, 2017) published a paper describing the effect of slice thickness on image noise. They concluded that small slice thickness are susceptible to high image noise whilst large slice thickness usually have a decreased image noise. *Table 5* did not follow the expected trend, rather some anomalies were exhibited. The image noise in *Table 6* generally decreased as the mAs was increased (from 150 mAs to 250 mAs) with anomaly points (300 mAs and 350mAs). It can be proposed that the changes in overall noise values obtained from the sampled ROIs when the slice thickness or mAs was changed depended on the texture pattern of the image inside the ROIs due to type of insert material (rubber particles) from which they were extracted.

The anomalies were observed to arise in instances where there was a change in spread of the grey level range within the matrix used to estimate the noise. For the same matrix size used, the greater the range of grey levels, the greater the noise. The image noise estimated represented a complex phenomenon of the influence it had on the image quality, the image quality in-turn is assumed to have effects on some radiomic features.

Table 8 shows the calculation results from the kV matrices examples displayed on the appendix *Table 15*, to *Table 18*. Almost all radiomic texture features in *Table 8* changed in value when the acquisition kV was changed. The magnitudes of the mean, energy and difference average features varied incrementally when the kV was changed from low to high kV values. Entropy, contrast, correlation and HX portrayed a reduced magnitude of the radiomic texture feature values as the kV was varied from low to high. The IMC1 and IMC2 features remained effectively constant with kV variation, these 2 features had a COV% that was less than 0.7%. On all the image matrices obtained from different inserts of the CCR phantom analysed for kV influence on features, 55.6% are consistently at less than 10% COV% and 44.4% of the features were above 10% COV%, see *Table 7* from wood insert data and *Table 8* from acrylic. The kV results imply there exist radiomic features that were reproducible and less susceptible to kV acquisition. This suggest that the choice of kV on radiomic signatures such as the variance, sum variance, difference variance, contrast, correlation and homogeneity could alter the prognostic value. The clear influence of the kV on the prognostic value of radiomic features has not yet been investigated and needs further research.

The results in *Table 9* displayed the variability with which co-occurrence matrix vary with slice thickness. About 33% of the features vary with more than 10% of standard deviation about the mean for each feature calculated manually. More than 66% of the features vary with less than 10% of the standard deviations about the mean

(coefficient of variance). As the slice thickness was increased the pixel intensities within an image vary less, the general trend expected would be a less variation at large slice thickness due to averaging of pixels.

As was shown in *Table 6* lower tube current was associated with high random noise. The random noise was known to cause a pixel by pixel intensity variability on the pixels that are supposed to carry the same grey scale density (grey scale information). The results in *Table 11* and *Table 12* supports the observation that, in general any parameter change on acquiring images for radiomics studies result in the values of the radiomic feature changing (Kim et al., 2019; Larue, van Timmeren, et al., 2017; Mackin et al., 2015). The results in *Table 11* and *Table 12* also reinforced the view that radiomic feature estimates performed from images obtained from 2 or more different CT machines shows some differences that ranges from marginal to significant (Midya, 2018; Larue, van Timmeren, et al., 2017; Fave et al., 2016).

The difference in feature values estimated using 250 mAs and 350 mAs was small for most of the features in *Table 11*. Big feature value differences are observed on the 400 mAs compared to either the feature values estimated from 350 mAs or 250 mAs images. This was attributed to the nature of the phantom insert material from which the image was obtained. Wood offers a broad Hounsfield Unit (HU) spread (approximately between -550 to -400 HU) within an image. A wide HU range within the ROI meant a broad range from the lowest pixel intensity to the highest pixel intensity for a specific mAs of image acquisition. A large range of the pixel intensity density within the ROI resulted in big size GLCM matrix being formed during feature calculation. Therefore, texture feature algorithms that involve the subtraction of pixel intensities within its equation (such as contrast, correlation, variance, sum and difference variance) produce large feature values as compared to feature values obtained from GLCM that are small.

Table 12 displayed that 22% of the GLCM feature values calculated to estimate the influence of mAs had a COV of above 10%. 78% of the GLCM feature values in *Table 12* had a COV% that is 10% and below. This means for the GE machine the mAs had a marginal effect on a greater number of the features presented in *Table 12*. Kim et al., and Yan et al., studies justified the use of below 10% COV as an appropriate measure of radiomic texture feature robustness.

The results in Fig 36 demonstrated that the values of 6 features that exhibited a gradual decrease as the ROI size was increased. The 7 features plotted in Fig 37 showed a steady increase in the texture feature values as the diameter of the ROI was increased. This meant that the features plotted (Fig 36 and Fig 37) showed that textural features were sensitive to the number of voxels in the ROI volume. Dercle L et al. in their study suggested the use of ROI that had more than 200 pixels to extract radiomic texture features (Dercle et al., 2017). The results in Fig 36 and Fig 37 showed that a variable ROI of data sampling has strong influence on the texture features. To exclude the influence of ROI size on texture features. This study used a fixed ROI for to extract all radiomic texture features.

In general radiomics texture features extracted from the same test phantom at approximately the same imaging parameters, conditions and imaged at different manufacturer CT units showed similar trends. The feature values obtained between different manufacturer units were never exact nor were they comparable. The process of normalising the values of specific features produced comparable patterns when the CT parameters (kV, mAs, or slice thickness) being varied were assessed.

5.1.2 Cervical cancer results discussion

The data samples used were from kV CBCT images acquired on the day of initial radiotherapy treatment and the subsequent following first day of the treatment week in the duration of the treatment. Strong observations were drawn from the patient data results as presented in the below paragraphs.

Fig 38 to Fig 41 illustrates the sensitivity or response of the individual cervical cancer tumours (A, B, C, D, E and F) to irradiation represented by a selected radiomic features (a mixture of relatively robust and not stable features). The patient data plots (A, B, C, D, E and F) are on the same Fig to compare sensitivities between different patients' tumour response to irradiation. A comparable set of GLCM radiomic features values was selected and plotted on the same set of axes. The average radiomic feature points plotted in the graphs had their corresponding uncertainty (standard deviation) bars plotted to show the effect of random errors within the radiomic texture data. Whilst Fig 42 also depicts the response to radiotherapy treatment, a selected number of radiomic features calculated from the tumours (A, B, C, D, E and F) average feature values normalized to the bladder average.

Information measure of correlation (Imc2), inverse difference (Id), difference entropy and difference variance features were illustrated in Fig 38. With the exception of the Id feature which estimated uniformity in an image, Imc2, difference entropy and difference variance features displayed voxel intensity level of disorderliness. It was observed that features Imc2, difference entropy and difference variance in Fig 38 followed similar patterns of tumour sensitivity during treatment. Id feature followed an inverse pattern to that of heterogeneity estimating features. Also, tumours A and C had similar trends of response to radiotherapy treatment whilst tumours B, D, E and F varied significantly with each other. Graphs in Fig 38 showed that generally the tumours were highly heterogeneous during the initial stages of the treatment. The heterogeneities slightly decreased as the treatment progressed. This was displayed clearly by difference entropy and difference variance features. Tumours B, D and F clearly displayed the observation, and some anomalies to the general trend were also observed.

Equation 35 represents the feature Imc2 and was used to estimate the mutual relationship between probability distribution i and j. An Imc2 estimation result of 0.0, would mean the distribution i and j were independent and result 1 would mean fully dependent and uniform distributions. From Imc2 in Fig 38, it was observed that the feature values Imc2 of all tumours A to F were between 0.2 and 0.5 with an average standard deviation 0.1. This showed that tumours A to F had complex texture characteristics that were not uniform.

Fig 39 displayed radiomic features sum squares, sum entropy, joint entropy and information correlation 1 (Imc1). The sum squares or variance, sum entropy and joint entropy features depicted the variability or randomness of the pixel intensity levels in the ROI. All these features measured the heterogeneity of the texture. All the other features shown in Fig 39 with the exception of Imc1, followed an identical trend in all tumours A to F along the treatment duration. The feature Imc1 represents heterogeneity in an image in the limits -1 and 0, thus presenting a flipped form of the trends observed for the sum squares, sum entropy and joint entropy features. It was determined in Fig 39 that tumours A and C had a comparable path of response to radiotherapy treatment whilst tumours B, D, E and F followed their own identical pattern. These tumour feature trend observations agreed with trends found in Fig 38.

The feature Imc1 in Fig 39 quantifies within the ROI the complexity of texture by assessing correlation between the probability distributions of i and j. The tumour environments A to F had very small and negative Imc1 feature values. The Imc1 feature values for tumour C ranged from -0.13 ± 0.02 to -0.03 ± 0.002 as was displayed in Fig 39. The magnitudes of the Imc1 feature values demonstrated tumours that had probability distributions of i and j that were highly complex. This might suggest that tumours A to F had some highly varying degrees of texture that were shown to have very weak correlations.

The energy feature shown in Fig 40 measured textural uniformity (depicting disorders in texture) in the ROI. It approximated the frequency of discrete voxel/pixel intensity value pairs existing in the neighbour within the tumour. Tumours A to F show a variation of energy feature values that ranged from 0.17 ± 0.01 to 0.44 ± 0.03 averages. The energy feature values displayed by these tumours were low on the 0 to 1 scale. A typical uniformity measure (energy feature) has a feature value maximum of 1 because the energy feature has a normalised range. Fig 40 displayed that the uniformity of the tumours changed during the course of radiotherapy treatment. The tumour response displayed by the energy feature shows that before treatment, tumour F had an energy feature value 0.22. Tumour F's energy feature value increased to 0.29 ± 0.01 in weeks 2 and 3, week 4 the feature value was estimated to be 0.44 ± 0.03 and then it decreased to 0.29 ± 0.02 and 0.32 ± 0.04 in the 5th and 6th treatment weeks respectively. An unstable relative increase in the uniformity is therefore established by this observation. The trends of the energy feature as well as all other features plotted in Fig 38 to Fig 41 were unique to each tumour.

The contrast feature plotted on the same axes as the energy feature in Fig 40 displayed feature values that were larger than the energy feature values. The contrast feature measures the spatial frequency of a contiguous voxels/pixels in an image. The values of the contrast features for tumours B, D and E were mostly above the 0.5 feature value on a 0 to 1 scale. The contrast features of all the patients in this study were larger than the energy feature values. This implies the contrast feature values observation agreed with the energy feature value results analysis that tumours A to F were not uniform and had complex texture patterns. Tumours A to F

contrast feature trends displayed in Fig 40 showed trends that were a flip figure to that of the energy feature. At a treatment point where the energy feature value was high, the contrast feature values was low and vice versa. The trends also displayed the tumours heterogeneities that had weak and unstable slight decreases along the duration of treatment.

Also plotted on Fig 40 were, the texture features inverse difference moment (Idm) and inverse difference moment normalised (Idmn). Both feature measures image local homogeneity. Idm assumes larger values for smaller grey tone differences in pair elements. Idmn differ from Idm in that Idmn normalises the square of the difference between neighbouring intensity values by dividing over the square of the total number of discrete intensity values. The homogeneity features are more sensitive to the presence of near diagonal elements in the GLCM. Idm has maximum value when all elements in the image are same. GLCM contrast and homogeneity are strongly, but inversely, correlated in terms of equivalent distribution in the pixel pairs population. It means homogeneity decreases if contrast increases while energy is kept constant. In this study Idm had values that are between 0.72 ± 0.02 and 0.85 ± 0.01.

Fig 41 illustrated the behaviour of texture features joint average, sum average and Id along the treatment period. The joint and sum average features estimate the mean intensity level in the image. The joint and sum average features displayed in Fig 41 can be classified in the category of features that describe the randomness/disorderliness of texture in images. It was observed that joint and sum average features took the same shape/trends that entropy features, contrast, variance feature and Imc2 feature followed. Tumours D and F shown in Fig 41 showed a gradual decrease of the joint average and sum average features from the start of treatment to the subsequent treatment weeks.

In general tumours are known to be heterogeneous in nature and the heterogeneity of tumours vary from one tumour (e.g. tumour A differed from tumour B etc.) to another in the same patient or between patients. A radio-genomics article by van Timmeren et al. (van Timmeren et al., 2017) demonstrated that across metastatic tumour sites within a single patient, the tumours genomic heterogeneity could be the major cause of radiotherapy treatment resistance and therefore leading to treatment failure. The tumour texture variability was explored because the variability measure assists in understanding the tumour heterogeneity and its effects on tumour response to radiotherapy treatment. In this study, a relative gradual decrease of tumour heterogeneity along treatment time was observed. This suggested better tumour treatment response. The phenomenon was observed clearly on tumours D and F through the cervical tumour study.

Table 14 displayed the results of the shape features extracted in the clinical data set. Identical spherical shape ROIs of the same size placed at different positions in the tumour were used. These ROIs produced identical shape features as illustrated by the same values between tumours. In the phantom study when the CT acquisition parameters were varied only the slice thickness affected the number of voxels in the ROI. Slice

thickness and FOV affects the width of voxels in such that the number of voxels changes from one image to the other. In the patient part of this study, an identical imaging protocol was employed. Therefore, it is presumed that the observations made regarding the cervical cancer results relied mainly on the tumour biological response to treatment.

The evolution of cancerous cells in a tumour is not the same in all tumours even in the same patient. Individual tumours undergo cloning from the initial cancerous cell to fast-growing cancerous cells that respond variably to the environment in which they are growing. Differential mutations (sub-clonal and clonal) bring about spatial heterogeneity among different tumours in patients (Bozic et al., 2016). Tumours respond differently to treatment, some will be resistant to radiotherapy treatment. Other tumours will be sensitive enough to be eradicated by the treatment (Jarosz-Biej et al., 2019; Rockwell et al., 2010). Variable radiation treatment response was expected due to the different micro or macroscopic structure, biochemistry and gene expression within the malignant tumours of this study. The manner with which the tumours (A, B, C, D, E and F) responded to fractionated radiotherapy treatment was a complex matter. The trends of the texture features displayed by Fig 38 to Fig 41 was patient specific. As was deduced from Fig 38 to Fig 41 some similarities in trends between tumours texture features response to radiation treatment existed. In this study tumours A and C radiomic texture features had comparable paths of response to radiotherapy treatment whilst tumours B, D, E and F followed their own identical patterns.

There exist at least four 'time factors' that make up the cell cycle. The 'time factors' influence tumours and normal tissues response to fractionated irradiation (Withers, 1975). For standard radiotherapy treatments, for example cervical cancer treatment, cell death and cell recovery are affected by the reoxygenation, repair, repopulation and redistribution processes of the irradiated cells. The cell repair and redistribution take place over relatively shorter time intervals in the cell cycle. Studies have observed that it is most probable that the repair and redistribution processes approximately end by the end of the therapy daily fractionation intervals (Schattler and Ledzewicz, 2015; Gasinska et al., 2009). Contrary to the repair and redistribution 'time factor' processes, the reoxygenation and repopulation happen over more prolonged times. Because the reoxygenation and repopulation are affected by several factors that include the position and environment in which the tumour is situated and the variation in treatment schedules from 1 patient to another. Large time differences between treatments affects the repopulation process, short time intervals between fractions is considered effective in tumour eradication (Gasinska et al., 2009; Withers, 1975). As a result there were less chances for the robust radiomic features extracted between tumours of this study to have the exact feature values at each treatment fraction day between patients. The patterns with which the robust features increased or decreased during the duration of radiotherapy treatment could have been similar between tumours, or be completely different as observed in these study results.

Chapter 6: Conclusion

6.1 **Conclusion and final considerations**

The aim of the study was to identify radiomic features that are not dependent on the CT scan parameters (mAs, kV and slice thickness) using a phantom study and mathematical equation estimations. The results were in agreement with the studies performed by Mackin et al., Larue et al. and Shafiq-ul-Hassan (Mackin et al., 2018; Shafiq-ul-Hassan et al., 2018; Ruben T H M Larue et al., 2017) that tested the impact of exposure parameters and other image characteristics such as the discretisation of the grey level. The exposure parameters investigated influenced most of the radiomic texture features that was examined. There exist some radiomic features such as the first order statistics' kurtosis, skewness, uniformity, total energy and entropy that were deduced to be less dependent on the mAs, kV and slice thickness parameters. GLCM texture features energy, inverse variance, inverse difference moments, maximum probability, homogeneity, Imc1, Imc2 and entropy were also less influenced by the mAs, kV and slice thickness changes. It can thus be concluded that the texture features described the randomness or orderliness with which the voxel/pixel intensities changed within the ROI of analysis when the mAs, kV and slice thickness was changed hence they were less influenced.

Changes to the exposure parameters, mAs, kV and slice thickness, influenced the image noise and pixel intensity values. It was observed and concluded that the systematic variation in image noise within a ROI had less or no influence on the texture patterns. Radiomic texture feature algorithms that estimated feature values based on the texture arrangements within the ROI had less dependence on changes caused by noise. On repeated estimations the features demonstrated COV $\leq 10\%$ to their values across a changed parameter (e.g. mAs) whilst the other parameters were kept constant.

It was established that when the kV was increased, the normalised feature difference values approach zero (either from positive or negative y-axis). The use of high kV (100 kV and above) considerably increased robustness of texture features. When the kV was increased the x-ray quantity in the beam increased and the quality of the x-rays also increased. This demonstrated that at high kV the radiation attenuated signal detected at the CT detector was higher reducing noise effects in the image. The effect of noise reduction as result of increased kV is an improved the signal-to-noise ratio (SNR). The image contrast is adversely affected by the increase in kV but this is largely over-compensated by the associated decrease in noise. Therefore use of higher kV the better the contrast-to-noise ratio (CNR). It was therefore deduced that textures features become more stable at higher kV (100 kV and above). More useful information on images was formed on the CT machine detector as compared to images acquired at low kV.

The study demonstrated that there exist an indirect relationship between the kV and image noise, a complex direct relationship between kV and CNR detail. In theory CT images are substantially affected by kV increase in that higher kVs produces better CNR due to decrease in noise(Nagel, 2007). It was established that radiomic

texture features extracted from materials with texture details such as the natural cork, sycamore wood and all the four ABS inserts had normalised robust feature values that approached zero. It was deduce that the texture feature magnitude of dependence on kV was influenced by the material of the phantom insert from which they were extracted. Textured materials produced considerably stable radiomic texture features when compared to homogenous materials.

All the shape features were robust, they were minimally and in most cases not at all influenced by image quality changes that result from CT acquisition parameter changes. The reason being identical ROIs were used for the phantom and cervical cancer part of this study.

There has been an increased volume of published articles that present evidence of the potential of correlating tumour texture and the treatment outcome. Panth et al. found that 'the feature value for slow-growing tumours (gene-induced) was higher than for faster-growing tumours (no gene-induced group) upon combination with radiotherapy'. They concluded that there is a relationship between the genetic tumour changes and early effects of radiation treatment (Panth et al., 2015). In this study, it was shown that robust radiomic features could be used to investigate the impact of radiotherapy treatment. By applying the quantitative radiomics algorithms on the weekly fraction CBCT images obtained during radiotherapy treatment. Tumour radiation-induced changes was observed through texture feature changes along treatment period. The trends of the texture features, entropy, Id, Idm, Idmn and energy extracted from the cervical cancer tumour environments was patient specific. In this study tumours A and C had similar path of response to radiotherapy treatment whilst tumours B, D, E and F followed their own specific (individual) pattern. The treatment outcome could not be conclusively deduced as patient follow-up information was not available. Never the less the clinical implication of this study was achieved. Radiomics texture features that were less dependent on the CT acquisition parameters in textured inserts of the CCR phantom were used to show changes in tumour heterogeneity. This fulfilled the objective of this study that identified robust radiomic texture features be use on a clinical data set.

The impact of this radiomic texture study established the tumours heterogeneity varied between them. This agreed with clinical studies that showed that tumours exhibit some extensive genetic and phenotypic variations. The use of texture features, such as contrast and entropy, which exhibited stability to CT exposure parameters to estimate tumour heterogeneity was a major success in this study. The methods used in this study were based on image information obtained through non-invasive and retrospective means. The non-invasive approach reduces the risks that can be caused by surgery and biopsy methods in extracting information from patients. The use of retrospective data (cervical cancer CBCT images data set) was convenient and did not add any radiation dose to patients.

This means the aim of the study was fulfilled in that the influence of CT acquisition parameters was determined. The first objective was also fulfilled in that radiomics texture features that were less dependent on CT technique parameters were identified. Also the results from the GE and Toshiba machines showed similar trends of the CT technique parameter influence on radiomic texture features. Thus the inter-scanner variability of texture features between CT scanners was comparable.

6.2 Limitations and Recommendations

The use of a phantom provided limitations in that the constituent materials did not perfectly substitute for human tissue. This might create further challenges in that some features that appear to be robust might not fit the human tissue feature value distributions. Many radiomic features in this study showed great dependence on the imaging parameters on a different scale depending on the phantom insert material. The experimental phantom study results suggest that materials used in constructing radiomics phantoms might have influence on the changes that radiomic texture features might present during investigations. The use of radiomic phantoms that would have suitable inserts with similar properties to human tissues is suggested. This might contribute further to the understanding of radiomics studies from a human tissue texture point of view.

Further tests that include both radiomic biomarkers and sophisticated genomic analyses need to be performed. This might help in identifying standard radiomic texture features that relate to a particular biological change. To predict disease prognosis, treatment outcomes, survival rate or even recurrences, radiomics classifiers would need to be compared to known existing prognostic factors to identify correlations.

This study has established that any change in the size of ROI used to sample radiomic feature data resulted in gradual changes in the radiomic feature values. Size of ROI has influence on the radiomic feature values. It is recommended that caution be exercised in interpreting non-shape features if or when studies use variable size ROIs due to tumour size change during radiotherapy treatment.

The cervical cancer patient data used in this study were limited. No information about follow-up of the radiotherapy treatment was available for patients. If patient CT images taken during follow-ups after the treatment completion was available, further inferences from the radiomic features about the treatment outcome could have been established. The clinical significance of radiomic feature studies should be tested further in various clinical situations.

The tumour histology data of the patient cohort investigated was not available. In future, such information should be sourced so as to test radiomic feature variations against the tumour histology.

REFERENCES

Aggarwal, N. and K. Agrawal, R. (2012) 'First and Second Order Statistics Features for Classification of Magnetic Resonance Brain Images', *Journal of Signal and Information Processing*, vol. 03, no. 02, pp. 146–153 [Online]. DOI: 10.4236/jsip.2012.32019.

Alobaidli, S., Mcquaid, S., South, C., Prakash, V., Evans, P. and Nisbet, A. (2014) 'The role of texture analysis in imaging as an outcome predictor and potential tool in radiotherapy treatment planning', *Br J Radiol*, no. May, pp. 5–14 [Online]. DOI: 10.1259/bjr.20140369.

Alshipli, M and Kabir, N. . (2017) 'Effect of slice thickness on image noise and diagnostic content of single-source-dual energy computed tomography Effect of slice thickness on image noise and diagnostic content of single-source-dual energy computed tomography', *IOP Conf. Series: Journal of Physics: Conf. Series*, vol. 851, no. 012005, pp. 1–7.

Alshipli, Marwan and Kabir, N. A. (2017) 'Effect of slice thickness on image noise and diagnostic content of single-source-dual energy computed tomography Effect of slice thickness on image noise and diagnostic content of single-source-dual energy computed tomography', *IOP Conf. Series: Journal of Physics*, vol. Series 851, no. 851 012005, pp. 1–6.

Alsleem, H., Davidson, R. and Mi, M. (2013) 'Factors Affecting Contrast-Detail Performance in Computed Tomography : A Review', *Journal of Medical Imaging and Radiation Sciences*, Elsevier Inc, vol. 44, no. 2, pp. 62–70 [Online]. DOI: 10.1016/j.jmir.2012.12.001.

Balvay, D., Perre, S. Vande, Bouchouicha, A., Savatovsky, J., Sadik, J., Thomassin-naggara, I., Fournier, L. and Id, A. L. (2019) 'Gray-level discretization impacts reproducible MRI radiomics texture features', *PLoS ONE*, vol. 14, no. 3, pp. 1–14.

Beckers, R. C. J., Lambregts, D. M. J., Schnerr, R. S., Maas, M., Rao, S. X., Kessels, A. G. H., Thywissen, T., Beets, G. L., Trebeschi, S., Houwers, J. B., Dejong, C. H., Verhoef, C. and Beets-Tan, R. G. H. (2017) 'Whole liver CT texture analysis to predict the development of colorectal liver metastases—A multicentre study', *European Journal of Radiology*, Elsevier, vol. 92, no. February, pp. 64–71 [Online]. DOI: 10.1016/j.ejrad.2017.04.019.

Bodalal, Z., Trebeschi, S. and Beets-tan, R. (2018) 'Radiomics : a critical step towards integrated healthcare', Insights into Imaging, pp. 911–914.

Bozic, I., Gerold, J. M. and Nowak, M. A. (2016) 'Quantifying Clonal and Subclonal Passenger Mutations in Cancer Evolution', *PLoS Comput Biol*, vol. 12, no. 2, pp. 1–19 [Online]. DOI: 10.1371/journal.pcbi.1004731.

Brooks, F. J. and Grigsby, P. W. (2014) 'The Effect of Small Tumor Volumes on Studies of Intratumoral Heterogeneity of Tracer Uptake', *The Journal of Nuclear Medicine*, vol. 55, no. 1, pp. 37–43 [Online]. DOI: 10.2967/jnumed.112.116715.

Bushberg, J. T., Seibert, A. J., Leidholdt, E. M. and Boone, J. M. (2002) 'Bushberg-The Essential Physics of Medical Imaging_2ed.pdf', Lippincott williams and wilkins company.

Byrd, D., Byrd, D., Bowen, S. R. and Sandison, G. A. (2015) 'Quantitative radiomics : impact of stochastic effects on textural feature analysis implies the need for standards', no. October [Online]. DOI: 10.1117/1.JMI.2.4.041002.

Castellano, G., Bonilha, L., Li, L. M. and Cendes, F. (2004) 'Texture analysis of medical images', *Clinical Radiology*, vol. 59, no. 12, pp. 1061–1069 [Online]. DOI: 10.1016/j.crad.2004.07.008.

Chityala, R., Hoffmann, K. R., Rudin, S., Bednarek, D. R., Street, M., Street, M., Street, M., Stroke, T., Street, M. and County, E. (2011) 'HHS Public Access', vol. 5745, no. 1, pp. 583–590 [Online]. DOI: 10.1117/12.595430.Region.

Cohen, F. and Cooper, D. (1984) 'Simple parallel hierarchical and relaxation algorithms for segmenting noncausausal markovian random fields, technical Report LEMS-7 July 1984', *Technical Report LEMS*.

Dercle, L., Ammari, S., Bateson, M., Durand, P. B., Haspinger, E., Massard, C., Jaudet, C., Varga, A., Deutsch, E., Soria, J. and Ferté, C. (2017) 'Limits of radiomic-based entropy as a surrogate of tumor heterogeneity : ROI-area , acquisition protocol and tissue site exert substantial influence', *Scientific Reports*, no. July, pp. 1–10 [Online]. DOI: 10.1038/s41598-017-08310-5.

Ertl-wagner, B. B., Hoffmann, R., Bruning, R., Herrmann, K., Snyder, B., Blume, J. D. and Reiser, M. F. (1980) 'Radiology Multi – Detector Row CT Angiography of the Brain at Various Kilovoltage Settings 1', no. 9.

Fave, X. (2015) 'Preliminary investigation into sources of uncertainty in quantitative imaging features.pdf', Computerized medical imaging and graphics: the official journal of the Computerized Medical Imaging Society 44.

Fletcher, J. G., Leng, S., Yu, L. and McCollough, C. H. (2016) 'Dealing with Uncertainty in CT Images.',

Radiology, vol. 279, no. 1, pp. 5–10 [Online]. DOI: 10.1148/radiol.2016152771.

Flores, L., Vidal, V. and Verdú, G. (2015) 'System matrix analysis for computed tomography imaging', *PLoS ONE*, vol. 10, no. 11, pp. 1–12 [Online]. DOI: 10.1371/journal.pone.0143202.

Ford, J. M. and Decker, S. J. (2016) 'Journal of Forensic Radiology and Imaging Computed tomography slice thickness and its effects on three-dimensional reconstruction of anatomical structures', *Journal of Forensic Radiology and Imaging*, Elsevier, vol. 4, pp. 43–46 [Online]. DOI: 10.1016/j.jofri.2015.10.004.

Funama, Y., Nakayama, Y., Kakei, K., Nagasue, N., Shimamura, M., Morishita, S. and Yamashita, Y. (2005) 'Radiology without Degradation of Low-Contrast Detectability at Abdominal Multisection CT with a Low – Tube Voltage Technique : Phantom Study 1', no. 8, pp. 905–910.

Garcia-Ramirez, J. L., Mutic, S., Dempsey, J. F., Low, D. A. and Purdy, J. A. (2002) 'Performance evaluation of an 85-cm-bore x-ray computed tomography scanner designed for radiation oncology and comparison with current diagnostic CT scanners', *Int. J. Radiation Oncology Biol. Phys*, vol. 52, no. 4, pp. 1123–1131.

Gasinska, A., Fowler, J. F., Lind, B. K. and Urbanski, K. (2009) 'Influence of overall treatment time and radiobiological parameters on biologically effective doses in cervical cancer patients treated with radiation therapy alone Influence of Overall Treatment Time and Radiobiological Parameters on Biologically Effectiv', *Acta Oncologica*, vol. 43, no. 7, pp. 657–666 [Online]. DOI: 10.1080/02841860410018511.

Geyer, L. L., Schoepf, U. J., Meinel, F. G., Nance, J. W., Bastarrika, G., Leipsic, J. A., Paul, N. S., Rengo, M., Laghi, A. and De Cecco, C. N. (2015) 'State of the Art: Iterative CT Reconstruction Techniques', *Radiology*, vol. 276, no. 2, pp. 339–357 [Online]. DOI: 10.1148/radiol.2015132766.

Gillies, R. (2012) 'Radiomics : Extracting more information from medical images using advanced feature analysis Radiomics : Extracting more information from medical images using advanced feature analysis', *European journal of cancer*, Elsevier Ltd, no. March [Online]. DOI: 10.1016/j.ejca.2011.11.036.

Godoy, M. C. B., Heller, S. L., Naidich, D. P., Assadourian, B., Leidecker, C., Schmidt, B. and Vlahos, I. (2011) 'Dual-energy MDCT : Comparison of pulmonary artery enhancement on dedicated CT pulmonary angiography , routine and low contrast volume studies', vol. 79, pp. 11–17 [Online]. DOI: 10.1016/j.ejrad.2009.12.030.

Goldman, L. W. (2007) 'Principles of CT : Radiation Dose and Image Quality *', *Journal of Nuclear Medicine Technology*, vol. 35, no. 4, pp. 213–226 [Online]. DOI: 10.2967/jnmt.106.037846.

Goldman, L. W. (2008) 'Principles of CT: Multislice CT', *Journal of Nuclear Medicine Technology*, vol. 36, no. 2, pp. 57–68 [Online]. DOI: 10.2967/jnmt.107.044826.

van Griethuysen, Joost J M, Fedorov, A., Parmar, C., Hosny, A., Aucoin, N., Beets-tan, R. G. H., Pieper, S. and Aerts, H. J. W. L. (2017) 'Supplementary material', *Supplementary material*.

van Griethuysen, J. J. M., Fedorov, A., Parmar, C., Hosny, A., Aucoin, N., Narayan, V., Beets-Tan, R. G. H., Fillon-Robin, J. C., Pieper, S. and Aerts, H. J. W. L. (2017) 'Computational Radiomics System to Decode the Radiographic Phenotype. Cancer Research', *Cancer Research*, vol. 77(21), pp. e104–e107.

van Griethuysen, Joost J M, Fedorov, A., Parmar, C., Hosny, A., Aucoin, N., Narayan, V., Beets-tan, R. G. H., Pieper, S. and Aerts, H. J. W. L. (2017) 'Computational Radiomics System to Decode the Radiographic Phenotype', *Cancer Research*, vol. 77, no. 21, pp. 104–108 [Online]. DOI: 10.1158/0008-5472.CAN-17-0339.

Haralick, R. M., Shanmugam, K. and Dinstein, I. (1973) 'Textural Features for Image Classification', *IEEE Transactions on Systems, Man, and Cybernetics*, vol. SMC-3, no. 6, pp. 610–621 [Online]. DOI: 10.1109/TSMC.1973.4309314.

He, L., Huang, Y., Ma, Z., Liang, Cuishan, Liang, Changhong and Liu, Z. (2016) 'Effects of contrast-enhancement, reconstruction slice thickness and convolution kernel on the diagnostic performance of radiomics signature in solitary pulmonary nodule', *Scientific Reports*, Nature Publishing Group, vol. 6, no. 1, p. 34921 [Online]. DOI: 10.1038/srep34921.

Hoogeman, M., Chai, X. and Herk, M. Van (2017) 'Bladder filling variation during conformal radiotherapy for rectal cancer Bladder filling variation during conformal radiotherapy for rectal cancer', *Journal of Physics: Conference Series*, vol. 851, pp. 1–7.

Huda, W., Scalzetti, E. M. and Levin, G. (2000) 'Technique Factors and Image Quality as Functions of Patient Weight at Abdominal CT 1',.

Huynh, E., Coroller, T. P., Narayan, V., Agrawal, V., Hou, Y., Romano, J., Franco, I., Mak, R. H. and Aerts, H. J. W. L. (2016) 'CT-based radiomic analysis of stereotactic body radiation therapy patients with lung cancer', *Radiotherapy and Oncology* [Online]. DOI: 10.1016/j.radonc.2016.05.024.

Incoronato, M., Aiello, M., Infante, T., Cavaliere, C., Grimaldi, A. M., Mirabelli, P., Monti, S. and Salvatore, M. (2017) 'Radiogenomic Analysis of Oncological Data : A Technical Survey', pp. 1–28 [Online]. DOI: 10.3390/ijms18040805.

Jarosz-Biej, M., Smolarczyk, R., Cicho ´n, T. and Kułach, N. (2019) 'Tumor Microenvironment as A " Game Changer " in Cancer Radiotherapy', *International Journal of Molecular Sciences*, vol. 20, no. 3212, pp. 1–19.

Jennings, D., Fennessy, F., Sonka, M. and Buatti, J. (2012) '3D Slicer as an Image Computing Platform for the Quantitative Imaging Network', *Magnetic Resonance Imaging*, vol. 30, no. 9, pp. 1323–1341 [Online]. DOI: 10.1016/j.mri.2012.05.001.3D.

Katkar, R., Steffy, D. D., Noujeim, M., Deahl, T. and Geha, H. (2016) 'The effect of mA, number of basis images and export slice thickness on contrast-to- noise ratio and detection of mandibular canal on cone beam computed tomography scans: an in vitro study', *Oral Surgery, Oral Medicine, Oral Pathology and Oral Radiology*, Elsevier Ltd [Online]. DOI: 10.1016/j.oooo.2016.08.006.

Kim, H., Park, C. M., Lee, M., Park, S. J., Song, S., Lee, J. H., Hwang, E. J. and Goo, J. M. (2016) 'Impact of Reconstruction Algorithms on CT Radiomic Features of Pulmonary Tumors : Analysis of Intra- and Inter-Reader Variability and Inter-Reconstruction Algorithm Variability', *PLoS ONE*, vol. 11, no. 10, pp. 1–11 [Online]. DOI: 10.1371/journal.pone.0164924.

Kodituwakku, S. R. (2014) 'Analysis and Comparison of Texture Features for Content Based Image Retrieval', no. March 2011.

Lalondrelle, S. and Huddart, R. A. (2012) 'Investigating the relationship between virtual cystoscopy image quality and CT slice thickness Investigating the relationship between virtual cystoscopy image quality and CT slice thickness', no. January [Online]. DOI: 10.1259/bjr/99567374.

Lambin, P., Leijenaar, R. T. H., Deist, T. M. and Peerlings, J. (2017) 'Radiomics : the bridge between medical imaging and personalized medicine', *Nature Publishing Group*, Nature Publishing Group, vol. 14, no. 12, pp. 749–762 [Online]. DOI: 10.1038/nrclinonc.2017.141.

Larue, R. T. H. ., Defraene, G., de Ruysscher, D., Lambin, P. and van Elmpt, W. (2017) 'Quantitative radiomics studies for tissue characterization: A review of technology and methodological procedures', *British Journal of Radiology*, vol. 90, no. 1070 [Online]. DOI: 10.1259/bjr.20160665.

Larue, R. T. H. ., van Timmeren, J. E., de Jong, E. E. C., Feliciani, G., Leijenaar, R. T. H., Schreurs, W. M. J., Sosef, M. N., Raat, F. H. P. J., van der Zande, F. H. ., Das, M., van Elmpt, W. and Lambin, P. (2017) 'Influence of gray level discretization on radiomic feature stability for different CT scanners , tube currents and slice thicknesses : a comprehensive phantom study', *Acta Oncologica*, Informa UK Limited, trading as Taylor & Francis Group, pp. 1544–1553 [Online]. DOI: 10.1080/0284186X.2017.1351624.

Lu, L., Ehmke, R. C., Schwartz, L. H. and Zhao, B. (2016) 'Assessing agreement between radiomic features computed for multiple CT imaging settings', *PLoS ONE*, vol. 11, no. 12, pp. 1–12 [Online]. DOI: 10.1371/journal.pone.0166550.

Mackin, D., Fave, X., Zhang, L., Fried, D., Yang, J., Taylor, B., Rodriguez-Rivera, E., Dodge, C., Jones, A. K. and Court, L. (2015) 'Measuring Computed Tomography Scanner Variability of Radiomics Features', *Investigative Radiology*, vol. 50, no. 11, pp. 757–765 [Online]. DOI: 10.1097/RLI.0000000000000180.

Mackin, D., Fave, X., Zhang, L., Yang, J., Jones, A. K., Ng, C. S. and Court, L. (2017) 'Harmonizing the pixel size in retrospective computed tomography radiomics studies', *PLoS ONE*, vol. 12, no. 9, pp. 1–17 [Online]. DOI: 10.1371/journal.pone.0178524.

Mackin, D., Ger, R., Dodge, Cristina, Fave, X., Chi, P., Yang, J., Bache, S., Dodge, Charles, Jones, A. K. and Court, L. (2018) 'Effect of tube current on computed tomography radiomic features', pp. 1–10 [Online]. DOI: 10.1038/s41598-018-20713-6.

Mahmood, U., Apte, A. P., Deasy, J. O., Schmidtlein, C. R. and Shukla-Dave, A. (2017) 'Investigating the Robustness Neighborhood Gray Tone Difference Matrix and Gray Level Co-occurrence Matrix Radiomic Features on Clinical Computed Tomography Systems Using Anthropomorphic Phantoms: Evidence From a Multivendor Study.', Journal of computer assisted tomography 41.

Manmadhachary, A., Ravi Kumar, Y. and Krishnanand, L. (2017) 'Effect of CT acquisition parameters of spiral CT on image quality and radiation dose', *Measurement*, Elsevier Ltd, vol. 103, pp. 18–26 [Online]. DOI: 10.1016/j.measurement.2017.02.020.

Mccann, C. and Alasti, H. (2004) 'Comparative evaluation of image quality from three CT simulation scanners', *Journal of Applied Clinical Medical Physics*, vol. 5, no. 4, pp. 55–70.

Molina, D., Pérez-Beteta, J., Martínez-González, A., Martino, J., Velásquez, C., Arana, E. and Pérez-García, V. M. (2016) 'Influence of gray level and space discretization on brain tumor heterogeneity measures obtained from magnetic resonance images', *Computers in Biology and Medicine*, Elsevier, vol. 78, pp. 49–57 [Online]. DOI: 10.1016/j.compbiomed.2016.09.011.

Monnin, P., Sfameni, N., Gianoli, A. and Ding, S. (2017) 'Optimal slice thickness for object detection with longitudinal partial volume effects in computed tomography', no. April 2016, pp. 251–259 [Online]. DOI: 10.1002/acm2.12005.

Murakami, Y., Kakeda, S., Kamada, K., Ohnari, N., Nishimura, J., Ogawa, M., Otsubo, K., Morishita, Y. and

Korogi, Y. (2010) 'Effect of Tube Voltage on Image Quality in 64-Section Multidetector 3D CT Angiography: Evaluation with a Vascular Phantom with Superimposed Bone Skull Structures', *AJNR AM J Neuroradiol*, vol. 31, pp. 620–625 [Online]. DOI: 10.3174/ajnr.A1871.

Nagel, H. D. (2007) 'CT Parameters that Influence the Radiation Dose. In: Tack D., Gevenois P.A. (eds) Radiation Dose from Adult and Pediatric Multidetector Computed Tomography.', *Medical Radiology (Diagnostic Imaging). Springer, Berlin, Heidelberg*, no. January 2007, pp. 51–78 [Online]. DOI: 10.1007/978-3-540-68575-3.

Nailon, W. H. (2012) 'Texture Analysis Methods for Medical Image Characterisation', *Biomedical Imaging*, pp. 75–100 [Online]. DOI: 10.5772/8912.

Padayachee, J., Alport, M. J. and Rae, W. I. D. (2006) 'Computer-Aided diagnosis in mammography: Correlation of Regions in multiple standard mammographic views of the same breats', *University of KwaZulu-Natal, School of Physics, Applied Physics Group*, pp. 1–240.

Panth, K. M., Leijenaar, R. T. H., Carvalho, S., Lieuwes, N. G., Yaromina, A., Dubois, L. and Lambin, P. (2015) 'Is there a causal relationship between genetic changes and radiomics-based image features ? An in vivo preclinical experiment with doxycycline inducible GADD34 tumor cells', *Radiotherapy and Oncology*, Elsevier Ireland Ltd, vol. 116, no. 3, pp. 462–466 [Online]. DOI: 10.1016/j.radonc.2015.06.013.

Pieper, S., Lorensen, B., Schroeder, W. and Kikinis, R. (2006) 'The NA-MIC Kit : ITK , VTK , Pipelines , Grids and 3D Slicer as An Open Platform for the Medical Image Computing Community 5) National Alliance for Medical Image Computing', *Proceedings of the IEEE Conference on Computer Vision and Pattern RecognitionIEEE*, pp. 698–701.

Reed, G. F., Lynn, F. and Meade, B. D. (2002) 'Use of coefficient of variation in assessing variability of quantitative assays', *Clinical and Diagnostic Laboratory Immunology*, vol. 9, no. 6, pp. 1235–1239 [Online]. DOI: 10.1128/CDLI.9.6.1235.

Rockwell, S., Dobrucki, I. T., Kim, E. Y., Marrison, S. T. and Vu, V. T. (2010) 'Hypoxia and radiation therapy: Past history, ongoing research, and future promise', *Current Molecular Medicine*, vol. 9, no. 4, pp. 442–458.

Salemi, F., Shokri, A., Maleki, F. H., Farhadian, M., Dashti, G., Ostovarrad, F. and Ranjzad, H. (2016) 'Effect of Field of View on Detection of Condyle Bone Defects Using Cone Beam Computed Tomography', *Journal of Craniofacial Surgery*, vol. 13, no. 4, p. 1 [Online]. DOI: 10.1097/SCS.0000000000002592.

Sanduleanu, S., Woodruff, H. C., de Jong, E. E. C., van Timmeren, J. E., Jochems, A., Dubois, L. and

Lambin, P. (2018) 'Tracking tumor biology with radiomics: A systematic review utilizing a radiomics quality score', *Radiotherapy and Oncology*, The Author(s), vol. 127, no. 3, pp. 349–360 [Online]. DOI: 10.1016/j.radonc.2018.03.033.

Schattler, H. and Ledzewicz, U. (2015) *Optimal Control for Mathematical Models of Cancer Therapies*, Greengard, S. S. A. L. and Holmes, P. (eds), Springer US.

Seibert, J. A. (2004) 'Tradeoffs between image quality and dose', vol. 34, pp. 183–195 [Online]. DOI: 10.1007/s00247-004-1268-7.

Sepp, M. and Matti, H. (2005) 'Visualizing human brain surface from T 1 -weighted MR images using texture-mapped triangle meshes', vol. 26, pp. 1–12 [Online]. DOI: 10.1016/j.neuroimage.2005.01.030.

Shafiq-ul-hassan, M., Latifi, K., Zhang, G., Ullah, G., Gillies, R. and Moros, E. (2018) 'Voxel size and gray level normalization of CT radiomic features in lung cancer', *Scientific Reports*, vol. 8, no. 10545, pp. 1–9 [Online]. DOI: 10.1038/s41598-018-28895-9.

Srinivasan, G. and Shobha, G. (2008) 'Statistical Texture Analysis', *Proceedings of world academy of* …, vol. 36, no. December, pp. 1264–1269 [Online]. Available at http://staff.fh-hagenberg.at/wbackfri/Teaching/FBA/Uebungen/UE07charRecog/StatTextAnalysisSrinivasan08.pdf.

Stefan, T. (2012) 'Texture analysis methods for the characterisation of biological and medical images', *ELBA Bioflux*, vol. 4, no. 1, pp. 8–12.

Theodoridis, S. and Koutroumbas, K. (2009) *Pattern Recognition*, [Online]. Available at http://www.malekinezhad.ir/1597492728.pdf.

van Timmeren, J. E., Leijenaar, R. T. H., van Elmpt, W., Reymen, B., Oberije, C., Monshouwer, R., Bussink, J., Brink, C., Hansen, O. and Lambin, P. (2017) 'Survival prediction of non-small cell lung cancer patients using radiomics analyses of cone-beam CT images', *Radiotherapy and Oncology*, The Authors, vol. 123, no. 3, pp. 363–369 [Online]. DOI: 10.1016/j.radonc.2017.04.016.

Tomic, N., Papaconstadopoulos, P., Aldelaijan, S., Rajala, J., Seuntjens, J. and Devic, S. (2018) 'Physica Medica Image quality for radiotherapy CT simulators with di ff erent scanner bore size', *Physica Medica*, Elsevier, vol. 45, no. July 2017, pp. 65–71 [Online]. DOI: 10.1016/j.ejmp.2017.11.017.

Tsougos, I., Vamvakas, A., Kappas, C., Fezoulidis, I. and Vassiou, K. (2018) 'Application of Radiomics and Decision Support Systems for Breast MR Differential Diagnosis', Hindawi, vol. 2018 [Online]. DOI:

10.1155/2018/7417126.

Velazquez, E. R., Parmar, C., Jermoumi, M., Mak, R. H., Baardwijk, A. Van, Fennessy, F. M., Lewis, J. H., Ruysscher, D. De, Kikinis, R., Lambin, P. and Aerts, H. J. W. L. (2013) 'Volumetric CT-based segmentation of NSCLC using 3D-Slicer', pp. 1–7 [Online]. DOI: 10.1038/srep03529.

Virendra, B., Abhinav, M., Omprakash, G., Raghuram, S., Priyusha, B., Krishnial, G. and Kanchan, S. (2015) 'The association of the uterine motion with bladder volume during radiotherapy in gynecological malignancies', *Journal of Cancer Metastasis and Treatment*, vol. 2, pp. 139–143 [Online]. DOI: 10.20517/2394-4722.2015.68.

Vuduc, R. (1997) 'Image segmentation using fractal dimension', *IIEEE Transactions on pattern analysis and machine intelligence*, vol. 17.1, no. JUNE 1997, pp. 72–77.

Withers, H. R. (1975) 'The four R's of radiotherapy', Advances in Radiation Biology.

Yan, J., Chu-shern, J. L., Loi, H. Y., Khor, L. K., Sinha, A. K., Quek, S. T., Tham, I. W. K. and Townsend, D. (2015) 'Impact of Image Reconstruction Settings on Texture Features in 18 F-FDG PET', *J Nucl Med*, vol. 56, pp. 1667–1674 [Online]. DOI: 10.2967/jnumed.115.156927.

Ye, L., Wu, X., Li, K., Bai, H., Zheng, J. and Ai, Y. (2017) 'Effects of bladder status on cervical cancer treatment with intensity-modulated radiation therapy plans', *Precision Radiation Oncology*, vol. 1, no. May, pp. 94–101 [Online]. DOI: 10.1002/pro6.25.

Yip, S. S. F., Parmar, C., Blezek, D., Estepar, R. S. J., Pieper, S., Kim, J. and Aerts, H. J. W. L. (2017) 'Application of the 3D slicer chest imaging platform segmentation algorithm for large lung nodule delineation', *PLoS ONE*, vol. 12, no. 6, pp. 1–17 [Online]. DOI: https://doi.org/10.1371/journal.pone.0178944.

Zhang, G., Sun, H., Shi, B., Jin, Z. and Xue, H. (2017) 'Quantitative CT texture analysis for evaluating histologic grade of urothelial carcinoma', *Abdominal Radiology*, Springer US, vol. 42, no. 2, pp. 561–568 [Online]. DOI: 10.1007/s00261-016-0897-2.

Zheng, Y., Solomon, J., Choudhury, K., Marin, D. and Samei, E. (2017) 'Accuracy and Variability of Texture-based Radiomics Features of Lung Lesions across CT Imaging Conditions', *Proc of SPIE Medical Imaging*, vol. 10132, pp. 1–7 [Online]. DOI: 10.1117/12.2255806.

Zukhi, J. and Yusob, D. (2017) 'Effect of slice thickness on image noise and diagnostic content of single-

source-dual energy computed tomography', *Journal of Physics: Conference Series*, pp. 1–6 [Online]. DOI: 10.1088/1742-6596/851/1/012005.

Zwanenburg, A., Leger, S., Agolli, L., Pilz, K., Troost, E. G. C., Richter, C. and Löck, S. (2019) 'Assessing robustness of radiomic features by image perturbation', *Scientific Reports*, no. June 2018, pp. 1–10 [Online]. DOI: 10.1038/s41598-018-36938-4.

APPENDICES

A. CCR phantom image sample used for manual calculations as demonstrated in Chapter 2

Table 15: 8x8 Image Intensity matrix sample from Acrylic insert centre slice

GE Machine Image acquired at 80 kV							
1127	1130	1126	1130	1134	1130	1130	1130
1121	1123	1128	1134	1132	1135	1134	1129
1133	1122	1127	1137	1128	1129	1133	1128
1131	1127	1123	1128	1128	1128	1129	1123
1124	1127	1125	1121	1127	1131	1132	1131
1131	1130	1132	1130	1128	1129	1128	1132
1129	1133	1130	1127	1132	1133	1128	1125
1124	1132	1130	1118	1126	1139	1135	1126

Table 16: 8x8 Image Intensity matrix sample from Acrylic insert centre slice

GE Machine Image acquired at 100 kV							
1138	1143	1142	1142	1145	1145	1145	1145
1141	1142	1140	1141	1143	1148	1150	1146
1142	1143	1143	1143	1147	1151	1145	1145
1142	1143	1138	1137	1144	1147	1144	1146
1143	1143	1141	1141	1142	1143	1145	1144
1147	1144	1147	1147	1142	1142	1145	1145
1146	1145	1143	1142	1142	1140	1142	1146
1142	1146	1145	1141	1148	1144	1141	1142

Table 17: 8x8 Image Intensity matrix sample from Acrylic insert centre slice

GE Machine Image acquired at 120 kV							
1148	1149	1152	1153	1151	1152	1153	1149
1146	1149	1154	1153	1151	1151	1150	1151
1151	1152	1153	1153	1156	1153	1149	1151
1152	1155	1152	1151	1155	1154	1150	1148
1151	1153	1152	1150	1151	1153	1151	1149
1147	1148	1150	1148	1150	1151	1148	1148
1139	1142	1146	1151	1153	1150	1148	1151
1148	1147	1149	1153	1154	1153	1152	1155

Table 18: 8x8 Image Intensity matrix sample from Acrylic insert centre slice

GE Machine Image acquired at 140 kV							
1155	1153	1155	1155	1157	1151	1150	1154
1155	1157	1154	1155	1155	1152	1154	1156
1157	1157	1155	1155	1157	1156	1155	1157
1160	1159	1156	1155	1157	1157	1155	1155
1158	1158	1153	1151	1154	1157	1157	1154
1153	1151	1152	1152	1154	1156	1154	1156
1155	1152	1152	1152	1155	1156	1155	1156
1155	1152	1151	1152	1156	1159	1158	1158

Table 19: 8x8 Image Intensity matrix sample from Sycamore Wood centre slice

GE Machine Image acquired at Slice Thickness 0.625 mm							
460	463	462	465	467	470	466	460
468	461	450	455	457	459	459	459
482	479	456	451	452	456	464	467
509	504	493	477	468	472	474	474
526	522	519	511	501	500	499	498
539	541	537	536	526	524	524	521
546	552	551	547	547	541	541	539
563	563	560	558	555	551	551	554

Table 20: 8x8 Image Intensity matrix sample from Sycamore Wood centre slice

GE Machine Image acquired at Slice Thickness 1.25 mm							
570	574	571	567	564	561	562	561
563	566	564	557	557	555	559	562
564	567	564	557	557	561	565	567
563	567	565	562	562	563	566	565
560	561	558	559	559	558	562	558
566	561	556	557	560	560	557	550
566	560	555	556	559	562	559	553
562	558	556	559	563	559	559	560

Table 21: 8x8 Image Intensity matrix sample from Sycamore Wood centre slice

GE Machine Image acquired at Slice Thickness 2.5 mm							
567	565	567	565	563	562	558	558
566	569	569	565	561	562	559	561
563	569	568	566	562	562	561	564
561	563	564	566	564	561	559	559
559	560	561	563	563	561	558	555
560	561	562	560	561	561	558	557
565	564	562	561	562	561	559	561
566	563	559	559	561	562	563	562

Table 22: 8x8 Image Intensity matrix sample from Sycamore Wood centre slice

GE Machine Image acquired at Slice Thickness 3.75 mm							
567	566	563	562	561	560	558	555
570	567	566	567	567	563	561	560
567	565	565	567	566	564	562	560
563	560	566	568	563	561	560	557
562	561	565	567	565	563	560	558
566	566	566	565	565	564	563	562
568	567	566	562	562	565	564	562
567	565	564	563	562	564	565	562

Table 23: 8x8 Image Intensity matrix sample from Sycamore Wood centre slice

GE Machine Image acquired at Slice Thickness 5 mm							
562	565	566	564	562	562	562	560
564	565	567	565	566	566	565	563
568	566	566	567	567	567	566	564
567	566	566	567	567	567	566	564
565	566	567	568	567	566	566	564
563	564	566	565	566	564	563	563
560	563	565	564	564	560	561	562
559	563	562	562	561	559	559	561

B. Sample graphs of Tumour Sensitivity to radiotherapy treatment

Fig 43 to Fig 48 below shows the patient tumour response to radiotherapy fractionated treatment. The graphs are plotted using the average of the tumour feature values and the normalised to the bladder features of the specific patient. The y-axis of the graphs as labelled represents the tumour feature values of a specific patient (e.g. patient A or patient B etc.) and the x-axis represents the day the radiotherapy treatment fraction was delivered.

The plotted feature values show an oscillating response to the treatment fractions. The sinusoidal response of a tumour to treatment shows unequal peaks at different treatment fraction points. This means these features exhibits a personalised tumour sensitive to radiation treatment

There exist tumours that response to radiotherapy treatments in the same manner whilst other tumour's response is unrelated to other tumours. Fig 44, Fig 46, Fig 47 and Fig 48 shows that tumours B, D, E and F followed similar response to radiotherapy treatment. The values of the plots point on point do not have exact feature values for each treatment fraction sampled but they followed the same trend from one fraction point to the other. Fig 49 and Fig 50 shows Toshiba Aquillion tube current variation heat maps.

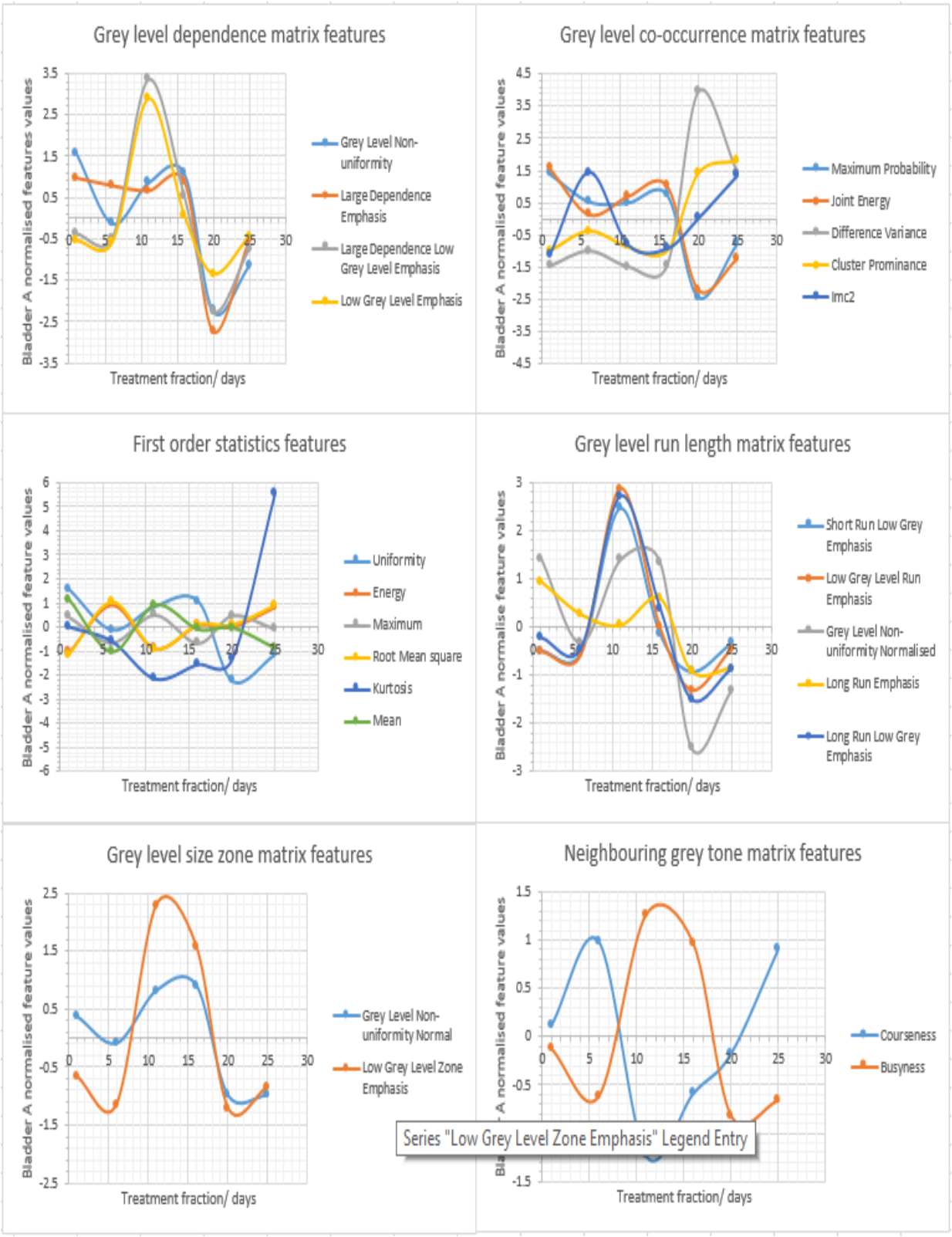

Fig 43. Graphical representation of tumour A sensitivity to the radiotherapy fractionated treatment employing the identified robust texture features.

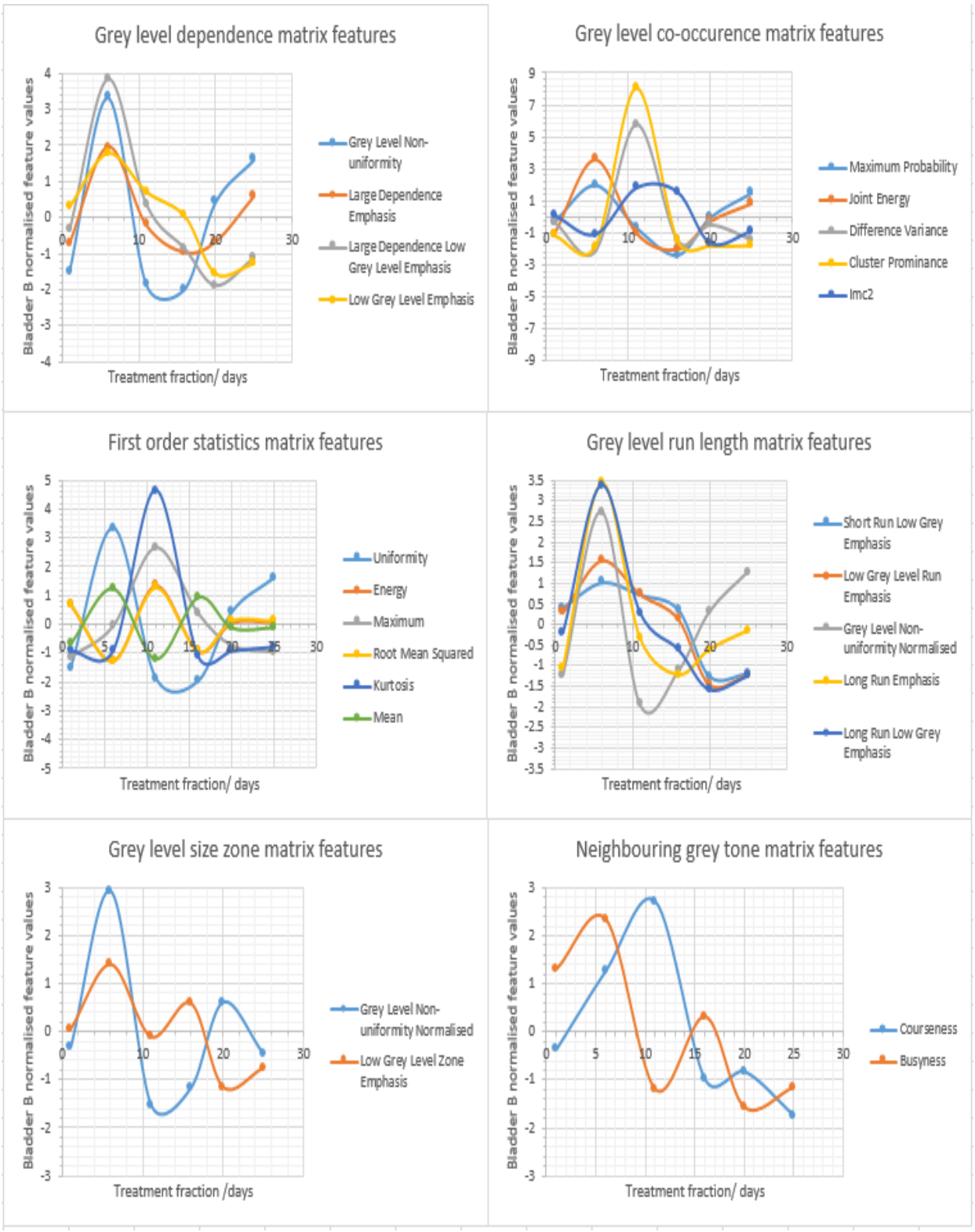

Fig 44. Graphical representation of tumour B sensitivity to the radiotherapy fractionated treatment employing the identified robust texture features.

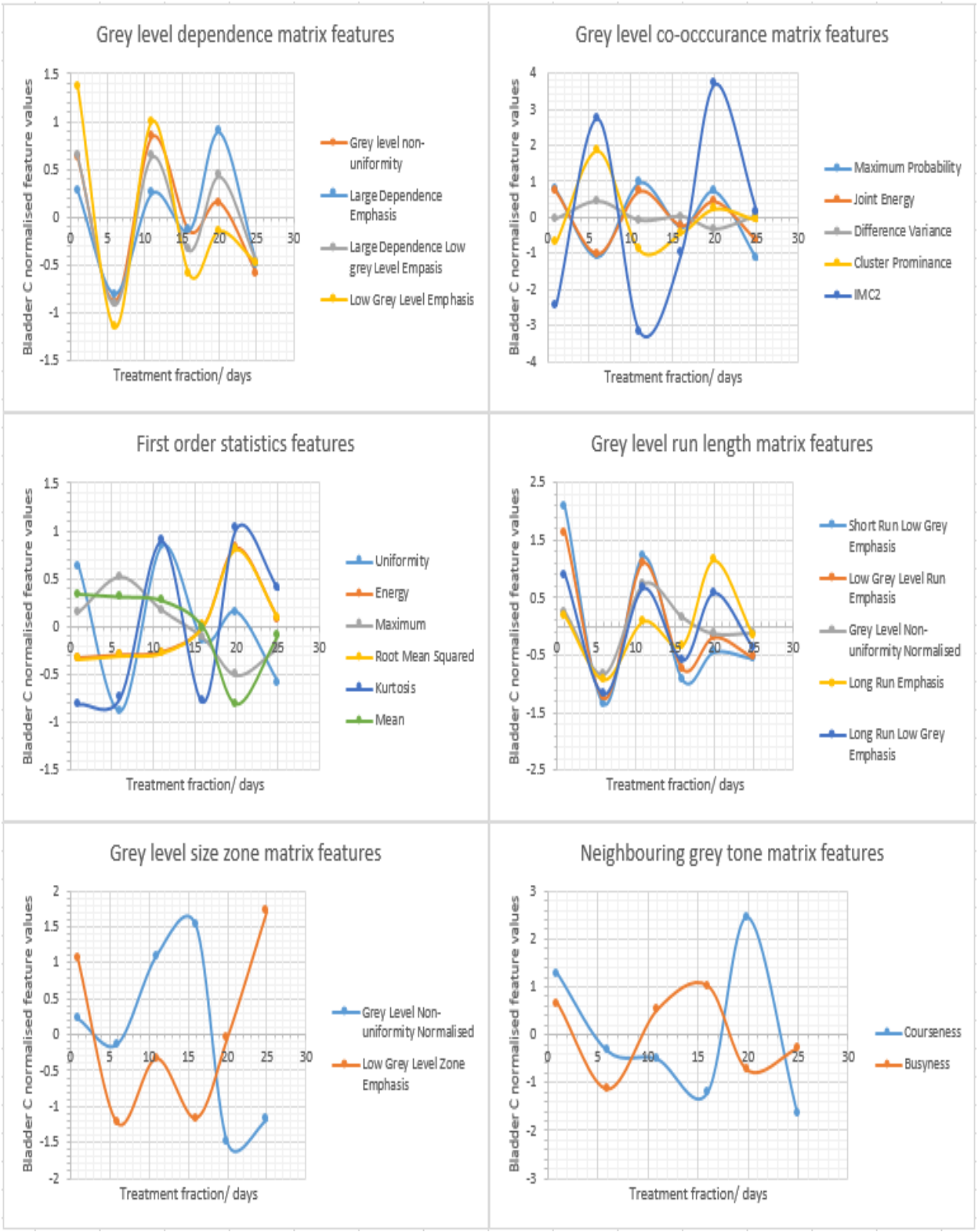

Fig 45. Graphical representation of tumour C sensitivity to the radiotherapy fractionated treatment employing the identified robust texture features.

Fig 46. Graphical representation of tumour D sensitivity to the radiotherapy fractionated treatment employing the identified robust texture features.

Fig 47. Graphical representation of tumour E sensitivity to the radiotherapy fractionated treatment employing the identified robust texture features.

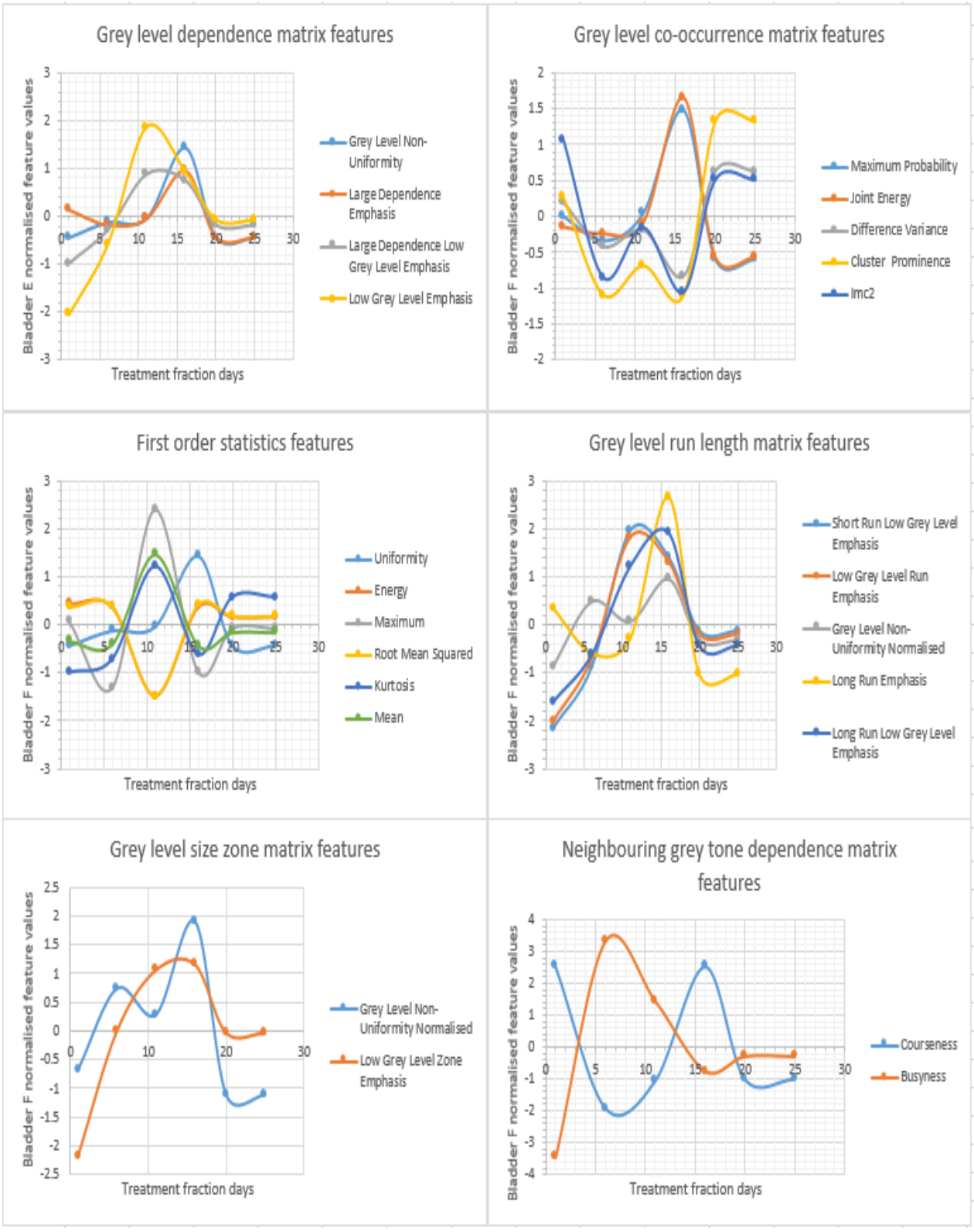

Fig 48. Graphical representation of tumour F sensitivity to the radiotherapy fractionated treatment employing the identified robust texture features.

C. Toshiba Aquillion Large bore CT unit tube current heat maps sample

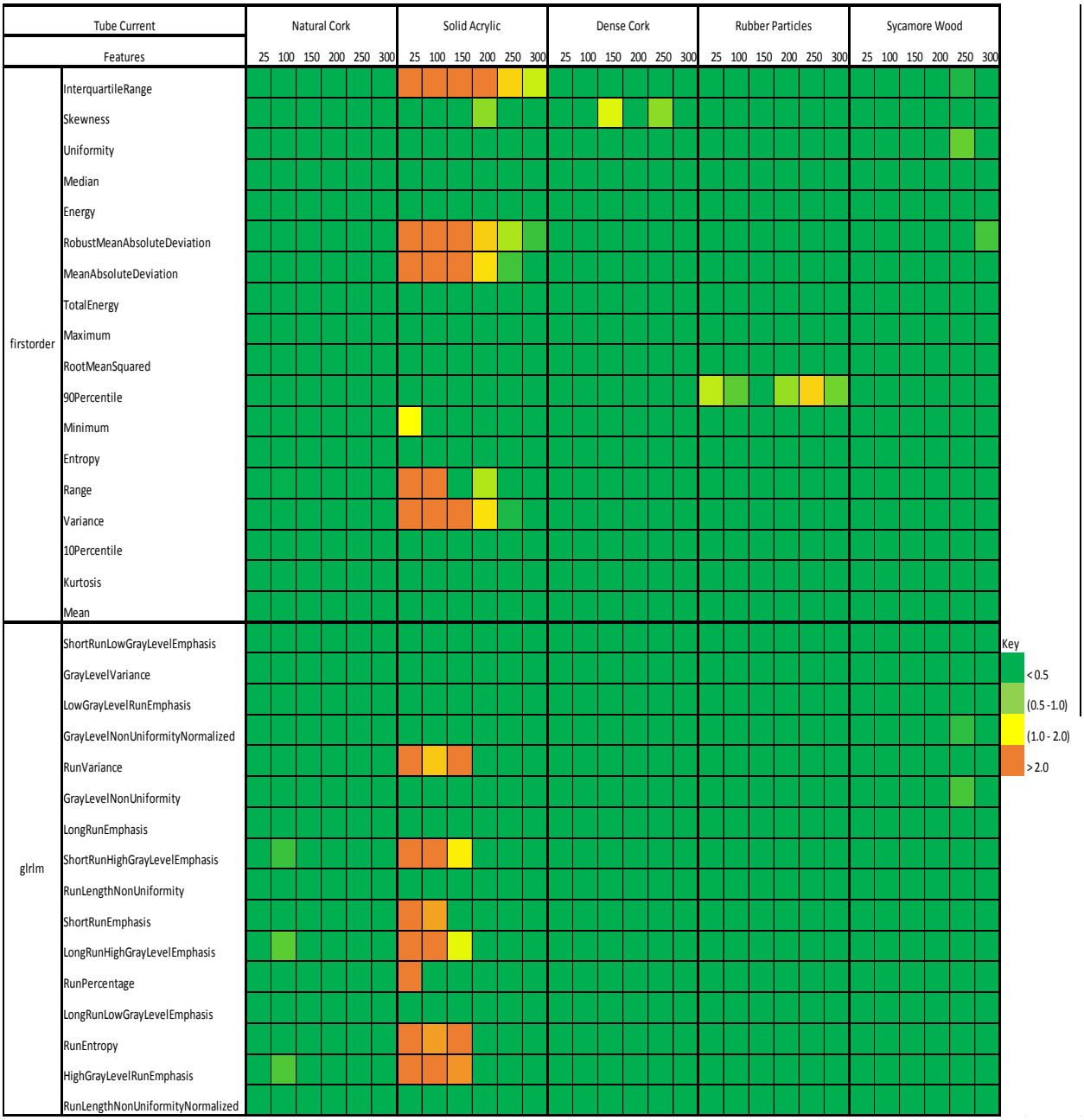

Fig 49. Tube current heat maps that represent the patient normalised first order statistics and GLRLM feature values of 5 cartridges that make up the CCR phantom, and the images used were acquired using a Toshiba Aquillion CT machine.

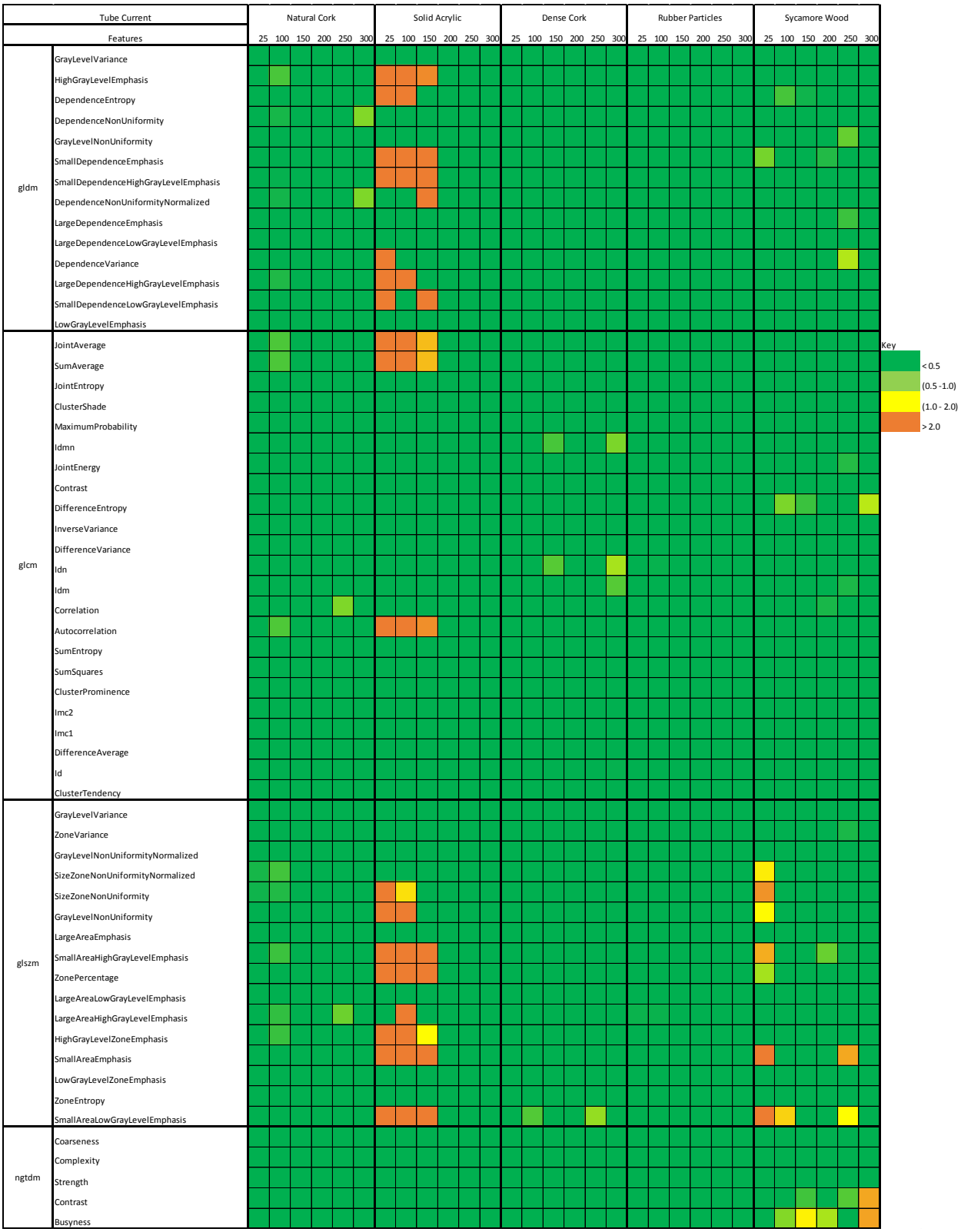

Fig 50. Tube current heat maps that represent the patient normalised GLDM, GLCM, GLSZM and NGTM feature values of 5 cartridges that make up the CCR phantom, and the images used were acquired using a Toshiba Aquillion CT machine.

D. Evaluation committee approval

UNIVERSITY OF THE FREE STATE
UNIVERSITEIT VAN DIE VRYSTAAT
YUNIVESITHI YA FREISTATA

UFS·UV
HEALTH SCIENCES
GESONDHEIDSWETENSKAPPE

NB: IT IS IMPORTANT TO INFORM THE STUDENT ABOUT POSTGRADUATE BURSARIES – ADVERTISED IN JANUARY OF EACH YEAR

SECTION B **MUST BE COMPLETED BY THE CHAIR OF THE EVALUATION COMMITTEE**

Initials and surname (student): Frank Makosa

Student number: 2014024554

Chair of the Evaluation Committee: N Mofolo

Members of the Evaluation Committee:	Present	Absent
Prof N Mofolo	✓	
Prof W Rae	✓	
Dr K van der Walt	✓	
Dr J van Staden	✓	
Ms D (FHJ) O'Reilly	✓	
Prof G Joubert		✓

Date of meeting: 12 December 2017

Proposed title: Computed tomography radiomics texture features dependence on upon imaging parameters

Title has been language edited by: Supervisor: Ms S.N.N. Acho

(Mark with an X)

Ethical aspects have been addressed:	Yes X	No
Facilities available:	Yes	No
Funds available:	Yes	No
Time schedule acceptable:	Yes	No
The study is recommended:	Yes	No

Remarks: Title was amended and objectives aligned in accordance to the title.

Prof. N. Mofolo
Head: School of Clinical Medicine
2018 -01- 19
Faculty of Health Sciences
University of the Free State

Prof. N. Mofolo
Head: School of Clinical
2018 -01-
Faculty of Health
University of the

E. Ethics Clearance

UNIVERSITY OF THE FREE STATE
UNIVERSITEIT VAN DIE VRYSTAAT
YUNIVESITHI YA FREISTATA

UFS·UV
HEALTH SCIENCES
GESONDHEIDSWETENSKAPPE

Health Sciences Research Ethics Committee

03-Jul-2018

Dear **Mr Frank Makosa**

Ethics Clearance: **Computed tomography radiomics texture features dependence on imaging parameters**
Principal Investigator: **Mr Frank Makosa**
Department: **Medical Physics (Bloemfontein Campus)**
APPLICATION APPROVED

Please ensure that you read the whole document

With reference to your application for ethical clearance with the Faculty of Health Sciences, I am pleased to inform you on behalf of the Health Sciences Research Ethics Committee that you have been granted ethical clearance for your project.

Your ethical clearance number, to be used in all correspondence is:**UFS-HSD2018/0130/3107**

The ethical clearance number is valid for research conducted for one year from issuance. Should you require more time to complete this research, please apply for an extension.

We request that any changes that may take place during the course of your research project be submitted to the HSREC for approval to ensure we are kept up to date with your progress and any ethical implications that may arise. This includes any serious adverse events and/or termination of the study.

A progress report should be submitted within one year of approval, and annually for long term studies. A final report should be submitted at the completion of the study.

The HSREC functions in compliance with, but not limited to, the following documents and guidelines: The SA National Health Act. No. 61 of 2003; Ethics in Health Research: Principles, Structures and Processes (2015); SA GCP(2006); Declaration of Helsinki; The Belmont Report; The US Office of Human Research Protections 45 CFR 461 (for non-exempt research with human participants conducted or supported by the US Department of Health and Human Services- (HHS), 21 CFR 50, 21 CFR 56; CIOMS; ICH-GCP-E6 Sections 1-4; The International Conference on Harmonization and Technical Requirements for Registration of Pharmaceuticals for Human Use (ICH Tripartite), Guidelines of the SA Medicines Control Council as well as Laws and Regulations with regard to the Control of Medicines, Constitution of the HSREC of the Faculty of Health Sciences.

For any questions or concerns, please feel free to contact HSREC Administration: 051-4017794/5 or email EthicsFHS@ufs.ac.za.

Thank you for submitting this proposal for ethical clearance and we wish you every success with your research.

Yours Sincerely

Dr. SM Le Grange
Chair : Health Sciences Research Ethics Committee

Health Sciences Research Ethics Committee
Office of the Dean: Health Sciences
T: +27 (0)51 401 7795/7794 | E: ethicsfhs@ufs.ac.za
IRB 00006240; REC 230408-011; IORG0005187; FWA00012784
Block D, Dean's Division, Room D104 | P.O. Box/Posbus 339 (Internal Post Box G40) | Bloemfontein 9300 | South Africa
www.ufs.ac.za